The Dissertation Committee for Arun Manickam
certifies that this is the approved version of the following dissertation:

Integrated Impedance Spectroscopy Biosensors

Committee:

Arjang Hassibi, Supervisor

Dean P. Neikirk

David Z. Pan

T.R. Viswanathan

Sam Kavusi

Integrated Impedance Spectroscopy Biosensors

by

Arun Manickam, B.E., M.S.E.

DISSERTATION

Presented to the Faculty of the Graduate School of

The University of Texas at Austin

in Partial Fulfillment

of the Requirements

for the Degree of

DOCTOR OF PHILOSOPHY

THE UNIVERSITY OF TEXAS AT AUSTIN

May 2012

Dedicated to my parents,

Dr. S. Manickam and Dr. P. S. Maheswari

Acknowledgments

First and foremost, I would like to express my gratitude to my advisor, Prof. Arjang Hassibi. I am really impressed by his broad vision and his constant pursuit for excellence, which served as the primary motivation for my Ph.D. His excellent mentorship, which helped me overcome technical as well as non-technical challenges, had enabled me to remain on track and obtain my Ph.D. degree, which is my biggest achievement so far.

I would like to thank my committee members Dr. Sam Kavusi, Prof. Dean Neikirk, Prof. T. R. Viswanathan and Prof. David. Z. Pan for serving on my dissertation committee and providing invaluable comments and feedback. I would like to thank Dr. Sam Kavusi for mentoring me at Bosch Research, where I was able to obtain a valuable insight into the world of biosensing. I would like to thank Dr. Christopher Andrew Johnson for helping me with the biochemical experiments and providing me with valuable advice.

I would like to thank Dr. Eric Soenen at TSMC for providing us with access to tapeouts, which enabled me to build chips and permitted me to complete my Ph.D. project.

I would like to thank Prof. T. R. Viswanathan and Dr. Lakshmi Viswanathan for providing me with valuable guidance. I would like to thank Mark McDermott and Murali Jegannathan for assisting me with the develop-

ment of digital IC cores. I would like to thank Aaron Chevalier, Dr. Bingling Li, and Prof. Andrew Ellington, for providing me assistance in developing the protocols for biochemical tests and for performing those tests, which was an essential part of my Ph.D.

I would like to thank Ritu Raj Singh for all our valuable discussions and for working with me on joint projects, which were of great interest to our group. I would like to thank my other group members, Sahar Ayazian, and Shreepriya Das for all their valuable comments and technical discussions.

I would like to thank my undergraduate adviser, Prof. P. V. Ramakrishna, for motivating me to pursue a career in research.

I am dedicating my thesis to my parents, Dr. S. Manickam and Dr. P. S. Maheswari, whose continued support enabled me to reach where I am today.

Throughout my stay at UT, I was fortunate to make good friends, Karthik Ganesan, Pradeep Ananth Govind, Lince Merin, Aditi Saha, Chinmayi Krishnappa, Jasveen Kaur, Ashish Khandelwal, Atif Malayalam Mohammed and Pavithra Raman. I will always cherish the lovely memories of the good times I had with them, during my five years of stay at Austin. Thank you all for the wonderful time I had.

Integrated Impedance Spectroscopy Biosensors

Arun Manickam, Ph.D.
The University of Texas at Austin, 2012

Supervisor: Arjang Hassibi

Affinity-based biosensors, or in short biosensors, are extremely powerful and versatile analytical tools which are used for the detection of a wide variety of bio-molecules. In recent times, there has been a need for developing low-cost and portable affinity-based biosensor platforms. Such systems need to have a high density of detection sites (i.e biosensing elements) in order to simultaneously detect multiple analytes in a single sample. This has led to the creation of integrated biosensors, which make use of integrated circuits (ICs) for bio-molecular detection. In such systems, it has been demonstrated that by taking advantage of the capabilities of semiconductor and very large scale integrated (VLSI) circuit fabrication processes, it is possible to build compact miniaturized biosensors, which can be used in wide variety of applications such as in molecular diagnostics and for environmental monitoring.

Among the various detection modalities for biosensors, Electrochemical Impedance Spectroscopy (EIS) permits real-time detection and has label-free

detection capabilities. EIS is fully electronic in nature. Hence, it can be implemented using standard IC technologies. The versatility and ease of integration of EIS makes it a promising candidate for developing integrated biosensor platforms.

In this thesis, we first examine the underlying principles of EIS method of biosensing. By analyzing an immunosensor assay as an example, we show that EIS based biosensing is a highly sensitive detection method, which can be used for the detection of a wide variety of analytes. Since EIS relies on small impedance changes in order to perform detection, it requires highly accurate models for the electrode-electrolyte systems. Hence, we also introduce a compact modeling technique for the distributed electrode-electrolyte systems with non-uniform electric fields, which is capable of modelling noise and other non-idealities in EIS.

In the second part of this thesis, we describe the design and implementation of an integrated EIS biosensor array, built using a standard complementary metal-oxide-semiconductor (CMOS) process. The chip is capable of measuring admittance values as small as $10^{-8}\Omega^{-1}$ and has a wide dynamic range (90dB) over a wide range of frequencies (10Hz-50MHz). We also report the results obtained from the DNA and protein detection experiments performed using this chip.

Table of Contents

List of Tables

List of Figures

Chapter 1

Motivation and Outline

1.1 Motivation

A significant part of research in life sciences is geared towards the development of analytical platforms that serve as tools for detecting biomolecules such as DNA, proteins, toxins, and even micro-organisms. The term biosensor particularly applies to systems which are used to detect the presence or estimate the concentration of biological analytes (molecules of interest, that are to be analyzed) in a sample. Biosensors are used in a wide variety of application areas such as in molecular diagnostics, cancer research, food processing, and environmental monitoring. The recent demand to build cost-effective compact biosensor platforms which, at the same time, are capable of detecting multiple analytes in parallel has introduced in new design challenges for both the biological and the engineering aspects of biosensor design. Such platforms will be used in future point-of-care (PoC) high-performance molecular detectors and other such point-of-use (PoU) applications.

Among the various techniques for biomolecular detection, affinity-based sensing is the most popular. Affinity-based biosensors make use of biomolecular recognition elements (also known as the molecular probes) which can

uniquely bind to the analyte ([1],[2]). These sensors take advantage of the specificity of biomolecular interactions such as in DNA-DNA hybridization and antigen-antibody interactions.

A wide variety of detection methods are used to convert the physiochemical interactions between the probe and the analyte into measurable signals in optical, electrical or magnetic domains [1]. Most of these methods require the use of labels which are additional molecular structures added as tags in order to detect the analyte with high sensitivity and specificity. Optical methods, which make use of florescent labels, are very common today. However optical methods require expensive and complex instrumentation such as laser light sources, filters and CCD cameras, which are difficult to miniaturize. Recently, electrochemical methods are also becoming increasing popular due to ease of miniaturization.

The push towards miniaturization and cost-effectiveness has resulted in the use of integrated circuits (ICs) for biosensing. This has led to the development of integrated biosensors, in which the biomolecular assay, including the probe and the analyte, and the detection circuitry are all incorporated onto the same platform. Since ICs are manufactured using robust VLSI fabrication methods, integrated biosensors have excellent manufacturability and yield. Large scale production of these ICs can greatly facilitate cost reduction. Also, it is possible to build massively parallel arrays on smaller areas, making it possible to build high density arrays. Several integrated biosensors have been demonstrated [3], which make use of various detection methods such as

florescence, electrochemical and magnetic bead based detection.

In this thesis, we will focus on using electrochemical impedance spectroscopy (EIS) for biomolecular detection. EIS is a powerful method which could be used for the detection of a wide variety of biomolecules. EIS also allows label-free and real-time detection, which can be used to study of kinetics of molecular interactions in their natural form. Furthermore, EIS-based sensors can be readily built using standard complementary metal-oxide-semiconductor (CMOS) processes. In this thesis, we will examine various considerations in EIS based sensing and provide an example immunosensor assay. Subsequently, we will discuss in detail the design, implementation and testing of an integrated EIS biosensor which was fabricated using a standard CMOS process.

1.2 Outline

Chapter 2 explains the basic concepts involved in affinity-based biosensing. It discusses the various steps involved, explains the different detection methods, and finally defines important terms such as specificity, sensitivity, labeling and real-time detection.

Chapter 3 introduces EIS based sensing, explains in detail the equivalent circuit model of the electrode-electrolyte structure, which is critical for the understanding of EIS systems and analyzing the measurement. Next, we discuss the principle of detection and explain the various considerations such as the choice of the electrode surface and the surface linkage options. Next, we describe an example immunosensor system, providing the detailed protocol

and a detailed discussion of the experimental results obtained.

Chapter 4 provides a general model to accurately describe the observed admittance and noise power spectral density (PSD) of distributed electrode-electrolyte systems, which are important in EIS. The described methodology is based on initially modelling the lumped solid-solution interface and the distributed bulk solution independently, and subsequently merging them together using circuit theory techniques.

Chapter 5 explains in detail the design, the implementation and measurement results obtained of a fully integrated CMOS EIS biosensor chip. The chip has 100 on-chip gold electrodes, and has a very wide detection dynamic range (90dB) over a broad range of frequencies (1kHz-50MHz). Next, we will describe the design and the implementation of a sigma-delta analog-to-digital converter (ADC), which has been specifically tailored towards our EIS sensor application.

Chapter 6 provide a summary of this thesis and discusses the future work.

Chapter 2

Affinity-Based Biosensor Basics

The design of an integrated biosensor is a multidisciplinary problem, which requires deep understanding of topics in the fields of biology, chemistry and electrical engineering. The key objective of this chapter is to provide an introduction to the important concepts in biosensing and to introduce the reader to some of the different detection methodologies used in biosensing.

2.1 Chapter Overview

Affinity-based biosensing (or in short version, biosensing) is a fundamental method to estimate the concentration of an analyte (molecule of interest which is being analyzed) in an aqueous sample ([1],[2],[4]). They make use of biological recognition elements (also known as probes) such as DNA and proteins, which can selectively bind to the analyte. In the section 2.2, the basic steps in affinity-based biosensing are discussed. Typically, the probes are immobilized onto a solid surface and the analytes bind to the probes, forming probe-analyte complexes at the surface. Using different detection methods, the concentration of the captured molecules is measured and subsequently used to estimate the original analyte concentration in the sample. Among the various

metrics used to compare different biosensors, specificity and sensitivity are the most important. Sensitivity refers to the lowest detectable analyte concentration, whereas specificity gives a measure of the ability of the system to detect the analyte in the presence of other interfering molecules. Both these parameters are closely related to the kinetics of the probe-analyte interactions, which are explained in the section 2.3. Then, we shift the focus to different detection methods (i.e, transduction mechanisms) in the following section, which convert the bio-chemical "signals" into measurable quantities such as photon flux, voltage, current or impedance.

Among the various metrics used to compare the different detection methods, the requirement for labels and the ability to perform real-time detection are important. Labels are additional reagents we add to the biosensing system, which have differentiating bio-physical properties that aid or enhance in the transduction process. A discussion about the merits and demerits of using labels is provided in the section 2.4.1. Real-time detection enables us to study the kinetics of the probe-analyte interactions. How real-time detection helps in obtaining a better estimate of analyte concentration is explained in the section 2.4.2. Finally, some of the popularly used detection methods are introduced in the section 2.4.3, along with a table comparing them in the view of the key metrics such as requirement of labels, ability to perform real-time detection and ease of integration of the instrumentation with standard IC technologies.

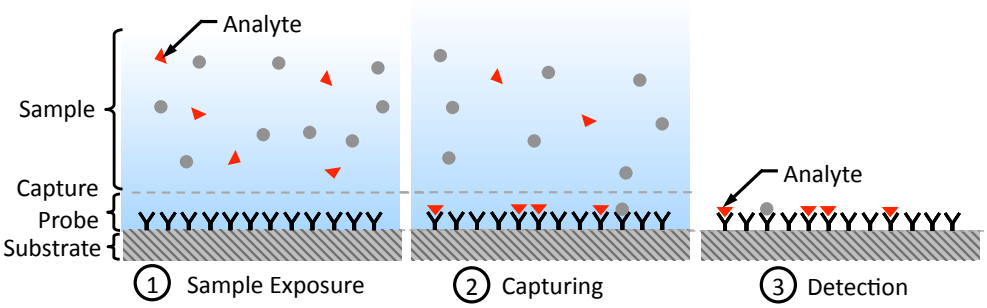

Figure 2.1: Steps in affinity-based biosensing.

2.2 Steps in Affinity-Based Biosensing

In biology, there are certain molecular pairs, which form a bond when they are in close proximity to each other. Binding reduces the overall energy, making it thermodynamically more favourable for the molecules to form a complex, rather than to remain as individual molecules. These molecular pairs, which are capable of binding together to form a complex, are said to have affinity for each other. Affinity-based biosensors make use of these molecular pairs, to perform biomolecular sensing ([1],[2]).

In figure 2.1, we show the steps involved in an affinity-based biosensing scheme [4]. Key to this scheme is the use of probes, which have a strong chemical affinity towards the analyte. The probe molecules are immobilized on a solid surface. The surface is then exposed to a sample containing the analytes. The analytes diffuse through the solution. The analytes, which reach the surface, bind to the probes during the capture phase. Finally, the concentration of probe-analyte complexes is measured using a detection method. These detection methods perform the transduction of the signal from the physiochemical

domain to a different domain (eg. optical or electrochemical), enabling detection. The measured signal is then used to arrive at an estimate of the original number of analyte molecules present in the sample.

Typically, by removing the sample solution, the binding or the capturing process is stopped and the dried solid surface, with the probe-analyte complexes immobilized on them, is used for detection. Such a method is called *end-point detection* method. Some detection methods enable measuring the concentration of the probe-analyte complexes during the capturing phase itself. Such methods are said to permit *real-time* detection.

2.3 Specificity and Sensitivity

Let us first examine a simple probe-analyte system ([2],[5]) governed by the equation 2.1.

$$P + A \underset{k_2}{\overset{k_1}{\rightleftharpoons}} PA \tag{2.1}$$

where P denotes the probe molecule, A denotes the analyte molecule, PA is the probe-analyte complex. In equation 2.1, k_1 is the association rate constant, and k_2 is the dissociation rate constant, which determine the kinetics of the reaction. These two parameters also specify the percentage of the total analyte molecules which form the probe-analyte complex under equilibrium conditions. It is important to keep in mind that the estimate of the initial concentration of A ($[A_0]$) is done solely using the measured value of the concentration of PA.

The rate equation for a simple probe-analyte system is given by

$$\frac{d[P]}{dt} = \frac{d[A]}{dt} = -\frac{d[AP]}{dt} = k_1[A][P] - k_2[PA] \tag{2.2}$$

The equilibrium condition is attained when the concentrations $[P]$, $[A]$ and $[AP]$ no longer change with time. This happens when $\frac{d[AP]}{dt} = 0$. Using the condition $k_1[A][P] - k_2[PA] = 0$, it is possible to estimate the equilibrium concentrations. Since the equilibrium value of $[AP]$ is a function of the ratio $\frac{k_2}{k_1}$, this ratio is important in determining the equilibrium concentration of probe-analyte pair $[AP]$. This ratio is called the equilibrium dissociation constant [6] and is given by the equation

$$K_d = \frac{k_2}{k_1} = \frac{[PA]}{[A][P]} \tag{2.3}$$

where the concentrations are in the equilibrium condition.

The equilibrium dissociation constant K_d is a good measure of affinity for a probe-analyte pair. It determines the fraction of the total analyte concentration, which binds to the probes to form the probe-analyte complex. Figure 2.2 shows the total fraction of the analyte molecules, which bind to the probes, under equillibrium conditions, as a function of the dissociation constant K_d. The initial probe concentration $[P]$ is taken to be equal to the initial analyte concentration $[A_0]$. As evident from the figure, the ratio $\frac{[PA]}{[A_{initial}]}$ drops for larger values of K_d, which indicates lesser affinity between A and P.

In all biosensor systems, there are two important considerations: sensitivity and specificity. *Sensitivity* refers to lowest detectable analyte concentration. Sensitivity depends on the probe concentration, the equilibrium

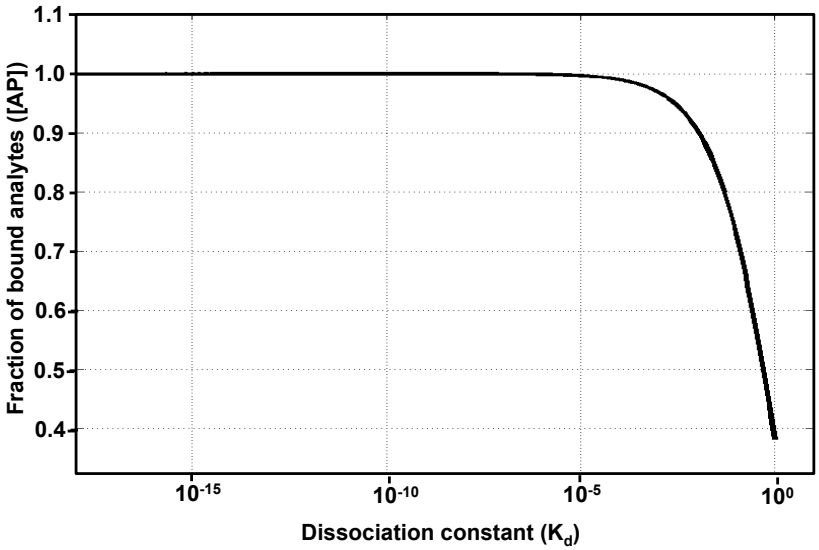

Figure 2.2: Affinity plot: fraction of bound analytes as a function of the dissociation constant.

dissociation constant K_d and the detection limit of detection modality being used. A good analogue for sensitivity, in the case of a communication system, is the electrical sensitivity, which is set by the noise floor of the receiver [4].

Specificity, on the other hand, refers to the detection of the analyte of interest in the presence of other molecules, which can potentially bind to the probe. Such molecules, generally referred to as interferers, compete with the analytes by forming molecular complexes with the probes ([2],[7]). The concentration of interferers can be much larger than the analyte itself. For example, a freshly obtained blood sample contains a large number of interfering proteins and other biological entities, which can non-specifically bind to the probe. Specificity is mainly determined by the uniqueness of the probe−analyte binding, which is determined by the equilibrium dissociation constant K_d. A good

analogue for specificity is the signal to interference ratio specification of a communication system, which determines how robust the system functions in the presence of interferers.

In order to better understand specificity, let us take an example system in which we have an interferer molecule I in addition to the probe and analyte molecules P and A. The equations governing the system are

$$P + A \underset{k_2}{\overset{k_1}{\rightleftharpoons}} AP \tag{2.4}$$

and

$$P + I \underset{k_4}{\overset{k_3}{\rightleftharpoons}} PI \tag{2.5}$$

The equilibrium dissociation constant for the reaction 2.5 is given by

$$K_{dI} = \frac{k_4}{k_3} = \frac{[PI]}{[I][P]} \tag{2.6}$$

Figure 2.3 shows the plot of $\frac{[PI]}{[PA]}$ as a function of ratio of the dissociation constants $\frac{K_{dI}}{K_d}$. The graph is plotted under different initial conditions where the initial concentration of interferer $[I_0]$ is equal to, 10, 100, and 1000 times larger than the initial analyte concentration $[A_0]$. The initial probe concentration is assumed to the initial analyte concentration, presenting a scenario where the analyte and the interferer compete with each other to form complexes with the probe. As can be seen, for equal initial concentrations, $\frac{[PI]}{[PA]}$ tends to be close to 1 if the dissociation constants are equal. But for the extreme case where the ratio is 1000, one requires K_d of probe-analyte pair to be at least three orders of

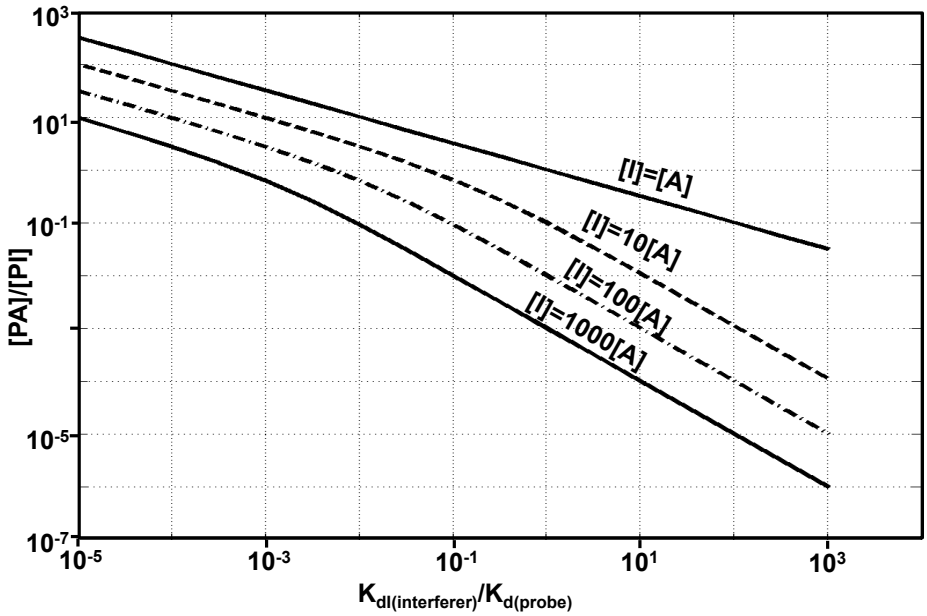

Figure 2.3: Specificity plot: $\frac{[PI]}{[PA]}$ vs. $\frac{K_{dI}}{K_d}$.

magnitude larger than K_{dI} for achieving $\frac{[PI]}{[PA]}$ of 1. This is the typically the case in many biosensor systems, where the interfering molecules could be in much higher concentration when compared to the analyte. This can greatly impact our ability to accurately estimate the original concentration $[A_0]$, since only $[AP]$ can be measured and is used to estimate $[A_0]$. This mandates K_d to be at least 4-5 orders of magnitude higher than K_{dI} of the interfering molecules, to achieve reasonable specificity.

2.4 Detection

As stated earlier, the detection step in an affinity-based biosensing system provides a quantitative way of measuring $[AP]$ at equilibrium, from which

the initial analyte concentration can be estimated. The detection step is a critical step, in which the signal is converted from the "molecular domain" to a measurable signal such as an optical or electrical signal. There are a wide variety of detection methods used for this. Before comparing different detection methods, it is beneficial to examine whether the method requires the use of reporter molecules (i.e, labels) or not and whether it permits real-time detection or not.

The subsequent sub-sections explain in detail the merits and demerits of using labels and having a real-time detection system. The most popular methods are the optical and the electrochemical methods. Different optical methods such as fluorescence and bioluminescence and electrochemical methods like amperometry, potentiometry and electrochemical impedance spectroscopy are discussed.

2.4.1 Label vs. Label-free Detection

In most biosensors, molecular labels are attached to the analytes of interest as shown in figure 2.4. These labels exhibit unique properties such as fluorescence (such as Cy-3, Cy-5, and FAM molecules) [8], chemi-luminescence (enzymes such as HRP, and luciferase) [9] or enhanced electrochemical activity (redox markers such as ferrocene, and $Fe(CN)_6$) [10]. These unique properties are extrinsic to the target molecules and samples used and hence the use of labels can greatly enhance detection sensitivity. One popular example is the DNA arrays [11], which uses fluorescent labels for detection.

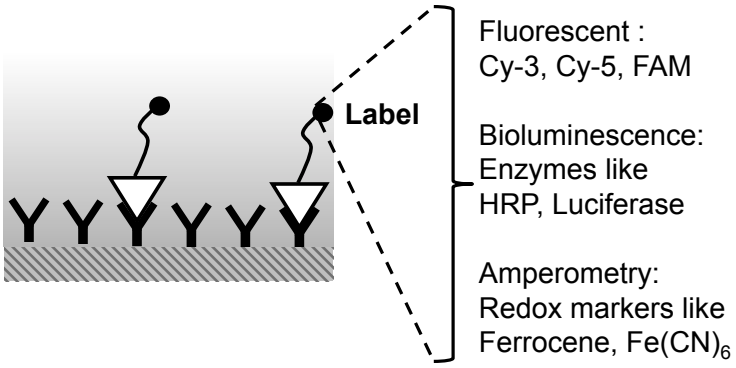

Figure 2.4: Different types of labels used in affinity-based biosensing.

In spite of these advantages, lot of work has been done in the recent years to develop label-free detection methods ([7],[10],[12],[13]). While it is relatively easy to label DNA molecules [11], it is difficult to label irregular and smaller molecules. In such cases, labeling can affect its binding properties and hence, the affinity. Labeling adds to the overall cost and in most cases, makes real-time detection difficult. Furthermore, labeling adds more steps, increasing the overall uncertainty, thereby making the system less repeatable ([7],[12]).

2.4.2 End-point vs. Real-time Detection

Let us consider the simple probe-analyte system governed by the equation 2.1. The concentration of the probe-analyte complex x=$[AP]$ as a function of time is shown in figure 2.5 [5]. In a real-world experiment, there is some amount of uncertainty associated with the measurement of $[AP]$. This uncertainty can arise from various sources such as labeling uncertainty, sam-

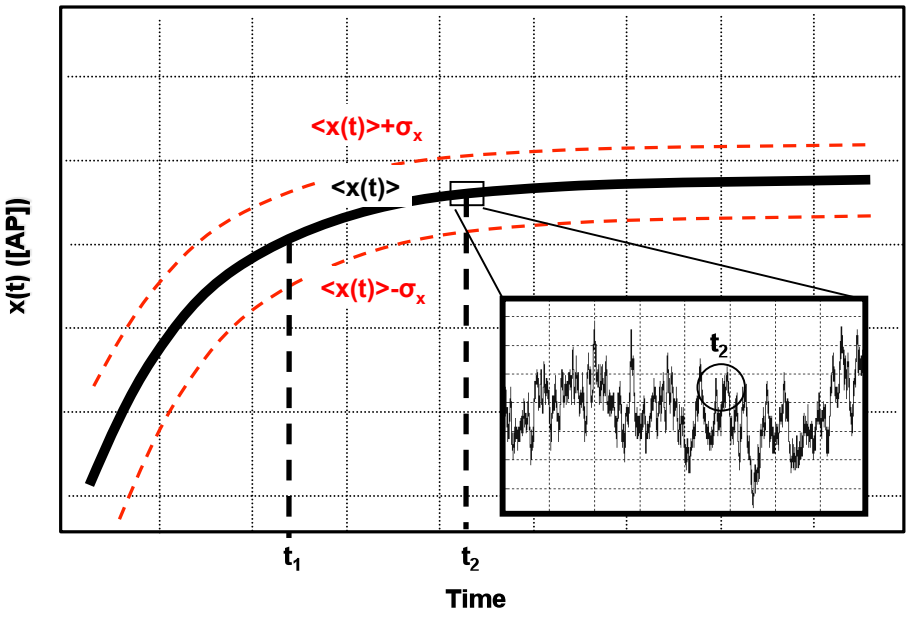

Figure 2.5: Real-time detection.

ple purification, noise of the detection system, fluctuations in environmental conditions, and thermal noise of the electrolyte [5]. Figure 2.5 shows three lines, the average and the two extreme values of the $[AP]$ over different trials, assuming that the standard deviation of the uncertainty in $[AP]$ is σ_x.

In the end-point detection method, the reaction is stopped, the solution is removed and a single point measurement of $[AP]$ is made. This can lead to significant errors. Firstly, if the reaction is stopped at t_1, the system has not settled yet and this leads to an underestimate of $[AP]$, and thereby of the analyte concentration. Secondly, even if one considers measuring at t_2, the random uncertainty in the measured value can lead to a significant error, requiring multiple repetitions of the same experiment to average out the

uncertainty.

One way to solve this problem is to use a system which enables real-time detection [5]. For the system governed by the equation 2.1, the rate of formation of $[AP]$ is given by

$$\frac{d[AP]}{dt} = k_1[A][P] - k_2[AP] \approx k_1[A]C \tag{2.7}$$

where C is a constant.

At the beginning of the reaction, $x(t)$ grows linearly with time. Under the assumption that the probe concentration $[P]$ is relatively constant and the reverse reaction rate is negligible, the slope $\frac{d[AP]}{dt}$ is directly proportional to the analyte concentration $[A]$. Using this section of the curve, we can obtain better estimates of $[A]$. It is also possible to have a larger dynamic range. An end-point measurement system is affected by saturation whereas a real-time system is not. For these reasons, there has been a considerable push towards developing real-time detection systems.

2.4.3 Comparison of Different Methods

Figure 2.6 provides a table comparing some of the popularly used detection methods in biosensing. Among the various methods, only optical and electrical methods have been explained as they are the most widely used.

Type	Detection Method	Principle	Label	Real-time Detection	Ease of Integration
Optical Detection	Fluorescence	Fluorescent molecules, which absorb light at a particular wavelength and emit light at a different wavelength.	Fluorescent molecules such as Cy-3, FAM	Difficult, reaction is typically stopped	Difficult, as it requires light sources and filters
	Chemi-Luminescence	Enzymes, linked to the analyte, generate light in the presence of substrate	Enzymes such as HRP	Difficult, as enzymes are large molecules and reaction is typically stopped	Easier than fluorescence, as it does not require light sources and filters
	Surface Plasmon Resonance (SPR)	SPR phenomenon occurs when polarized light, under the condition of total internal reflection, is incident on a conducting layer of gold which is sandwiched between a high refractive index sensor surface and the buffer	Not required	Can be done easily	Very difficult, as large bulky equipments are required.
Electro-chemical Detection	Amperometry	Redox reactions, happening close to the electrode surface, changes the redox current.	Redox markers such as Ferrocene, Ferrocyanide	Possible	Can be readily integrated with standard CMOS ICs
	Potentiometry	Relies on the changes in potential that happen at an electrode surface when zero or a negligible DC current flows through the system.	Not required	Possible but subject to drifts, requiring constant calibration	
	Electrochemical Impedance Spectroscopy (EIS)	EIS utilizes the impedance changes in the system that occurs in response to bio-molecular interactions occurring near the electrode-electrolyte interface.	Not required	Possible	

Figure 2.6: Comparison of different methods of detection.

2.4.3.1 Fluorescence

The most commonly optical detection method is fluorescence-based detection. The fluorescent molecules are capable of absorbing light at a particular wavelength and emitting light at a different wavelength. Fluorescence-based biosensors are popularly used in DNA microarrays ([8],[11],[14]). Fluorescence-based biosensors provide excellent specificity and sensitivity.

The fluorescence method of detection, though popularly used, has certain drawbacks. Most fluorescent detection systems use high intensity sources, optical filters and lenses that make these systems bulky and expensive, making it difficult to build compact and low-cost platforms. Also fluorescence method requires the use of labels. The use of labels has several disadvantages as explained previously in 2.4.1.

2.4.3.2 Chemi-luminescence

Chemi-luminescence is used in enzyme linked immunosorbent assays (ELISA) ([15],[16]), where a secondary probe, which can specifically attach to the analyte of interest, is labeled with an enzyme. This enzyme, in the presence of a substrate such as hydrogen peroxide, emits a large amount of light. Unlike fluorescence, chemi-luminescence does not require an external light source or any kind of optical filtering. Another application of chemi-luminescence is in pyrosequencing ([17]), where the incorporation of the correct nucleotide into a ss-DNA strand leads to emission of light. The key issue with chemi-luminescence is that it requires enzyme-labeled analytes or probes. The

enzymes are typically large in size, and can affect the probe-analyte interaction.

2.4.3.3 Surface Plasmon Resonance (SPR)

Surface plasmon resonance (SPR) phenomenon occurs when polarized light, under the condition of total internal reflection, is incident on a conducting layer of gold, which is sandwiched between a high refractive index sensor surface and the buffer ([13],[18],[19]). An evanescent wave is generated when the light strikes the glass. This evanescent wave interacts with, and is absorbed by, free electron clouds in the gold layer, generating electron charge density waves called plasmons, which causes a reduction in the intensity of the reflected light. The resonance angle, at which this intensity minimum occurs, is a function of the refractive index of the solution close to the gold layer. This useful feature permits us to monitor bio-molecular interactions, which occur at the gold surface, and alter the resonance angle.

Such SPR systems do not require the use of labels. They can be used to study the kinetics of biomolecular interactions, which enable us to estimate the disassociation constant K_d (equation 2.3) directly. Also using real-time measurements, one can arrive at a better estimate of the analyte concentration (section 2.4.2). But the major drawback in using SPR is its high cost and the necessity to use large bulky instruments. It is very difficult to integrate SPR-based sensing onto compact and portable platforms.

2.4.4 Electrochemical

Electrochemical biosensors have generated a lot of interest in recent years. Glucose biosensors, which account for 85% of the total biosensor market [20], measure the current generated by an enzyme reaction and hence are essentially electrochemical in nature. The use of electrochemical biosensors in DNA, protein and antibody detection has been demonstrated previously [21]. Since these systems are fully electronic in nature, they do not require the use of expensive optical sources or filters and can be readily integrated onto standard electronic integrated circuits.

2.4.4.1 Amperometry and Voltammetry

Amperometric sensors measure the current that is generated by a redox reaction (simultaneous reduction and oxidation reaction) involving an electroactive species [6]. The current flow is modified by redox reactions happening close to the surface of the working electrode, on which the probes are immobilized. In the case where redox labels are attached to the analytes, it is useful to cycle the voltage applied (between the working electrode and a reference electrode, which is used to set the potential of the bulk solution) and obtain the forward and reverse I-V characteristics. This method of sweeping the potential is referred to as cyclic voltammetry (CV) and it is useful in characterizing the activity of redox species.

A good example of an amperometric sensor is the glucose measurement sensor[20]. This sensor makes use of the enzyme glucose oxidase *Gox* to cataly-

ses the oxidation of glucose to gluconic acid. This oxidation reaction generates a current, which is linearly related to the glucose concentration. References [22], [23], and [24] show the use of amperometry for detection in DNA arrays. Another application is the use of CV in studying the blocking properties of surface immobilized layers [25]. The peak current in CV curve reduces with the formation of blocking layers.

Amperometic techniques provide a highly sensitive and yet a simple method to detect a large variety of biologically relevant molecules. These involve the use of redox labels such as ferrocene and methylene blue or require the use of enzymes such as glucose oxidase ([20],[22],[24]) and the flow of large currents, which can corrode the electrode surface and affect its long-term stability.

2.4.4.2 Potentiometry

Potentiometric sensing relies on the changes in the potential difference between the electrode surface and the bulk solution, caused by the changes in the concentration of the bulk solution or due to biomolecular events happening close to the surface, even when the DC current flow is zero or negligible [6].

A popularly used potentiometric sensing system is the pH sensor. The potential difference across a thin glass membrane is used to determine pH of the solution [6]. Ion-selective electrodes use different membranes to detect different ions such as nickel, manganese and mercury [26]. Today, many potentiometry based systems employ ion-sensitive field effect transistors (ISFET) to measure

pH changes and ionic concentrations. ISFETs are regular transistors, whose gates are directly connected to the sensing electrode. Reference [27] provides a comprehensive review of various applications of ISFETs in biosensing and other areas. Reference [28] describes an ISFET array which can be used for pH sensing.

Potentiometry does not require special redox molecules or enzymes in order to perform detection. Also since negligible DC current flows through the system, there is a much lesser risk of corrosion when compared to amperometric methods. One disadvantage of potentiometric sensing is that only the open circuit potential is measured and hence it is essentially a single point measurement, as compared to amperometric systems, where different input waveforms can be used to study the properties of the system. Also since the electrode surface is not kept at a well defined potential, it is more susceptible to drifts and sensitive to changes in the environmental conditions, such as temperature and humidity, requiring constant calibration [27].

2.4.4.3 Electrochemical Impedance Spectroscopy (EIS)

EIS utilizes the impedance changes in the system that occur in response to bio-molecular interactions occurring near the electrode-electrolyte interface [21]. A small signal perturbation (AC voltage) is applied across the electrode system and the resulting current that flows through the system is measured. Typically, the magnitude and phase response is measured at different frequencies and hence impedance spectrum is obtained over a wide frequency range.

EIS based biosensors take advantage of the intrinsic impedance changes in the system in response to probe-analyte binding and hence can perform label-free detection [7]. Like any electrochemical biosensor, it can be readily integrated into standard electronic integrated circuits. Also, when compared to ISFET based sensing, it provides a vast amount of information at various frequency points, making it possible to study the effect of molecular interactions and diffusion mechanisms happening at various distances from the electrode surface [21]. These advantages of EIS along with the basic concepts and important considerations involved will be explained in detail in the next chapter.

Chapter 3

Fundamentals of Electrochemical Impedance Spectroscopy (EIS)

3.1 Overview

EIS, as introduced in the previous chapter, is a powerful electrochemical method, capable of performing label-free and real-time detection. In this chapter, we will introduce the fundamental principles in designing an EIS system.

In this chapter, we begin with an explanation of the equivalent circuit model of an electrode-electrolyte system, which links the different phenomenon occurring in the electrode-electrolyte interface to the equivalent circuit components.

Generally speaking, electrochemical interactions can be categorized as Faradaic or non-Faradaic, based on the magnitude of the DC current flowing through the system. In the case of non-Faradaic interactions (negligible DC current flow), the interface capacitance plays a significant role (section 3.3). On the other hand, in the case of Faradaic interactions (DC current flow), the charge-transfer resistance plays a key role (section 3.4). Having introduced the basic concepts involved, we will discuss the underlying principles behind

the use of EIS for sensing, in section 3.5, by describing the two different mechanisms by which the interface impedance changes with probe-analyte binding.

We will then discuss the various practical considerations of EIS in section 3.6, such as the choice of the right surface, effect of linker length and concentration. Finally, we will present an antibody immunoassay, with the detailed experimental procedure and the explanation of the results obtained.

3.2 Circuit Model of an Electrode-Electrolyte System

Figure 3.1 shows a widely-used equivalent circuit used to model the electrode-electrolyte system ([6],[7],[21]). It consists of the bulk resistance of the solution R_B in series with the impedance of the electrode-electrolyte interface. The interface impedance consists of the charge transfer resistance (R_{CT}) in parallel with the capacitance of the double layer (C_{DL}). The charge transfer resistance is attributed to the interactions of ions in the solution with the electrons in the electrodes which produced a current. A net charge is relocated from the electrode to the electrolyte or vice versa [6]. The double layer capacitance is attributed to the spatial distribution of ions formed close to the electrode-electrolyte interface.

Electrochemical reactions can be classified as Faradaic or non-Faradaic based on the magnitude of DC current flowing through the interface. If no DC current flows through the interface, the reaction is referred to as non-Faradaic reaction. In the case of non-Faradaic interactions, the capacitance of the double layer plays a significant role in determining the impedance response of

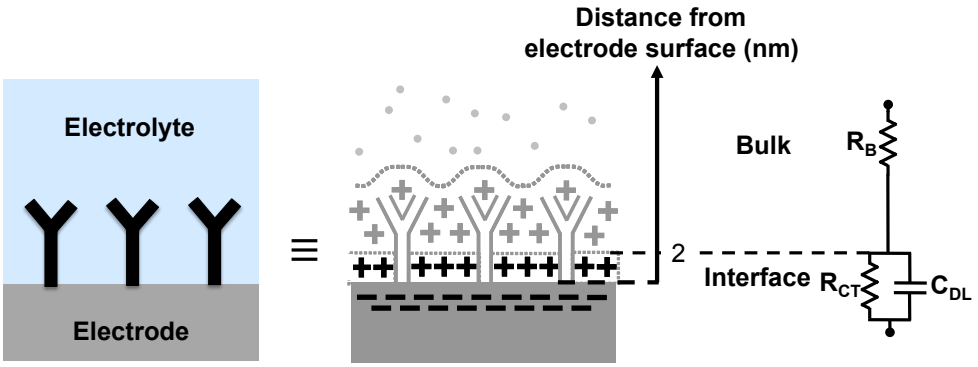

Figure 3.1: Circuit model of an electrode-electrolyte system

the system. On the other hand, if DC currents flow through the interface, then the reaction is referred to as Faradaic. In the case of Faradaic interactions, R_{CT} plays a significant role.

Figure 3.2 shows the impedance spectra obtained using the equivalent circuit model of the electrode-electrolyte system. Typically, a small signal sinusoid (amplitude $<$ 20mV) is applied as the "excitation" source and the current flowing the system at various frequency points is measured. At very low frequencies (i.e., near DC), R_{CT} dominates the response. Hence for measuring Faradaic currents, one must operate near DC, typically at frequencies $<$ 100Hz. At high frequencies, the effect of the solution resistance R_B is dominant with very little or no contribution from the interface impedance. Typically, this frequency range is not useful for studying molecular interactions happening at the intimate proximity of the interface as only the effect of the bulk resistance is observable. At intermediate frequencies, C_{DL} dominates the response and its value can be measured more accurately.

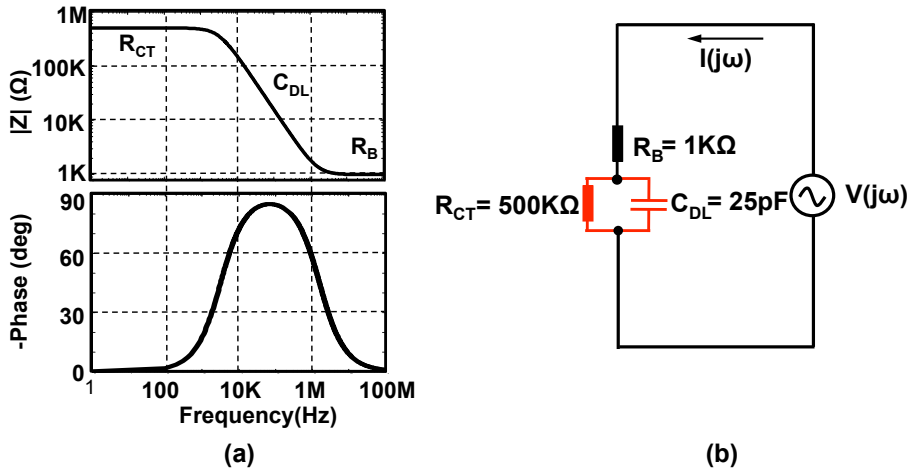

Figure 3.2: (a) Impedance spectra (b) Equivalent circuit model with assumed values for an electrode-electrolyte system.

3.3 Electrode-Electrolyte Interface Characteristics

Near the point of zero potential difference across the electrode-electrolyte interface, the interface behaves like a capacitor [6]. The charge on the metal electrode is balanced by the ions in the electrolyte, near the interface. The electrical double layer, which is formed in the solution, consists of two layers: an inner layer of specifically adsorbed ions or molecules, which is referred to as the Stern layer and outer diffuse layer of ions which extend all the way into the bulk of the solution. A charge profile example with its potential distribution is shown in figure 3.3.

The inner layer of specifically adsorbed ions or molecules is called the stern layer. The capacitance of the stern layer (denoted by C_H) is relatively constant with concentration and is primarily a function of the type of metal electrode used and ions in the electrolyte. This capacitance value is typically

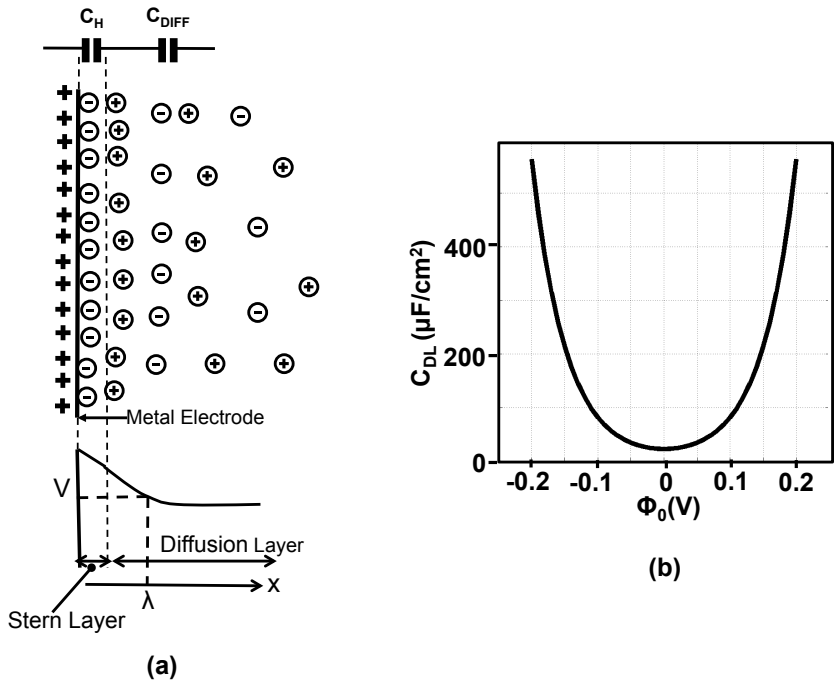

Figure 3.3: (a) Charge and potential profile at the vicinity of an electrode-electrolyte interface (b) C_{DIFF} as a function of ϕ_0

4-5 times larger than the capacitance of the diffuse layer.

The capacitance of the diffuse layer is a function of relative permittivity of the medium (ϵ_r), the potential applied (ϕ_0) and the concentration of the bulk solution (n_0) and is given by the equation [6],

$$C_{DIFF} = \sqrt{\frac{2z^2\epsilon_r\epsilon_0 n^0}{kT}} cosh(\frac{zq\phi_0}{2kT})\frac{\mu F}{cm^2} \tag{3.1}$$

where z is the charge of the ionic species involved, ϵ_0 is the absolute permittivity, q is the charge of an electron, k is the boltzmann constant and T is the absolute temperature.

For dilute aqueous solutions at $25°C$, this equation can be approximated by [6]

$$C_{DIFF} = 228zn_{sol}cosh(19.5z\phi_0)\frac{\mu F}{cm^2} \tag{3.2}$$

where n_{sol} is the bulk concentration in $\frac{mol}{l}$. For a 100mM bulk concentration, the capacitance is in order of 30 $\frac{\mu F}{cm^2}$. As evident in 3.2, C_{DIFF} is a function of ϕ_0 as well. The capacitance is minimum at $\phi_0 = 0$ which is referred by E_z, the potential of zero charge. As ϕ_0 rises or drops from this value, we can see that capacitance rapidly rises. We can clearly see, from the figure, that the capacitance is a highly non-linear function of potential. It is for this reason that the amplitude of the excitation voltage used in EIS experiments is always kept below 20mV.

The distance from the surface at which the potential drops to $\frac{1}{e}$ of its value at the surface is referred to as the Debye length. The Debye length is

given by the following expression

$$\lambda = \sqrt{\frac{1}{\frac{2n^0 z^2 q^2}{\epsilon_r \epsilon_0 kT}}} = 3.29 \times 10^{-7} z C_{sol}^{\frac{1}{2}} m \tag{3.3}$$

The Debye length λ is a good estimate of distance upto which the applied potential can change the charge distribution in the bulk solution. This translates to the distance upto which the changes in the charge distribution, due to bio-molecular interactions, can create changes in C_{DIFF}.

The total capacitance of the double layer, is given by the expression 3.4.

$$\frac{1}{C_{tot}} = \frac{1}{C_h} + \frac{1}{C_{diff}} \tag{3.4}$$

where C_h is the stern layer capacitance and C_{diff} denotes the diffuse layer capacitance. C_h is usually modelled by a constant capacitance, which is a function of the composition of the solution and the type of the metal electrode used.

3.4 Faradaic Interactions

Let us consider a simple electrode process, wherein species Ox and Re are involved in a n electron transfer process at the interface 3.5,

$$Ox + ne^- \underset{k_2}{\overset{k_1}{\rightleftharpoons}} Re \tag{3.5}$$

where k_1 and k_2 are the rate constants of the forward and reverse reactions respectively. At equilibrium, under the special condition of $C_{Ox}^* = C_{Re}^*$ (where

C^* denotes the bulk concentration), k_1=k_2 and the potential difference between the electrode and the bulk solution becomes E^0, which is referred to the standard equilibrium potential. The rate constant at the equilibrium potential is called the standard rate constant k^0. The rate constant at other potentials are given by the expressions

$$k_1 = k^0 e^{\left[-\alpha(\frac{nq}{kT})\left(E-E^0\right)\right]} \tag{3.6}$$

$$k_2 = k^0 e^{\left[(1-\alpha)(\frac{nq}{kT})\left(E-E^0\right)\right]} \tag{3.7}$$

where α is the transfer coefficient, which is derived from the energy considerations. As evident from equations 3.6 and 3.7, the rate constants are exponential functions of the $(E - E^0)$, which is referred to as the overpotential (η). The current flow as a function of overpotential is given by the expression,

$$i(t) = FAk^0 \left[C_{Ox}(0,t)e^{\left(-\alpha(\frac{nq}{kT})\eta\right)} - C_{Re}(0,t)e^{\left((1-\alpha)(\frac{nq}{kT})\eta\right)}\right] \tag{3.8}$$

where $C_{Ox}(0,t)$ and $C_{Re}(0,t)$ denotes the concentration of the oxidised and reduced species at time t. This important relation is known as the Butler-Volmer formulation and can be used to model any reaction requiring an account of heterogeneous kinetics. The current-overpotential curve is shown in figure 3.4.

Under equilibrium, the net current is zero and the electrode reaches a potential based on the bulk concentrations, C^*_{Ox} and C^*_{Re}. This exchange current is proportional to k^0 and for the particular case, when $C^*_{Ox} = C^*_{Re} = C$,

$$i_0 = FAk^0C \tag{3.9}$$

where A is the area of the electrode and F denotes the Faraday's constant. When the potential is moved away from the equilibrium potential, the Faradaic current becomes a non-linear function of the applied potential. For small values of overpotential, $e^x \approx 1 + x$ and the current can be expressed as

$$i = -i_0 \frac{nq}{kT} \eta \tag{3.10}$$

where η denotes the overpotential, $E - E^0$. The net current is a linear function of the overpotential, in a narrow potential window around E^0. The ratio $-\frac{\eta}{i}$ can be modelled as a resistor and is called the charge transfer resistance R_{CT}.

$$R_{CT} = \frac{KT}{qi_0} \tag{3.11}$$

R_{CT} provides a convenient way to model Faradaic interactions as a circuit element and will be used in our model to accurately interpret the data obtained from EIS experiments.

3.5 Impedance Based Biosensing

Impedance based biosensors take advantage of the changes in the interface impedance with the attachment of the analytes to the probes, as shown in figure 3.5. The impedance change at the interface can be caused by one of the two different mechanisms ([7],[21],[29],[30],[31],[32],[33],[34])

- *Mechanism 1:* The attachment of a large target molecule onto a probe molecule reduces the capacitance C_{DL}, due to the increase in the thick-

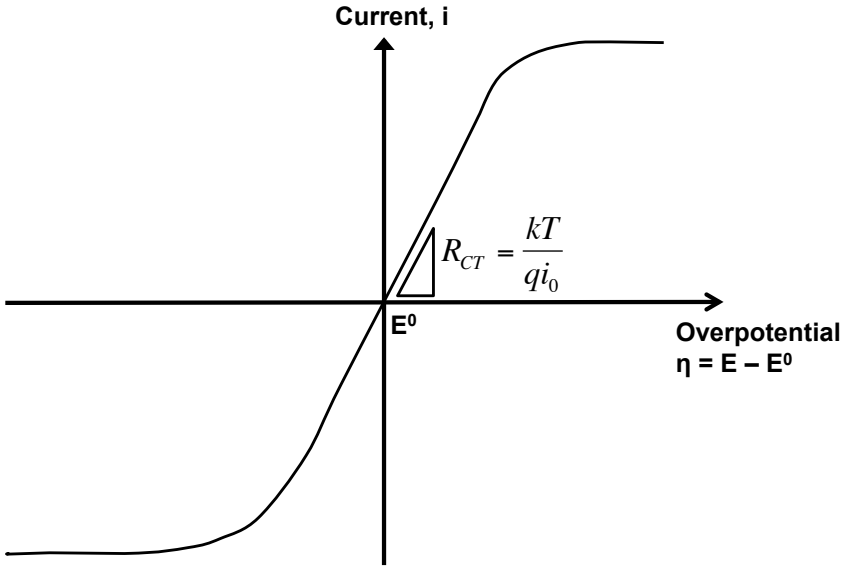

Figure 3.4: I-V for a Faradaic electrode-electrolyte system.

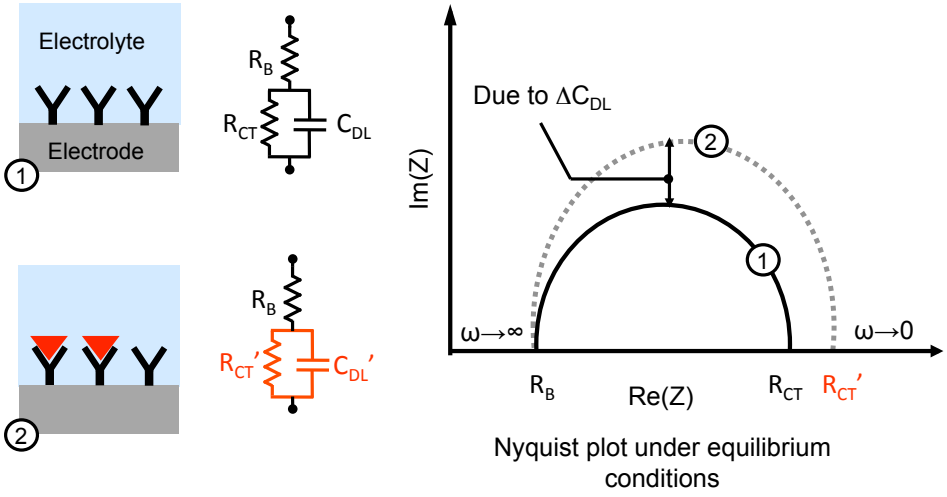

Figure 3.5: Impedance change with molecular attachment.

ness of the double layer and also due to reduction in the dielectric constant near the interface (e.g, ϵ_r of water is $\approx$81, whereas ϵ_r of organic molecules is around 2-3). Also, the larger molecular complexes formed can block the flow of the current through the interface, leading to an increase in R_{CT}. ([7],[29],[30]).

- *Mechanism 2:* The ionization of the surface immobilized groups can lead to a change in the double layer capacitance, caused by the change in the charge density profile in the vicinity of the electrode-electrolyte interface [34]. When the electrolyte contains redox molecules, the change in the surface charge density can alter R_{CT}. Since redox molecules have a positive or negative charge on them, they can be repelled or attracted by the new ions that are formed close to the surface, thereby changing R_{CT} ([7],[21]).

A good example of an impedance change due to the attachment of a large molecule (mechanism 1) is in antigen-antibody assays, where the attachment of the target antibody with an antigen probe changes the surface impedance. Reference [21] shows examples, where R_{CT} changes significantly with multiple levels of antibody attachment. In [32], the changes in capacitance with protein-antibody binding is shown and various issues in capacitance (C_{DL}) based sensing are discussed.

Reference [34] shows changes in the impedance of a surface immobilized layer with change in the solution pH due to the ionization of its terminal

group. However, the capacitance change can only be seen at very low bulk concentrations. The negative charge on the DNA molecules enables the detection of the attachment of the target single-stranded DNA (ssDNA) to the probe ssDNA (DNA hybridization) by observing the changes in redox current [21]. If a negatively charged redox marker is used such as $Fe(CN)_6^{3-/2-}$, the increase in negative charge close to the surface, with hybridization, causes an increased repulsion of the redox molecules, increasing R_{CT}. If a positively charged redox marker such as $Ru(NH)_2^{1+/2+}$ is used, a decrease in the charge transfer resistance can be observed.

3.6 Considerations in EIS Analysis

Having introduced the basic concepts, in this section, we will discuss the important considerations in EIS-based sensing such as choosing the right surface, use of the right linkers and choosing the buffer concentration.

3.6.1 Electrode Surface

As explained in the previous section, EIS systems can use electronic ICs for detection. Since EIS simply requires an electrode surface to serve as the sensor, the surface of electronic ICs can serve as transduction sites. Most ICs today are fabricated using complementary metal oxide process (CMOS) processes [35]. These processes have been optimized such that they can be used to manufacture ICs with excellent yield and reliability.

In a standard CMOS process, aluminum is typically used for building

interconnects [35]. For building an EIS biosensor, the easiest option is to use the aluminum surface as the sensing electrode, as no additional post processing steps are required. However, the usage of aluminum is generally not preferred. Aluminum surface rarely remains in its unionized state. The stability of the aluminum surface under different potential and pH conditions can be analysed using the Pourbaix diagram [36]. Pourbaix diagrams are used in corrosion studies, to analyze the stability of different materials when exposed to a wide variety of environmental conditions. Pourbaix diagrams plot the surface state for the material of interest, as a function of the half-cell potential (the potential applied between the bulk solution and the metal electrode) and pH of the buffer solution. The Pourbaix diagram of aluminum is shown in figure 3.6. Aluminum forms a protective oxide layer on its surface near neutral pH. However, this protective coating gets removed under high pH conditions and aluminum surface gets heavily ionized under basic as well as acidic conditions. Aluminum surface does not exist in its solid unionized state even under neutral pH conditions, as shown in the figure.

Another choice is to use metal oxides such as alumina and tantalum oxide for sensing. Such metal oxides are popular in ion-sensitive field-effect transistor (ISFET) sensors. Reference [27] gives a good review of ISFET based sensors and its various applications in chemical and biomolecular sensing. However, the oxide layers prevent any DC current flowing through the interface, i.e., they only permit non-Faradaic interactions. This makes the system unsuitable for Faradaic sensing. Another major consideration is the thickness

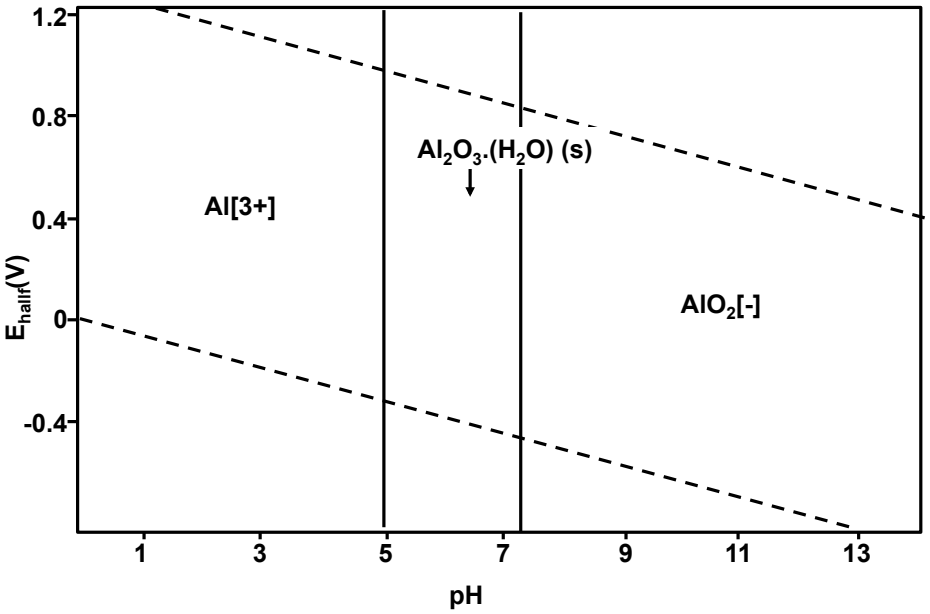

Figure 3.6: Pourbaix diagram of aluminum surface.

of the oxide layer that is being used. The thickness of the metal oxide layer should be 50nm [37]. For EIS based sensing, the increased thickness results in a lower capacitance. This will lead to a large potential drop across the oxide layer, which leads to a reduced sensitivity to molecular attachment occurring in the proximity of the surface. To increase the sensitivity, the thickness of the oxide layer needs to be minimized. However, thinner layers are unstable when large potentials are applied, as oxide breakdown and leakage can occur. Furthermore, accurate deposition of oxide layers requires the use of complicated methods, such as physical vapor deposition (PVD) or sputtering [35].

Gold (Au) is a more suitable choice when compared to aluminum as is evident from its Pourbaix diagram (figure 3.7) [36]. Gold is stable and

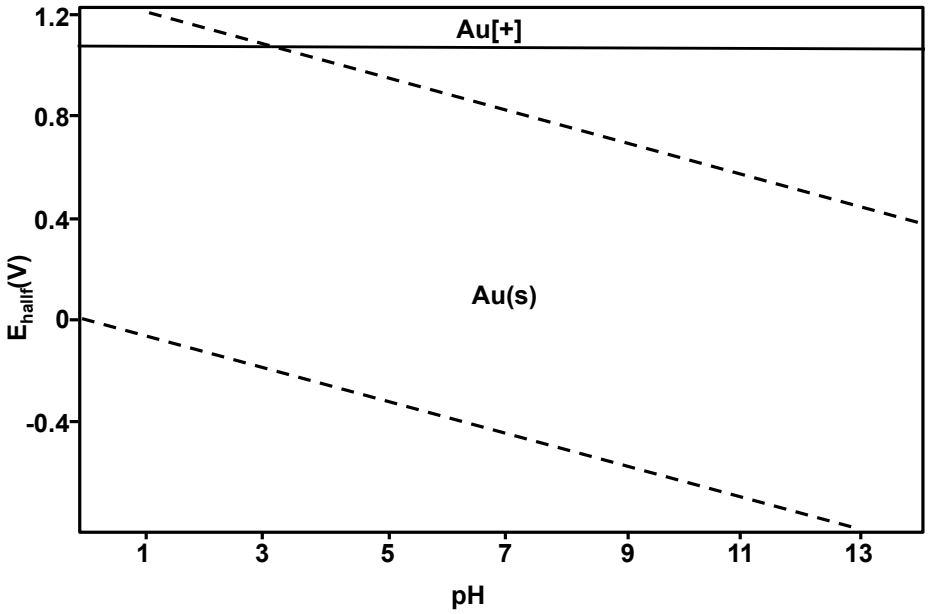

Figure 3.7: Pourbaix diagram for gold surface

stays in its solid neutral state, over a wide range of potential and pH conditions. Also, there are a number of surface immobilization protocols available for attachment of biomolecules onto a gold surface ([38],[39]). These protocols take advantage of the strong thiol bond, i.e., gold-sulphur bond. Thiolated molecules (molecules which have sulphur incorporated in them) are used in surface immobilization steps. These thiolated molecules then form self-assembled monolayers (SAM) on the gold surface. Review paper [40] discusses how thiolated carbon chains from a well-oriented, uniform, and a stable blocking layer onto the gold surface. These SAM layers can also made functional [32], making them suitable for the immobilization of a wide variety of molecules, such as proteins and antibodies, onto the gold surface.

3.6.2 Linkage of Bio-molecules onto Au Surface

Sulphur compounds (eg., thiol compounds) have a strong affinity to gold surfaces [40]. The gold-sulphur attachment occurs due to the oxidative addition of SH bond to the gold surface, followed by the reductive elimination of the hydrogen, described by

$$R - S - H + Au_n^0 \rightarrow R - S^- Au^+ \bullet Au_n^0 + \frac{1}{2} H_2 \tag{3.12}$$

where *R-S-H* denotes the thiolated molecule, and Au_n^0 refers to the gold atom at the surface, which is in its neutral state. The bonding of the SH group to the gold surface is very strong (the bond strength is approximately $10kT$) [40].

There are two different ways of attaching molecules onto a gold surface. One is the direct attachment method, where the biomolecules are chemically modified, such that they have SH groups as their terminal. One such example is the thiolated DNA strand [41]. The terminal base of the DNA molecule is modified by a SH group as shown in figure 3.8.

Protein molecules can directly attach to the gold surface due to the hydrophobic and electrostatic interactions between the protein molecule and the gold surface [42]. While this direct attachment method serves as the simplest immobilization scheme, we discovered that it is not suitable for EIS based sensing due to the following reasons:

- The surface coverage might be low. This is especially true for proteins and antibodies, which differ in shape, size, and orientation [32]. Direct

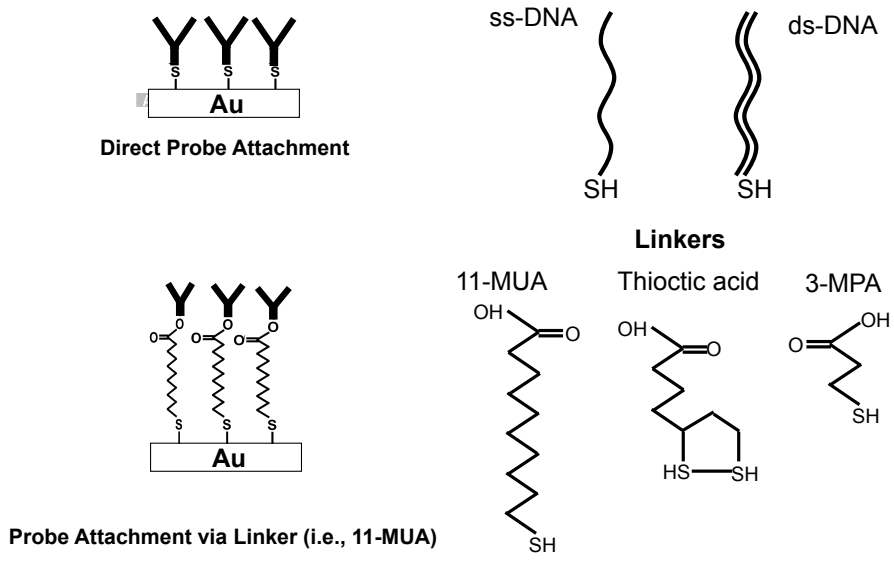

Figure 3.8: Direct and indirect attachment of molecules onto gold surfaces.

attachment is more suitable for molecules, such as DNA, which have a well defined structure [41].

- It is challenging to block the active surface sufficiently. Since the molecules can be randomly arranged over the gold surface, it is difficult to prevent the non-specific adsorption of interfering molecules [32].

- The adsorption of proteins onto the gold surface can be reversible. The proteins can be easily removed from the surface using certain solvents such as acetone and detergents such as Tween [39].

One way to overcome this issue is to use linker molecules. Functional alkanethiols serve as suitable linkers. Figure 3.8 shows some examples of functional alkanethiols (11-MUA, 3-MPA and thioctic acid). All of these have SH

groups, which can bind to the gold surface, and a functional COOH group. This COOH group can be modified to form NHS esters, using the EDC/NHS protocol [39]. The covalent binding between the NHS ester group and the amine group in proteins is irreversible and hence the use of linker molecules enhances the stability of protein attachment to the gold surface. Furthermore, the alkanethiols form self-assembled monolayers on the gold surface. These SAM layers have a well defined composition, structure, and thickness [40]. These monolayers form a pinhole free isolating molecular films. Formation of a thin, well defined monolayer close to the surface makes it possible to develop capacitance based biosensors [32].

3.6.3 Properties of Monolayers

One of the most important parameter in the selection of the right linker is its length. The length of the monolayer, formed from the linker molecule, has impact on sensitivity, stability and packing density [43]. The structure of three different linkers is shown in figure 3.8. Among the three different linkers that we have considered, 11-MUA is the longest and 3-MPA is the shortest with only 3 carbon atoms. The approximate distance between two carbon atoms in C-C chain is 0.13 Å[44].

In order to analyze the impact of monolayer length on the performance of an EIS based biosensor, we performed experiments on gold electrodes, on which we formed different monolayers. In all experiments, gold slides are first thoroughly cleaned and subsequently immersed in solutions containing

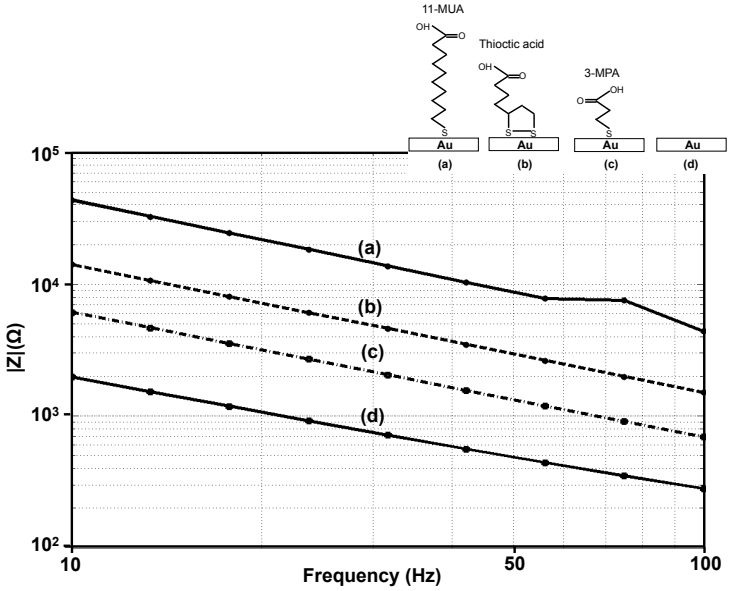

(a) Magnitude spectrum

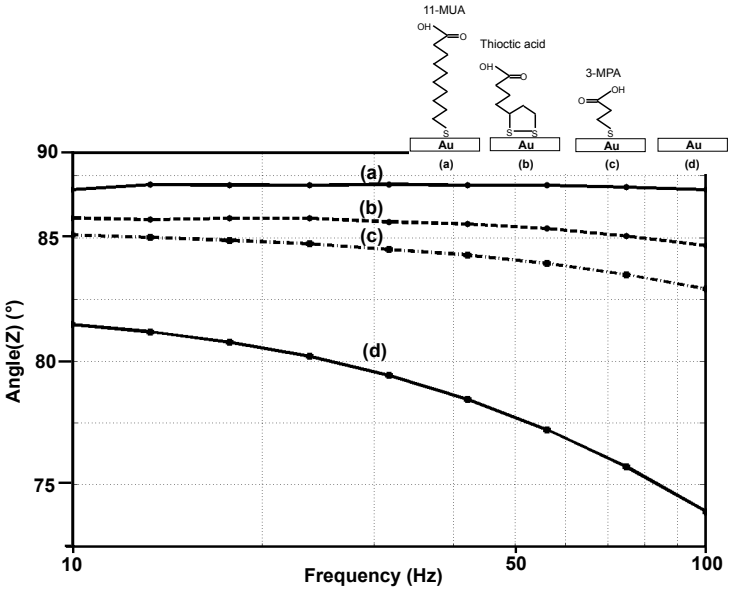

(b) Phase spectrum

Figure 3.9: Experimental determination of the magnitude and phase spectrum of electrode-electrolyte system with different monolayers immobilized onto the gold surface (a) 11-MUA (b) thioctic acid (c) 3-MPA (d) gold.

11-MUA, 3-MPA or thioctic acid. The detailed procedure for surface cleaning and monolayer formation is provided in the material and methods section of antibody assays (section 3.9.2 and Appendix). EIS experiments are then performed on these gold electrodes, with an active area of $4mm \times 4mm$, in 1X PBS (phosphate buffered saline) solution.

Figures 3.9a and 3.9b show the impedance spectra of three different monolayers (11-MUA, 3-MPA, and thioctic acid) on gold and the impedance spectrum of the bare gold surface. The phase angle of 11-MUA monolayer is very close to 90° and for a bare gold surface, it is 78° and for 3-MPA, 85°. This essentially means that the impedance is more capacitive in the case of a thicker monolayer. This translates into higher surface coverage and better blocking capacity for the thicker monolayer ([25],[44]). The magnitude of the capacitance is in the following order, Bare gold >3-MPA> Thioctic acid>11-MUA.

Apart from the fact that the shorter length leads to a higher capacitance, lower surface coverage also causes an increase in the surface capacitance. The diffusion capacitance of the metal-solution double layer is in the order of 30 $\frac{\mu F}{cm^2}$ (equation 3.4) when compared to the capacitance of 11-MUA which is around 2-3 $\frac{\mu F}{cm^2}$. So any pores in the monolayer can lead to a significant increase in the surface capacitance, since the diffusion capacitance comes in parallel with the monolayer capacitance. Another important consideration is the stability of monolayers as a function of time. We observed that the stability of monolayers of length greater than 10 carbon atoms (11-MUA in our

case) is greater than a day but for monolayers less than 10 carbon atoms in length (3-MPA and thioctic acid in our case), the impedance starts to change even after a couple of hours, because the surface coverage decreases with time, as a larger fraction of the monolayer gets removed from the surface.

Even though longer monolayers are more stable and have better blocking capabilities, one issue with longer monolayers is the reduced sensitivity to subsequent molecular attachment. There are two primary reasons why the usage of a longer monolayer leads to a reduced sensitivity. Firstly, since the protein attachment happens at the terminal of the SAM layer extending into the solution, longer the monolayer, further away is the protein (i.e., the antigen) from the surface. The potential difference between the electrode and the bulk solution drops exponentially across the diffusion layer. Therefore, the changes in the charge distribution in the diffusion layer, that occurs with antigen-antibody binding decreases exponentially as the length of the monolayer increases. Secondly, longer monolayers have smaller values of capacitance. The monolayer capacitance comes in series with the antigen/antibody capacitance, which changes when binding occurs. Smaller the value of monolayer capacitance, smaller will be the change in overall capacitance due to antibody-antigen binding.

In order to verify this theory, we performed experiments, in which the impedance is measured before and after the attachment of the protein molecules on the 11-MUA and 3-MPA monolayer. The protein molecule used in the experiments is FoS, which has a molecular weight of 78 kDa. The results

obtained are shown in the graphs 3.10a and 3.10b. The detection of FoS protein is of great importance to neurologists, as it serves as a maker for neuronal activity [45].

As evident from the figure, the change in the surface impedance can be barely seen in the case of the 11-MUA monolayer, whereas the capacitance changes by 20% in the case of 3-MPA monolayer. A similar trend can be seen in the phase response where protein attachment causes only one degree change in the phase angle for the 11-MUA monolayer, whereas for 3-MPA, the phase angle changes by 4 degrees.

3.6.4 Impact of Buffer Concentration

One of the important factors in impedance measurement is the buffer and the concentration of ions in it. The buffer concentration determines the thickness of the double layer, which is the layer of ions formed in the solution close to the electrode surface, as introduced in section 3.3. The double layer causes an exponential potential drop from the surface to the bulk solution. The Debye length, given by the equation 3.3, gives a good approximation of the distance from the surface, until which the system is sensitive to biomolecular interactions. Longer the Debye length, further away the surface we can perform detection.

The Debye length is inversely proportional to the solution concentration. For 100mM KCl, the Debye length is approximately 55nm. For $300\mu M$ KCl, the Debye length is around $1.75\mu m$. Also, the corresponding diffusion ca-

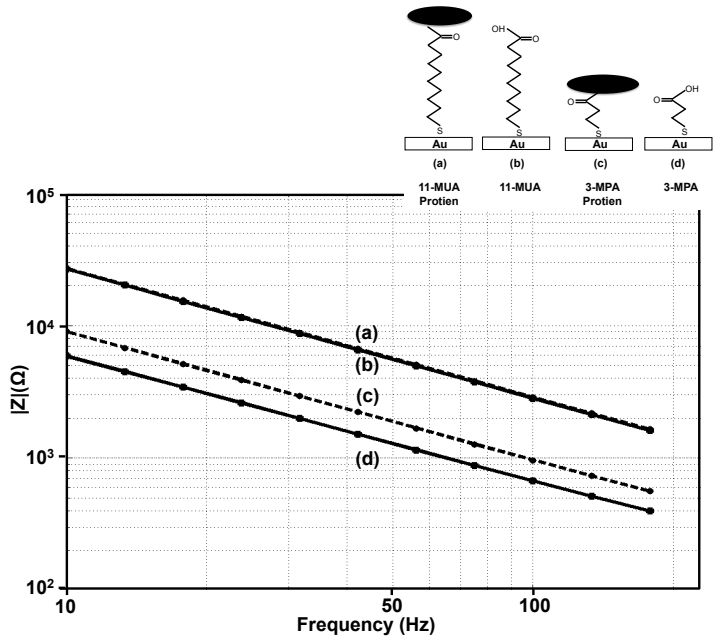

(a) Magnitude spectrum

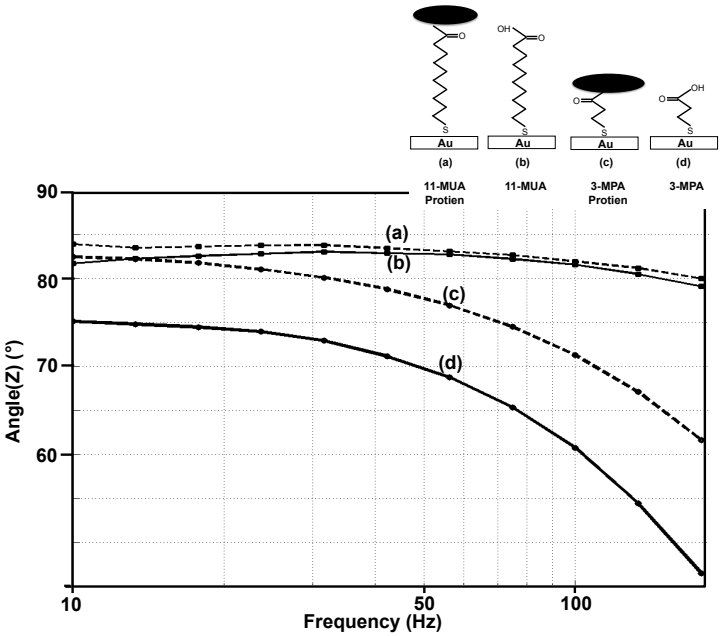

(b) Phase spectrum

Figure 3.10: Experimental determination of magnitude and phase spectrum of (a) 11-MUA with protein attached (b) 11-MUA only (c) 3-MPA with protein attached (d) 3-MPA only

pacitance decreases with this concentration, as shown by the equation 3.2. The reduced capacitance translates into higher sensitivity to subsequent molecular attachment.

Though deceasing the buffer concentration makes the system more sensitive, it might not be a practical technique for improving sensitivity. It is preferable to study the molecular interactions at physiologically relevant and compatible ionic concentrations, because the interactions can be completely different at lower concentrations. Furthermore, certain bio-molecules like DNA tend to alter their structure under reduced buffer concentrations.

3.7 Advantages of EIS Based Sensing

* *High sensitivity:* EIS is highly sensitive to molecular interactions happening close to the electrode surface. Using shorter SAM layers or lower buffer concentrations can enhance sensitivity.

* *Label-free detection:* EIS relies on the inherent properties of molecules and it does not require the use of labels ([7],[29]). This makes EIS-based sensing suitable for detection of specific molecules, such as proteins, which are difficult to label.

* *Real-time detection:* In EIS experiments, it is possible to study the evolution of the interface impedance with biomolecular interactions as function of time. Real-time detection allows us to better understand reaction mechanisms and helps us to better estimate the analyte concentration

[7].

* *Ease of Integration:* Since EIS is fully electronic in nature, EIS based sensors can be readily integrated into standard electronic integrated circuits (ICs). The use of ICs has greatly revolutionized the field of electronics, by enabling one to build compact, highly complex, and densely packed electronic systems with excellent yield and reliability. The possibility of creating integrated EIS biosensors, which utilize ICs for detection, makes EIS an attractive candidate for building portable, cost-effective platforms, which can be used in PoC applications. The concept of integrated biosensing will be discussed in detail in Chapter 5.

3.8 Challenges in EIS

- *Non-specific binding:* In order to improve EIS sensitivity, it is necessary to use shorter monolayers such as 3-MPA or thioctic acid. Shorter monolayers have poor surface coverage, permitting non-specific attachment of molecules directly to the gold surface. This can lead to large errors, especially if the sample contains a significant concentration of interfering molecules. To address this challenge, one can make use of longer monolayers, which form SAM layers with good blocking capabilities.

- *Surface cleaning:* To form reasonably uniform monolayers on the gold surface [46], strong chemical cleaning steps are required. These harsh chemical steps can require special protocols and advanced safety mea-

sures.

- *Variation with temperature and buffer conditions:* The interface impedance is a function of temperature and ionic concentration of bulk solution. In order to perform EIS experiments, it is necessary to have setups in which the temperature and humidity are tightly controlled. Furthermore, it is necessary to use buffered electrolyte, since we want the ionic concentration to remain as constant as possible.

- *Variation with antigen/antibody type:* The interface impedance varies with the type of antibody and antigen used. Biomolecules can differ in size, structure and ionic states under various electrolyte concentration and pH conditions, making it difficult to theoretically predetermine the magnitude of impedance change with antigen-antibody binding.

  In order to mitigate the effect of variations, it is advisable to make use of real-time detection, in which we measure the changes in impedance rather than the absolute values.

- *Corrosion:* In Faradic EIS-based sensing, there can be a significant DC current flow. This can result in the corrosion of the electrode, removal of the SAM layer or even removal of deposited oxide layers, which can impair experiments.

- *Stability:* Shorter monolayers are only stable for 5-6 hours after their deposition, which gives limited time to complete the required experiments.

It is possible to preserve gold slides with longer monolayers, for a longer time, but that requires the slides to be placed in an oxygen-free, cold and dark environment. This is because thiols can get oxidized if exposed to atmospheric oxygen and light for a long time.

- *Difficulty to build reusable platforms:* References [7] and [46] show that it is difficult to reuse the gold slides for new experiments. This restricts the use of EIS to disposable platforms, which are for one-time use only.

3.9 Antibody Assays

3.9.1 Significance of Antibody Assays

Today, protein and antibody detection assays are widely used in life science research and diagnostic applications. In most systems, multiple proteins and antibodies are detected in parallel. These assays help us to better understand normal and disease processes in our body [47]. Protein assays are currently being studied within several areas relevant to cancer research [47]. Some of the applications of protein/antibody arrays are [48],:

1. Antibody response profiling for studying the effect of immunization, exposure to infectious agents and determination of response to infections.

2. Cytokine profiling used in determining antibody specificity

3. Clinical biomarker development for diseases such as inflammatory bowel disease, lung and ovarian cancer.

4. Clinical diagnosis such as in Point-of-Care stroke detection, diagnosis of myocardial infection and screening of drugs of abuse.

In this section, we will build an immunoassay, which uses EIS for detection. We choose thioctic acid as the linker molecule for our experiments. Thioctic acid is chosen as the linker as it has a length of 7-8 carbon atoms, offering a reasonable trade-off between sensitivity to subsequent molecular attachment and stability of the monolayer. Thioctic acid is used in [29] for building a protein-antibody assay and reasonable sensitivity has been demonstrated. We have chosen FoS as our protein of interest. It has a molecular weight of 78 kDa and it is approximately $7.5nm$ in size. We will first study the attachment of anti-FoS IgG molecules (an immunoglobulin G antibody which can specifically attach to FoS) to the immobilized FoS. Then we will study the second level of attachment, where an anti-IgG (an antibody which can specifically attach to anti-FoS IgG) is introduced. We restrict ourselves to non-Faradaic studies, where we are primarily interested in the changes that occur in C_{DL}. Since we make use of a SAM layer of thioctic acid, R_{CT} is high, making the surface behave more like a capacitor.

3.9.2 Materials and Methods

Gold Slides: In order to perform the experiments, one requires freshly prepared gold surfaces. Typically gold is evaporated and deposited over glass slides. We made use of 500 Ågold on glass slides from Platypus technologies. It is difficult to reuse the slides, due to the rearrangement of gold atoms with

the attachment of thiolated molecules [46]. In our case, fresh slides are used for every experiment.

Surface Preparation Methods: The gold surface needs to thoroughly cleaned before the thioctic acid monolayer immobilization step. There are different cleaning strategies that can be used ([46], [49]).

1. *Acetone, ethanol wash:* Basic wash step that removes large dust and dirt particles. Ineffective in removing the organic contaminants or any kind of sulphur compounds.

2. *Air plasma:* The slide is placed in a plasma of atmospheric oxygen at a pressure of 700-1000 atm. Air plasma can rid the surface of most of the organic contaminants.

3. *SC-1 clean:* This is a strong chemical clean step using 1:1:4 ratio of ammonium hydroxide, hydrogen peroxide and water. This step strongly oxidises any organic contaminant on the surface.

4. *Piranha clean:* This is the strongest cleaning reaction for cleaning the gold surface. It completely oxidises any organic or inorganic contaminant and makes the gold surface hydrophilic by introducing OH groups on the surface.

For forming a uniform blocking layer on the gold surface, we found that either SC-1 clean or piranha clean is required. For our gold slides, we made use of SC-1 clean. This method provided reasonably repetitive results.

3.9.3 Experiments

We performed EIS experiments to study two different protein-antibody assays. The detailed protocol is provided in the appendix section. In one system, FoS protein serves as the antigen and anti-FoS IgG, which can specifically attach to FoS, serves as the antibody. In the other, anti-FoS IgG serves as the antigen and anti-IgG acts as the antibody.

The EIS is performed using a bench-top Solartron impedance analyzer. A three-electrode setup is used, in which Ag/AgCl electrode serves as the reference electrode and a platinum wire serves as the counter. A three electrode setup is commonly used, as the potential of the bulk solution can be set accurately using the reference electrode, irrespective of the magnitude of the current flow [6].

3.9.4 Results and Inference

Figure 3.11a shows the real-time experimental results that we obtained when antibody solution (anti-FoS IgG) is added to the 1x PBS buffer. The slides immersed have FoS immobilized on a thioctic acid monolayer. We can see that the surface capacitance drops with the attachment of the antibody. We can see that there is a 11 % change in the capacitance value with higher concentration ($50\frac{\mu g}{ml}$) and 8 % change with 10X dilution ($5\frac{\mu g}{ml}$). As expected, the capacitance change is larger and capacitance value drops at a faster rate when the concentration of the antibody solution used is higher (equation 2.7). The percentage change in capacitance is large, indicating that EIS has very

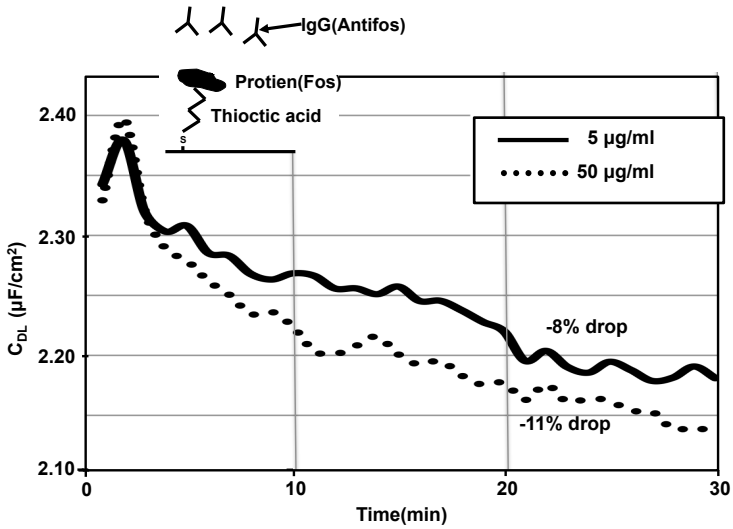

(a) Surface capacitance change with anti-FoS (IgG) attachment.

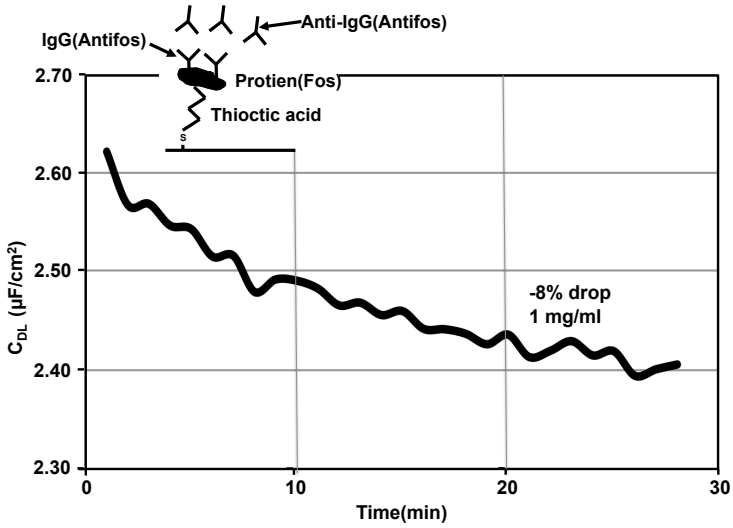

(b) Surface capacitance change with anti-IgG attachment.

Figure 3.11: Real-time EIS study is done with addition of 5 $\frac{\mu F}{cm^2}$ and 50 $\frac{\mu F}{cm^2}$ anti-FoS (IgG) solution onto a slide which has FoS immobilized on it (a) and later with the addition of 1 $\frac{mg}{ml}$ anti-IgG solution (b).

good sensitivity.

Figure 3.11b shows the changes in the surface capacitance when IgG is introduced on anti-FoS immobilized surface. The capacitance changes by 8% in 30 min. Thus we can observe that the system is sensitive for an additional level of antibody attachment. Since the two graphs shown are obtained using experiments performed on two different gold slides, the baseline capacitance in the two experiments varied by 10%.

Thus we can see that EIS is a highly sensitive method for detecting biomolecular interactions happening close to the surface and is capable of detecting multiple levels of antibody attachment. However, EIS based system has issues such as non-specific binding and varying baseline which can hamper the use of EIS based biosensors in real life applications.

In spite of its shortcomings, EIS can still provide a cheap and quick alternative to SPR based systems for studying the kinetics of molecular attachment close to the electrode surface. Also another application of EIS can be to study the quality of monolayers formed. Any holes in the monolayer can translate to large changes in the surface impedance and hence we can perform some form of quality control on the immobilized monolayers using EIS.

Chapter 4

A Comprehensive Compact Model for Distributed Electrode-Electrolyte Systems in Impedance Spectroscopy

In EIS based sensing, the impedance spectra obtained is typically fit into equivalent circuit parameters, in order to obtain a good interpretation of the physiochemical phenomenon happening close to the electrode surface. Since EIS based sensing deals with small changes in the impedance against a large electrochemical background, we need to make use of highly accurate models for electrode-electrolyte systems, so that the fitting error can be minimized.

While the impedance of parallel-plate systems can be modeled accurately, analytical models for non-parallel plate systems are of limited accuracy and computational intensive finite element method (FEM) simulations are required for accurate modeling. In this chapter, we present a general model to describe the observed admittance and noise power spectral density (PSD) of distributed electrode-electrolyte systems. The motivation behind developing this model is the accurate design and implementation of electrochemical impedance spectroscopy (EIS) transducers in biomedical and biotechnology applications. Our methodology is based on initially modeling the lumped

solid-solution interface and the distributed bulk solution independently, and subsequently merge them together using circuit theory techniques. Our preliminary results show that using this approach we achieve a superior fitting error performance compared to conventional analytical models; therefore we believe that it has the potential to become the preferred modeling technique in high-performance EIS platforms.

4.1 Introduction

Accurate modeling of micro- and macro-scale electrode-electrolyte interfaces is imperative in many biomedical and biotechnological applications. Examples are electrochemical biosensors [21], neural stimulation and recording [50], electrocardiography (ECG) [51], electroencephalography (EEG) [52], electrophoresis ([53] and [54]) environmental monitoring ([55],[56],[57]). It is widely known that among all these existing applications, the emerging area of electrochemical impedance spectroscopy (EIS) based biosensors requires the most accurate analytical models [21]. This is mainly due to the fact that EIS-based analyzers (generally referred to as impedimetric sensors [21]) rely on measuring extremely small level of impedance change (e.g., 10ppm) that occur due to the attachment or electronic interactions of specific molecules such as DNA and proteins with the solid electrode surfaces, as explained in the previous section ([21],[58],[59],[60],[61]). Such changes are typically measured over a wide range of frequencies ranging from as low as 1Hz in some systems to as high as 50MHz in certain miniaturized systems [62]. The gen-

erated impedance data is almost always fit into equivalent circuit models and modeling inaccuracies can directly affect the sensitivity of these systems.

As discussed in section 3.2, the impedance of the electrolyte is mainly resistive and a function of ions within the electrolyte. The interfacial impedance, on the other hand, is formed by the specific interaction of the ions with the electrode surface and can have impedance values quite different from the electrolyte. While the dimensions of the solution and the electrode surface can be large, the physical thickness of the interfacial layer is always small (a few Debye lengths in chemical equilibrium), in the order of tens of nanometer to a few micrometers, depending on the ionic strength of the electrolyte ([6],[63]).

The basic circuit model for a closed electrochemical circuit in EIS in general, and impedimetric biosensing in particular, consists of two electrodes (one working and the other reference) and an electrolyte sandwiched in between, as shown in figure 4.1. In this model, there are three distinct impedances in series; two for the electrode-electrolyte interfaces (one per electrode), and one for the electrolyte. While this model is widely used, it can be significantly inaccurate. The main reason is that placing these impedances in series is an oversimplification of the structure and only applicable to parallel-plate electrode-electrolyte structures, which are not widely used. One example of sensing electrode structures, which cannot be accurately modeled by such a simple circuit model is the planar sensing micro-electrodes. These inaccuracies and inconsistencies generally originate from the non-uniformities of the electric fields (i.e., fringing fields) in non-parallel-plate electrode structures as shown

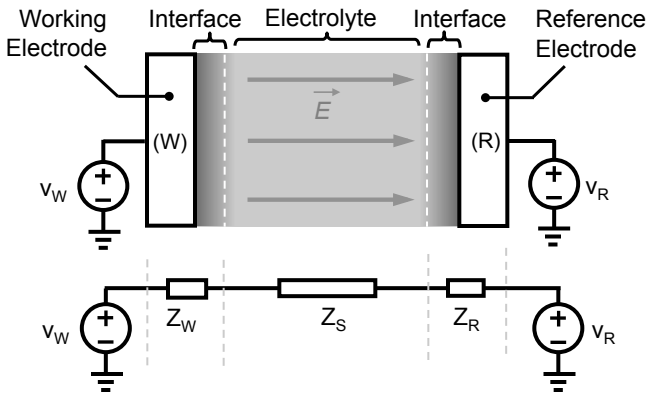

Figure 4.1: A parallel-plate electrode-electrolyte setup, where the equivalent circuit is modeled by three impedances in series.

in figure 4.2. Due to its very small thickness, the interface impedance is seldom affected by this electric field non-uniformity; nonetheless the distributed resistance of the electrolyte and the portion of it, which contributes to the overall impedance, is a strong function of the non-uniformities. Accordingly, one can say that, different electrode arrangement results in a different solution resistance and consequently different overall electrode-electrolyte admittance.

Although, analytical formulations have been reported to compute equivalent impedance (or admittance) models for non-parallel electrode systems ([64],[65]), they all exhibit limited accuracies as low as 80%. Such inaccuracies manifest themselves more when the level of fringing fields increase. For example, one of the fundamental limitations of these models is that they are incapable of describing the relationship between capturing coordinates and the impedance which is critical is micro- and nano-scale biosensors. One general approach that has been proposed to address this problem is to make use of

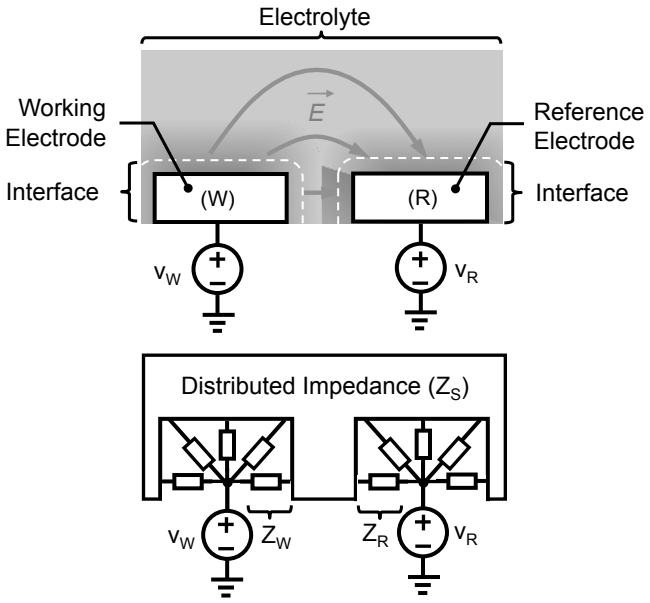

Figure 4.2: A non-parallel electrode-electrolyte system with fringing fields, where the circuit model should include distributed impedance elements.

full-scale finite-element-method (FEMs) based simulations. While such approaches are accurate, they require a significant amount of computation and cannot easily be interfaced with electronics and IC design CAD tools. Another challenge, yet to be addressed by these models, is how to effectively incorporate the electrode-electrolyte electrochemical Poisson noise [66] and thermal noise [67] into the compact models of non-parallel plate electrode systems, taking into effect the distributed nature of these systems.

The goal of this chapter is to introduce a compact modeling approach for the distributed electrode-electrolyte systems with non-uniform electric fields. The focus is not only on accurately computing the admittance of the electrode-electrolyte systems, but also computing the noise power-spectral density (PSD).

Initially in section 2 of this chapter, we introduce our proposed method and describe how the compact electrode-electrolyte interface impedance models can be coupled with the electrode topology to compute the overall observable admittance of the system in all regimes, from macro- to micro-scale. In addition, we describe the methods to incorporate noise into these compact models. In section 3, we discuss some practical biosensing implementations of the model and report our achieved results.

4.2 Model Derivation

The formulations of this section are applicable to any macroscopic electrode-electrolyte configuration. For clarity and without loss of generality however, we use the example of the widely used coplanar micro-electrodes.

In this structure, as shown in figure 4.3A, the electrodes are placed on top of a non-conductive (generally dielectric) planar substrate and the electrolyte is placed on top of it. The interface layer in our formulations is always assumed to be relatively thin compared to electrode dimensions. We also assume that the structure of this layer is in equilibrium. In our illustrations, its thickness has been exaggerated for clarity.

4.2.1 Calculating admittance

The admittance per unit area of any electrode-electrolyte interface is a function of the molecules and electric field at its liquid-solid boundary and not the electrode geometry ([6],[63]). Nonetheless, the non-uniformities within the electric field (and hence current density) are functions of the electrode geometry. In other words, the microscopic interactions within the interface are somewhat unaware of the big picture and only notice the neighboring molecules and the local electric field. From a circuit theory point of view, this suggests that the local admittance of the interface can be modeled by a lumped circuit element connecting the electrode surface to the ions at the tail of the interface layer. On the other hand, the admittance of the electrolyte (or solution) cannot be modeled by lumped circuit element since it is distributed in nature, i.e., it has a spatially varying electric field.

Now, to provide a compact model for the system, we first need to identify the terminals of the admittance element. In this paper, we assume that the admittance that we are trying to compute is between two electrode struc-

tures, which are made of a conductor with infinite conductance. Our proposed method is based on first modeling the electrolyte as a multi-port circuit network and subsequently incorporating into it, the lumped admittance model of the interface. There are two fundamental advantages to this approach. The first is that one does not require a high spatial resolution FEM simulation and a simple electrostatic simulation to calculate the solution admittance matrix is sufficient. Second, the interface characteristics in this modeling approach are decoupled from electrode topology which can provide significant insights into both design and analysis of any EIS-based biosensor.

The computational setup is illustrated in figure 4.3, where we first remove the interface layer, as we are only interested in modeling the electrolyte as a multi-port network. To create the admittance matrix, the entire area of both the working and the reference electrode is divided into N and M subsections (or grids), respectively. Subsequently, we apply voltage vectors $V_w \in R^n$ and $V_r \in R^n$ to the working (W) and the reference (R) electrodes, respectively. If we assume that the current vectors passing through the electrodes (see figure 4.3B) are $I_w \in R^n$ and $I_r \in R^n$, we can compute the admittance matrix, $Y_s \in R^{(N+M)}$, by

$$\begin{bmatrix} I_w \\ I_r \end{bmatrix} = Y_s \begin{bmatrix} V_w \\ V_r \end{bmatrix}. \tag{4.1}$$

Now, we consider the complete electrode-electrolyte system including the interface layer and its admittance. As illustrated in figure 4.3C, the interface layer can be divided into N and M subsections and its admittance is placed in series with the terminals of the multi-port electrolyte network. This

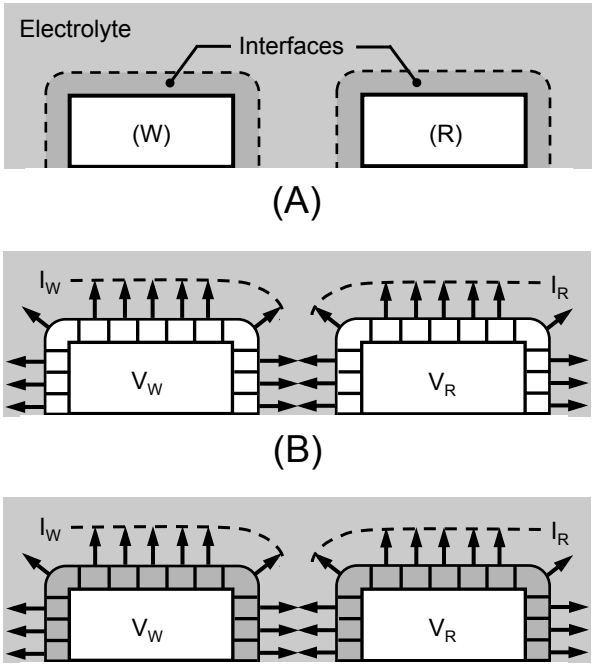

Figure 4.3: A coplanar electrode topology, where (A) the electrode are placed on a dielectric substrate and exposed to a conductive electrolyte. In (B) and (C) the computational setup for obtaining in (1) and in (10) is illustrated respectively.

approach is valid if (i) the admittance of the interface layer is uniform within each subsection, and (ii) the electric field at the surface of the electrodes is perpendicular to the surface, which guarantees no coupling between individual subsections. Based on these assumptions, we can form $Z_w \in R^{N\times N}$ and $Z_r \in R^{M\times M}$ to represent the impedance of working and reference interface layers, respectively in the form of

$$Z_w = \begin{bmatrix} Z_{1W} & 0 & \dots & & 0 \\ 0 & Z_{2W} & & \dots & 0 \\ & & \ddots & & \vdots \\ & \vdots & & Z_{(N-1)W} & 0 \\ 0 & 0 & \dots & 0 & Z_{NW} \end{bmatrix}, \tag{4.2}$$

and

$$Z_r = \begin{bmatrix} Z_{1R} & 0 & \dots & & 0 \\ 0 & Z_{2R} & & \dots & 0 \\ & & \ddots & & \vdots \\ & \vdots & & Z_{(N-1)R} & 0 \\ 0 & 0 & \dots & 0 & Z_{NR} \end{bmatrix}. \tag{4.3}$$

where z_{iW} is the impedance of the i^{th} subsection in the working electrode and z_{jR} is the impedance of the j^{th} sub-section in the reference electrode, as shown in figure 4.3C.

In figure 4.4, we illustrate the equivalent circuit network of the complete electrode-electrolyte system, where Z_w and Z_r represent the interfaces, and Y_s describes the sandwiched electrolyte. Using 4.1 to 4.3, we can calculate the voltage of the electrolyte at the edge of the interface layer of the working

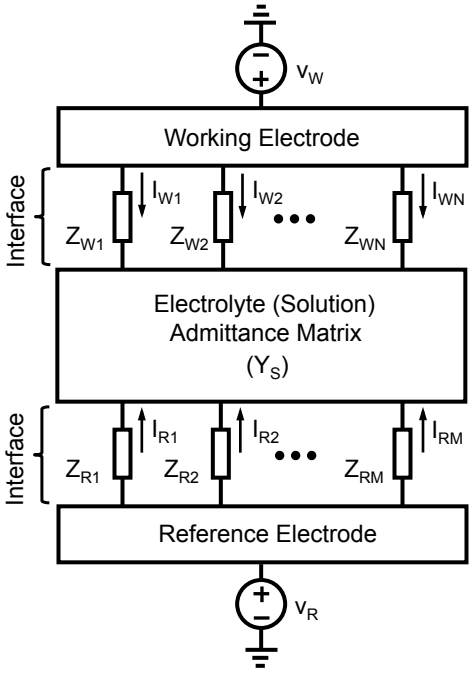

Figure 4.4: The equivalent circuit model for the distributed electrode-electrolyte system.

electrode, $V_{EW} \in R^N$, using

$$V_{EW} = V_W - Z_W I_W, \tag{4.4}$$

and similarly for the reference electrode we can define, $V_{ER} \in R^N$, and formulate it by

$$V_{ER} = V_R - Z_R I_R, \tag{4.5}$$

Based on the definition of Y_S , we have

$$\begin{bmatrix} I_W \\ I_R \end{bmatrix} = Y_S \begin{bmatrix} V_{EW} \\ V_{ER} \end{bmatrix}, \tag{4.6}$$

and since Y_S is invertible, we can get

$$\begin{bmatrix} V_{EW} \\ V_{ER} \end{bmatrix} = Y_S^{-1} \begin{bmatrix} I_W \\ I_R \end{bmatrix}. \tag{4.7}$$

Next, by using 4.4 and 4.5, we can modify 4.7 as

$$\begin{bmatrix} V_W - Z_W I_W \\ V_R - Z_R I_R \end{bmatrix} = Y_S^{-1} \begin{bmatrix} I_W \\ I_R \end{bmatrix}, \tag{4.8}$$

$$\begin{bmatrix} V_W - Z_W I_W \\ V_R - Z_R I_R \end{bmatrix} = \begin{bmatrix} Y_A^{-1} & Y_B^{-1} \\ Y_C^{-1} & Y_D^{-1} \end{bmatrix} \begin{bmatrix} I_W \\ I_R \end{bmatrix}, \tag{4.9}$$

where $Y_A^{-1} \in R^{N \times N}$, $Y_B^{-1} \in R^{N \times M}$, $Y_C^{-1} \in R^{M \times N}$ and $Y_D^{-1} \in R^{M \times M}$ are all sub-matrices of Y_S^{-1}. By rearranging 4.9, we can come up with the relationship between electrodes voltages and current as

$$\begin{bmatrix} I_W \\ I_R \end{bmatrix} = \begin{bmatrix} Z_W + Y_A^{-1} & Y_B^{-1} \\ Y_C^{-1} & Z_R + Y_D^{-1} \end{bmatrix}^{-1} \begin{bmatrix} V_W \\ V_R \end{bmatrix} = Y_T^{-1} \begin{bmatrix} V_W \\ V_R \end{bmatrix}, \tag{4.10}$$

where we define Y_T as the comprehensive admittance matrix of the electrode-electrolyte system.

In most practical applications where the electrode is a good conductor (i.e., large conductivity, $\sigma \to \infty$), the potential is identical everywhere across the electrode surface which means that all entries within V_W and V_R are the same and equal to v_W and v_R, respectively. In such situations, we can model the electrode-electrolyte system as a two terminal circuit element between the working and reference electrodes. Furthermore, we can associate a single value for the observed admittance between the two electrodes. We denote this

admittance by y_t , which is defined as the ratio of the total current flowing between the electrodes divided by the applied voltage across them, i.e., $v_W - v_R$. Now if we realize that the total current going through the working and reference electrode contacts is the sum of the entries in I_W and I_R , we can simply formulate y_t by

$$y_t = \frac{tr\left(I_W\right) - tr\left(I_R\right)}{v_W - v_R} \tag{4.11}$$

where function $tr\left(X\right)$ computes the trace of X.

4.2.2 Deriving the noise PSD

Let us first consider the effects of thermal noise (i.e., Johnson-Nyquist noise [68]) in the electrode-electrolyte system. According to the fluctuation dissipation theorem [69], the observed thermal noise of a macroscopic conductor, can be directly derived from the losses within the system, i.e., electrical resistance. Hence in our formulation, the real part of y_t is sufficient for its calculation. Hence, we first consider y_t as $Re\{y_t\}$ in parallel with $Im\{y_t\}$ (see figure 4.5). The equivalent thermal noise within this system can then represented by a noisy current source, i_{nt}, in parallel with $Re\{y_t\}$, where the single-sided PSD of i_{nt}, denoted by $\overline{I_{nt}^2\left(\omega\right)}$, is

$$\overline{I_{nt}^2\left(\omega\right)} = 4kTRe\{y_t\} \tag{4.12}$$

where k is the Boltzmann constant and T is the absolute temperature.

Additionally, in electrode-electrolyte systems, under certain conditions (e.g., presence of Faradaicaic currents), we will experience shot noise [66]. In

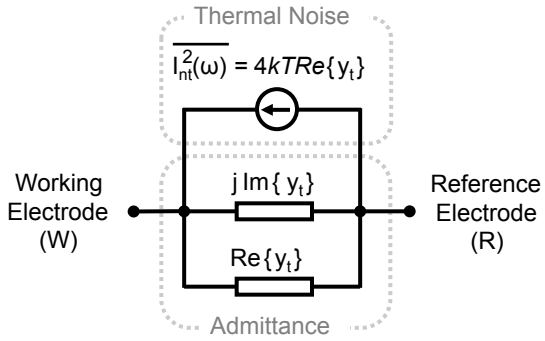

Figure 4.5: Electrode-electrolyte compact model with thermal noise.

order to incorporate this into our model, we place noisy small-signal current sources in parallel with each subsection element of the interface impedance (see figure 4.6). As with the traditional noise analysis methods used in circuits, we can use superposition theorem and make V_W and V_R equal zero, to calculate the effect of these noisy current sources on output current flowing from the working to the reference electrodes.

As shown in figure 4.6, we can create noise current matrices, i_{nW} and i_{nR}, for both the working electrode and reference electrode such that

$$i_{nW} = \left[\begin{array}{cccc} i_{nW1} & i_{nW2} & \dots & i_{nWN} \end{array} \right], \tag{4.13}$$

and

$$i_{nR} = \left[\begin{array}{cccc} i_{nR1} & i_{nR2} & \dots & i_{nRM} \end{array} \right]. \tag{4.14}$$

Now, by converting the parallel noise current sources (Norton model) into the Thevenin model and substituting them in place of V_W and V_R, we can calculate the noise current vectors, I_{nW} and I_{nR}, observed at working and reference electrodes by using the following equation

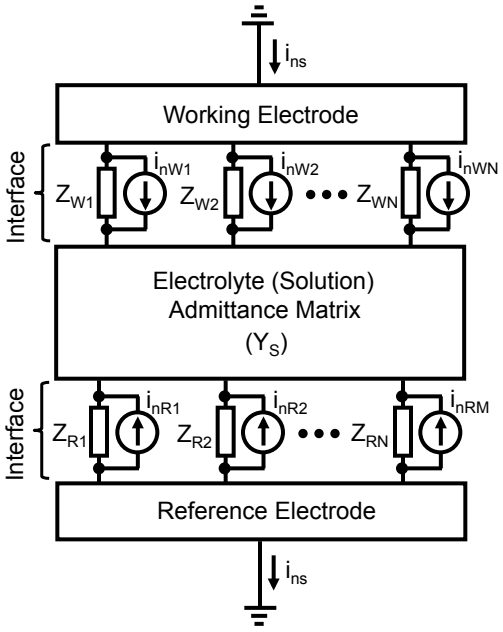

Figure 4.6: The equivalent circuit model for the distributed electrode-electrolyte system with interfacial shot-noise.

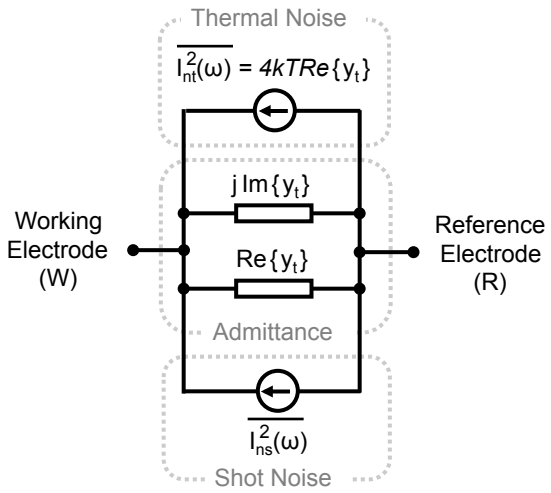

Figure 4.7: Electrode-electrolyte compact model with thermal and shot-noise sources

$$\begin{bmatrix} I_{nW} \\ I_{nR} \end{bmatrix} = Y_T \begin{bmatrix} -Z_W i_{nW} \\ -Z_R i_{nR} \end{bmatrix}. \tag{4.15}$$

The total shot noise current flowing between the working and reference electrodes, i_{ns}, becomes

$$i_{ns} = tr\left(I_{nW}\right) - tr\left(I_{nR}\right). \tag{4.16}$$

By using 4.16, we can also compute the PSD of i_{ns}, denoted by $\overline{I_{ns}^2\left(\omega\right)}$. In most practical electrode topologies we can safely assume that the entries of i_{nW} and i_{nR} are uncorrelated, which in turn makes the PSD calculation straightforward. It is also important to realize that the shot noise is uncorrelated with the thermal noise in the system. As a result, we can use superposition to calculate the overall noise PSD as illustrated in figure 4.7.

4.3 Model Implementation and Discussion

In this section, we implement the model to analyze the admittance characteristics of a coplanar electrode structure. Our goal is to use this example to demonstrate the capabilities of this modeling approach, discuss the insights that the model can provide, and finally point out its limitations.

4.3.1 Admittance

Table 4.1: Simulation parameters.

Parameter	**Value**
Interface Capacitance (C_{int})	$2\mu F/cm^2$
Electrolyte Conductance (σ_S)	$4S/m$
Interface Conductance (σ_{int})	$10^{-4}S/m$
Electrolyte Permittivity (ϵ_S)	81
Substrate Permittivity (ϵ_{sub})	11
Electrode Conductance (σ_m)	$10^7S/m$

The dimensions of the coplanar system under consideration are shown in figure 4.8 and Table I provides the properties of the materials used in this example. The interface is modeled as a lossy capacitor consisting of a parallel combination of a resistance and a capacitor. Such a model is general enough for modeling both Faradaic and non-Faradic interactions that happen close to the interface. The permittivity of the substrate is set to that of silicon and the solution properties are set to the electrical properties of sea water, which closely matches the properties of commonly used biological buffers.

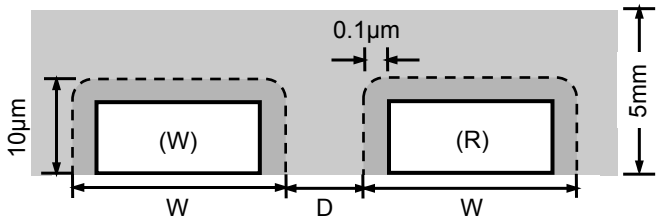

Figure 4.8: Example system under consideration.

In order to obtain the admittance matrix, Y_S, the interface layer is removed as discussed in section 2. The elements in the conductive subsections are separated by a thin layer of air (not shown in the figure) in order to prevent element-to-element direct conduction. The 2-D FEM simulation is carried out using COMSOL multiphysics simulation environment (COMSOL, MA, USA). We observed that in this example, $\frac{\sigma}{\omega\varepsilon} \ll 1$ for frequencies up to 1 MHz, which means that in this frequency range, the conduction current dominates displacement current. As a result, it is sufficient to obtain Y_S at DC and use it in calculation of y_t for frequencies up to 1MHz (the frequency range upto which the condition $\frac{\sigma}{\omega\varepsilon} \ll 1$ is satisfied). This particular simplification significantly reduces the simulation time. Now by using 4.11, we can compute y_t. For evaluating the accuracy of our model, the results are compared with a fully distributed model, where the interface characteristics are incorporated into the COMSOL model and y_t of the entire system is computed using computationally intensive FEM simulations.

For estimating the accuracy of our compact model, a fully distributed model is taken as a reference. In this model, the interface characteristics are

incorporated into the COMSOL model by introducing the equivalent loss and relative permittivity of the interface layer. COMSOL generated a mesh with atleast 10000 nodes for this model. Next, y_ts of the entire system are computed using FEM simulations for each frequency point of interest.

In order to compare the accuracy of our model with the traditional analytical models, we define the error parameter, S, by computing the complex non-linear least square error for each model [70]. The admittance values computed using the fully distributed model is taken as the correct value. The error is then computed as the sum of squares of normalized error in the real and imaginary parts of the admittance values, calculated at 70 frequency points between 100Hz and 500kHz with a resolution of 20 points per decade. The following equation describes how S is calculated:

$$S = \sum_i \left(\frac{Re\{y_t(\omega_i)\} + Re\{y'_t(\omega_i)\}}{Re\{y'_t(\omega_i)\}} \right)^2 + \sum_i \left(\frac{Im\{y_t(\omega_i)\} + Im\{y'_t(\omega_i)\}}{Im\{y'_t(\omega_i)\}} \right)^2 \tag{4.17}$$

where $\{y_t(\omega_i)\}$is the admittance values at frequency ω_i computed using our model and $\{y'_t(\omega_i)\}$ is the same parameter derived from the fully distributed model.

In this paper, we consider four setups with different values of the electrode width, W, and electrode spacing, D. In addition, three different numbers of sub-sections on each electrode are considered (N=20, 40, and 50) to examine the trade-offs between the model complexity and the accuracy. In order

to compare the performance of our models with existing analytical models in electro-analysis, we picked two popular analytical models from the literature ([6],[63]) (see figure 4.10). The first model is the RC series model, denoted by 1-(RC), in which R_d and C_d constitute the admittance of the interface and R_s and C_c constitute the solution admittance. The second model uses constant phase elements (CPE) to model the interface and is denoted by 2-(CPE). CPEs have been used routinely to fit electro-analytical experimental impedance data ([6],[63]), as it has been empirically shown that it can take into account the effects of distributed elements to some extent.

From the table in figure 4.9 where S for different models are reported, we can see that our modeling approach has significantly better performance compared to the existing analytical models. As expected, as the complexity of our model increases (i.e., N increases), the error decreases. However, improving the accuracy leads to larger matrices and longer simulation times, so there is a fundamental trade-off between the accuracy of the model and the amount of required computation. The fully-distributed FEM simulation for 70 frequency points takes 1.5 hours in a computer with a 8 core processor and 72 GB RAM whereas the computation done using our model, for N=50, takes less than 30 seconds.

In figures 4.11 and 4.12, we have plotted the normalized magnitude error and phase errors, respectively, to compare the results of all the models. As evident, even for the N=20 model, it is possible to obtain magnitude errors less than 1% and phase errors less than 0.5 degree, which is a significant

Dimensions		Least-Square Error (S)				
W (mm)	D (mm)	Analytical Model		Our Model		
		1-(RC)	2-(CPE)	N = 20	N = 40	N = 50
1	2	1.1260	0.4541	0.0706	0.0103	0.0083
1	3	1.0256	0.4184	0.0775	0.0114	0.0078
1.5	2	1.5423	0.4877	0.1448	0.0293	0.0124
1.5	2	1.3732	0.4418	0.1416	0.0326	0.0125

Figure 4.9: Fitting error (S).

improvement over the conventional analytical models.

One important limitation in our models is that it has an upper frequency limit. This originates from to the fact that Y_S is computed at DC and using a single FEM simulation. If we require $y_t(\omega)$ at higher frequencies, additional FEM simulations need to be performed, which increases the overall computational time. Another important observation is that for conductive solutions, where $\frac{\sigma}{\omega\varepsilon} \ll 1$ remains valid, the entries of Y_S, scale with σ. This property can significantly reduce the simulation time, as it is sufficient to run only one initial FEM solution for each electrode topology.

It is important to emphasize at this point that the described modeling approach in this paper is general and not restricted to coplanar electrode systems. This model has been tested with non-coplanar systems and the results are always better than that obtained from the analytical models. As predicted in the previous sections, the relative error between the analytical models and our approach increased, as the non-uniformity of the electric fields increased.

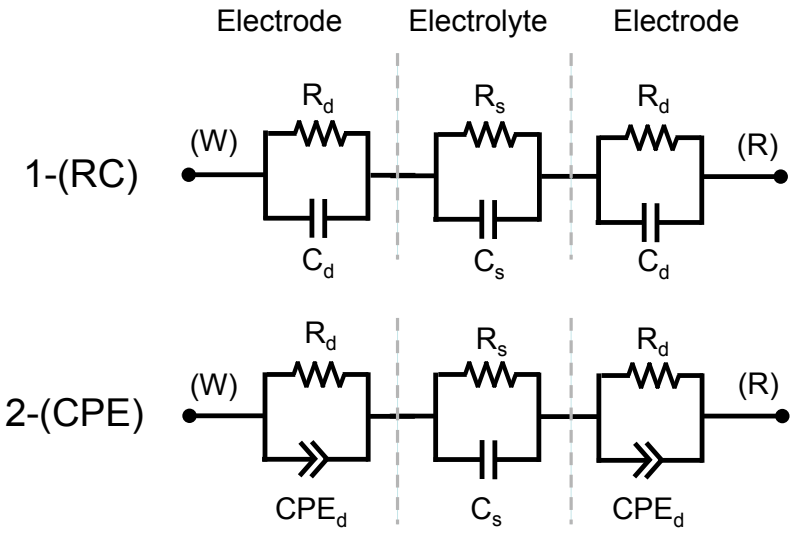

Figure 4.10: Analytical circuit models

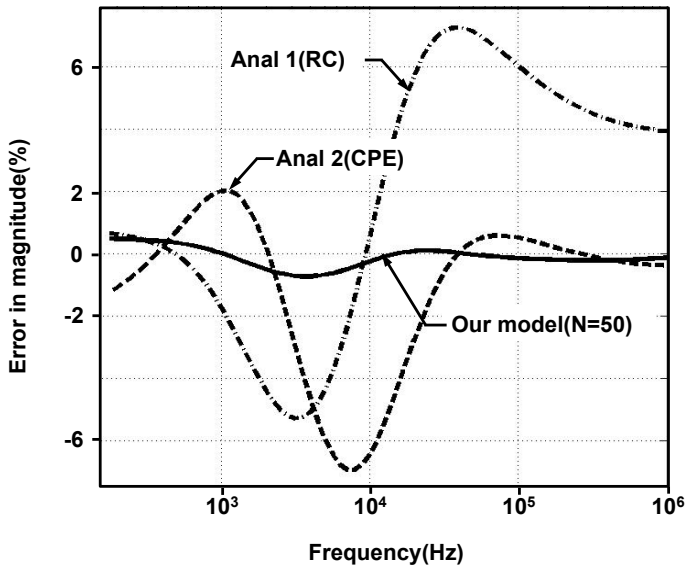

Figure 4.11: Normalized magnitude errors in models.

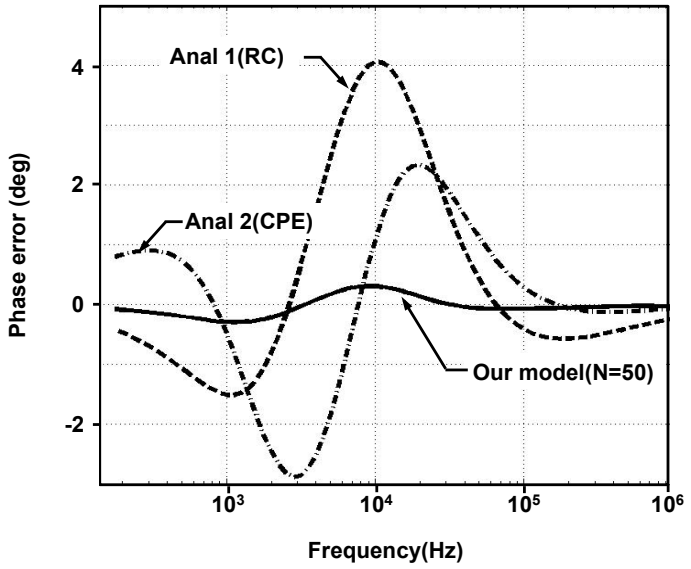

Figure 4.12: Phase errors in models.

4.3.2 Noise PSD

To compute the noise current source, we need to use equations 4.12 and 4.16. The calculation of the thermal noise component from $Re\{y_t(\omega)\}$ is straightforward, but the shot-noise component (if any) requires prior knowledge of the vectors i_{nW} and i_{nR} as well as their PSD. As an example here, we assume that we have an electrode-electrolyte interface, which experiences a diffusion-dominated redox Faradaic current. Based on [71], if the DC current flowing through each subsection of the electrode has amplitude I, then the observed PSD of the current shows a 1/f noise behavior in the form of

$$\overline{I_n^2(\omega)} = 2zqI\frac{\pi \mid erf\sqrt{j\tau_t\omega} \mid^2}{4\sqrt{\tau_t}\omega}, \tag{4.18}$$

where z is the average unit of charge of the electro-active species participating in the redox process, and τ_t is the expected transport time.

In figure 4.13, we show the computed PSD of this system, where the thermal and shot-noise components are also plotted. The total noise PSD exhibits a 10dB/decade slope (1/f noise) at low frequencies. As the frequency increases, the contribution of the interface capacitance to the overall admittance of the system goes down, which reduces the contribution of the shot noise current source to the overall output current. Nevertheless, it can be seen that, in this region the thermal noise component increases, and eventually dominates the noise PSD and forms a constant noise floor at higher frequencies. The shot current amplitude used is 1pA. The simulation is performed for W=1mm and L=1mm model. The relaxation time constant, τ_t, is set to 1s.

4.3.3 Coordinate-dependant Surface Bindings

In all impedimetric biosensors, the probe-analyte bindings can take place at different coordinates along the interface. If the current distribution is different at these locations, it is expected that the impedance changes should be coordinate-dependant, which essentially means that probe-analyte bindings have a coordinate-dependant gain. Although conventional analytical models are incapable of incorporating this phenomenon, this effect can be studied using our model.

In figure 4.14, we show a system where surface impedance changes occur at three different locations on the surface of the working electrode. We model

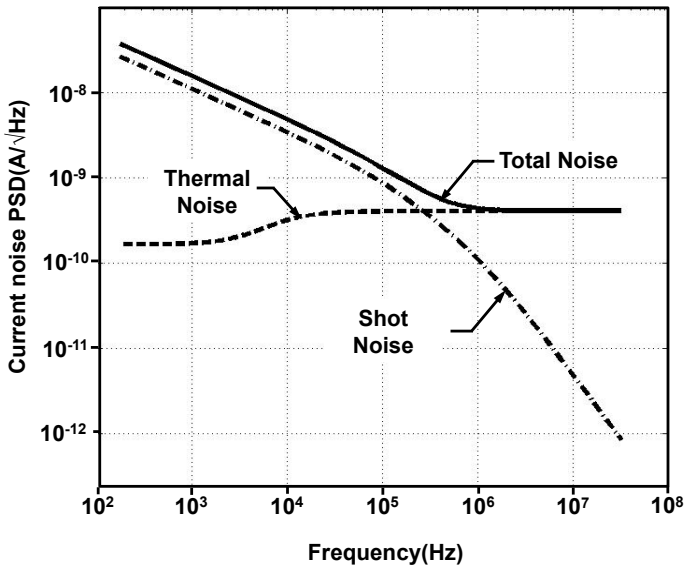

Figure 4.13: Output current noise spectral density (PSD) of the electrode-electrolyte system

binding by decreasing the local capacitance of the associated sub-section by a factor of 10. Subsequently, we calculate the overall admittance and normalize them with respect to the original admittance value. From the normalized impedance change plots of figure 4.15, we can easily see that at certain frequencies, the difference can be in order of 0.5%. This result is particularly important for two main reasons. The first is that, we need to recognize that spatial dependence of the transducer gain is an important source of variation in all impedimetric biosensors, especially when we have fringing fields or small micro-transducer structures with small capturing surface areas. Secondly, through proper design, we might be able to create special transducers capable of associating the impedance change to the reaction coordinate. This

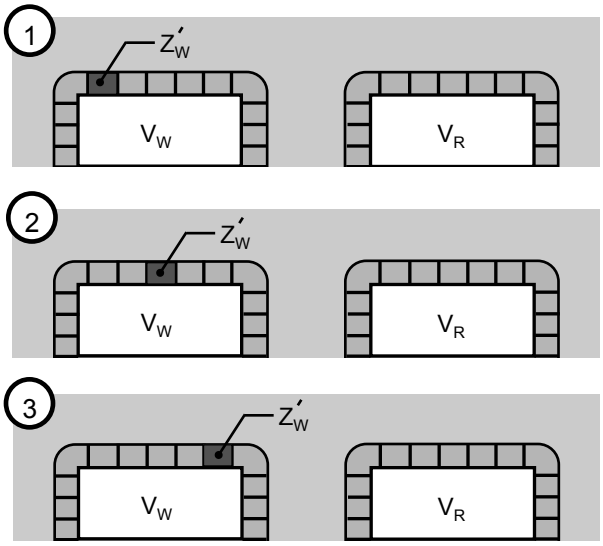

Figure 4.14: Example of coordinate-dependant impedance changes in an electrode electrolyte system

essentially creates a new detection paradigm in EIS and is extremely useful for monitoring electrode-electrolyte systems.

4.3.4 Conclusion

In this chapter, we have introduced a compact model, which can be used to accurately model distributed electrode-electrolyte systems. The compact model is built by initially modeling the lumped solid-solution interface and the distributed bulk solution independently, and subsequently merging them together using circuit theory techniques. This model has a much better accuracy when compared to purely analytical models and at the same time, requires much lesser computational time and resources, when compared to a

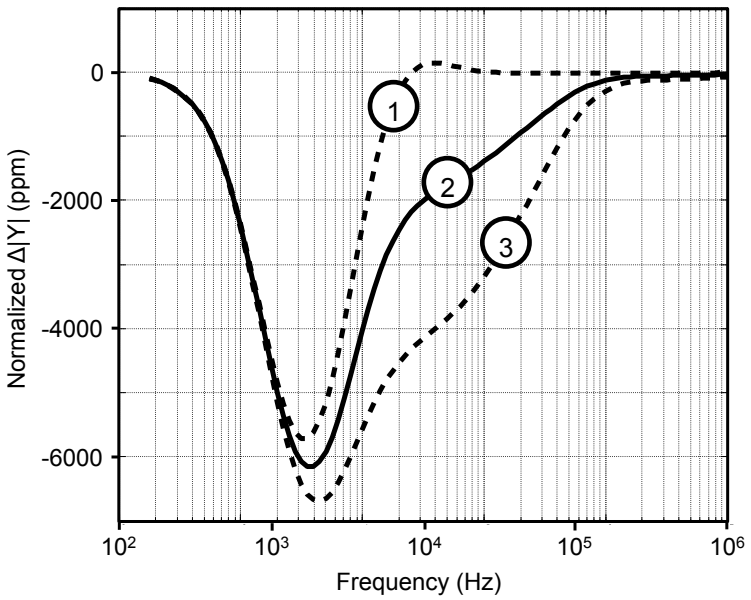

Figure 4.15: Magnitude response for the example system.

fully distributed model. Furthermore, the model can be used to estimate the noise PSD of the system, including the effects of both thermal and shot noise. The development of such a model, is important in the design of integrated biosensor systems, in which large arrays of coplanar electrodes typically serve as sensing sites.

Chapter 5

An Integrated CMOS EIS biosensor

5.1 Biosensor Integration

In recent years, there has been a push towards building compact, high-performance, and cost-efficient biosensor platforms which can be readily used in point-of-care (PoC) devices for applications such as molecular diagnostics and environmental monitoring. Such detection platforms need to have a very wide dynamic range, but their performance, as of today, is limited by the biochemical aspects of the system and not by the limited dynamic range of the electronic sensors or detectors. Additionally, these detection platforms must be considerably robust, to be deployed at the PoC settings. Finally, they must have the capability to detect multiple analytes in parallel. For example in DNA microarray applications, upto 100,000 unique DNA strands need to be detected in parallel [11].

One solution is to utilize complementary metal oxide semiconductor (CMOS) fabrication processes, which are the most robust and widely used fabrication processes in the semiconductor industry, for manufacturing biosensors. The rationale behind this, as opposed to using MEMS or other processes is the unmatched yield, cost-efficiency, and the integration capabilities of CMOS

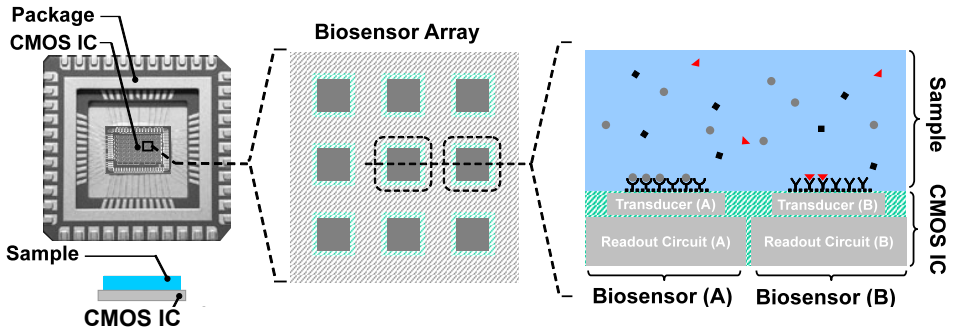

Figure 5.1: Anatomy of an integrated biosensor.

processes. Hence, integrated CMOS biosensors are defined as sensors which use CMOS fabrication processes to create massively parallel biosensors. In contrast to conventional biosensor systems where incubation and detection are carried out independently, the biomolecular assays are directly built on top of the detector, i.e., an integrated circuit (IC), combining capturing and detection together in a single platform. Furthermore, the CMOS fabrication process greatly improves cost-efficiency and manufacturability.

A typical setup for an integrated biosensor is shown in figure 5.1. The CMOS IC is placed in a special package and the sample containing the analytes is directly placed on top of the CMOS die. The chip, almost always, has an array of pixels, each consisting of a transduction element, along with the integrated readout circuit. The transducer can just be an electrode for an electrochemical biosensor, or a photodetector in an optical biosensor. Depending on the application, different probe molecules can be immobilized on the different transduction sites, accommodating parallel detection of multiple analytes. The readout circuit performs the task of low-noise signal amplification

and some amount of signal processing to make the transduction measurable. Depending on the sensor size, available silicon area, and CMOS process used, analog-to-digital converters and other signal processing blocks can also be integrated.

5.1.1 Existing CMOS Integrated Biosensors

Table 5.1 provides a list of CMOS integrated biosensors that have been reported. Among the different detection methods, optical, magnetic, and electrochemical methods are the most widely implemented. The important inference is that the CMOS fabrication processes can, in fact, be used for manufacturing biosensors, with no or a few additional post processing steps [72].

Optical biosensors utilize simple photodiodes for sensing, and use a capacitive trans-impedance amplifier (CTIA) structure to measure the current generated [72]. Reference [73] describes a bioluminescence detection sensor, which can be used to perform DNA sequencing, while, [14] describes an integrated florescence biosensor, which has an optical filter integrated on top of the CMOS chip and has a CTIA, a pre-amplifier and a time-to-saturation ADC inside every pixel. Finally in [79], an optical biosensor is described, which utilizes a first order sigma-delta loop to achieve a wide optical detection dynamic range. In [74] and [75], magnetic biosensors based on magnetic nano-particles are built, which act as molecular reporters.

Electrochemical detection methods or electroanalysis are popular choices

Table 5.1: Survey of CMOS integrated biosensor.

Reference (ISSCC/JSSC)	**Detection Modality**	**Assay**	**Label/Reporter**
Eltoukhy,2004[73]	Optical	Bioluminescence	Luciferase Enzyme
Jang,2009[14]	Optical	Fluorescence	Cy3
Wang,2009[74]	Magnetic	Nano-Particle	Paramagnetic beads
Sun,2009[75]	Magnetic	Nano-Particle	Ferrite beads
Schienle,2004[76]	Electrochemical	Cyclic Voltammetry	Redox enzyme
Levine,2008[22]	Electrochemical	Cyclic Voltammetry	Ferrocene redox label
Heer,2008[77]	Electrochemical	Cyclic Voltammetry	Polypyrrole redox polymer
Stagni,2006[78]	Electrochemical	Capacitance-based	NA
Hassibi,2006[71]	Electrochemical	Electro-analytical	NA
This work	Electrochemical	EIS	NA

for building integrated biosensors, as all signals are fully electronic, eliminating the need for complex light sources, optical filters or lenses. Cyclic voltammetry is essentially an amperometric scheme, in which the excitation voltage is cycled between two limits and the current flowing through the system is measured. In [76], electrochemical redox cycling process is used for detection. In [22], an array of 16 gold electrodes and integrated potentiostats, consisting of current-input ADCs, are used for detection. In [77], a first-order sigma-delta ADC which makes use of the electrode-electrolyte capacitance as the integrator, is used. This results in a very compact reading circuit. Reference [78] discusses the use of a capacitance-based sensor to detect DNA hybridization. Reference [71] describes reconfigurable pixel architecture, capable of performing cyclic voltammetry, potentiometry and impedance spectroscopy.

The goal of this chapter is to demonstrate how we can implement a fully-integrated impedance-based CMOS biosensor system. The transduction method used in this system, i.e., electrochemical impedance spectroscopy (EIS), is widely used to detect a wide variety of biomolecules such as DNA and proteins ([7],[21]).

In EIS, small impedance changes in an electrode-electrolyte interface that are generated by capturing events are detected in real-time and are correlated to the presence, as well as, the abundance of various analytes. EIS is a label-free and a real-time detection method. However, the challenge is to measure the small impedance change due to capturing in the presence of a large electrochemical background. Furthermore, impedance measurement is an

inherently complex process that requires complicated data analysis to meaningfully interpret the data. Our challenge in this research is to leverage the capabilities of VLSI systems to not only design high-dynamic range impedance detectors for biosensing, but also integrate an array of them in a single CMOS chip. Finally, we want to design this system as an open-platform by making its electrode transducers compatible with conventional EIS methods.

Initially in Section 2 of this chapter, we introduce the system-level issues in EIS biosensors, the electro-analytical transducer design, and the proposed impedance detection methodology. In Section 3, we discuss in detail the IC implementation of various blocks in a standard CMOS process, followed by an explanation of both the electrical and biological experimental results obtained in Section 4.

5.2 EIS Biosensor System

5.2.1 EIS Electrode Design

The sensing electrode needs to take advantage of a variety of capturing molecules for detection. These molecules come in a variety of sizes, molecular weights, and charge densities. For example, a short 30 base pair (bp) oligonucleotide in DNA-based biosensors can weigh about 9.9 kDa, while an immunoglobin A (IgA) antibody used in EIS immunoassays weighs more than 70 kDa [80]. These molecules can also exhibit different levels of hydrophobicity and hydrophilicity and hence interact differently with the molecules on the electrode surface. As a result, it is critical to consider the physiochemical

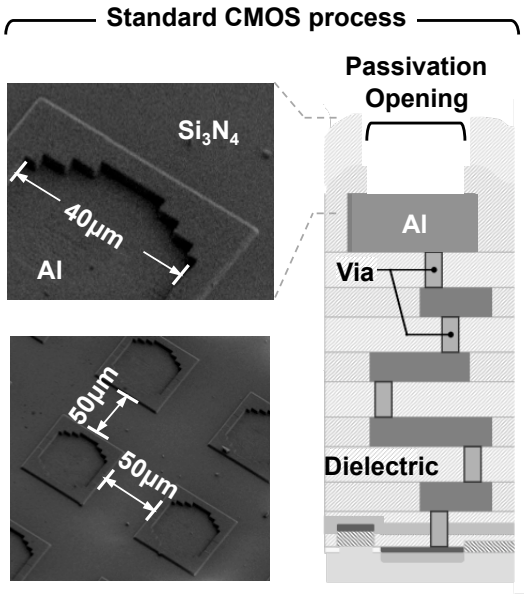

Figure 5.2: Passivation openings in standard CMOS structure used as sensing electrodes.

characteristics of the probes in EIS systems. Additionally, it is imperative to choose a proper material for the conducting electrode (e.g., Au or Pt) and the proper linking molecule or chemical bond between solid electrode surface and the capturing probe.

In our system, we choose gold (Au) as the material of choice for our electrode surfaces (Section 3.6.1). The main rationale for this is its inertness (i.e., Au does not corrode with non-zero biases on the surface), in addition to being biocompatible. One can implement different thiol-based immobilization chemistries to attach molecules to the Au surface ([39],[43],[81]).

The electrodes in our design are created by first forming passivation openings on the top metal layer of the CMOS process, as it is done for I/O

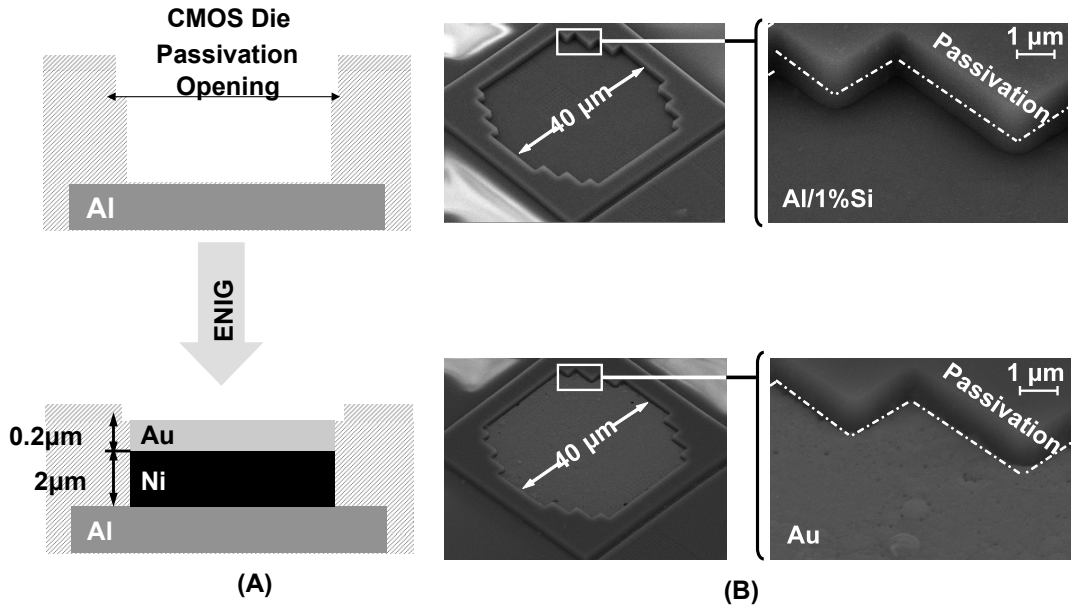

Figure 5.3: (A) Top layers of a CMOS process, where using an electroless nickel immersion gold (ENIG) process we create Au sensing electrodes, and (B) SEM picture of surface before and after the ENIG process.

pads (illustrated in figure 5.2). The exposed electrodes are approximately $40\mu m \times 40\mu m$ in size and are separated by a distance of $50\mu m$. To create an universal Au electrode surface, we took advantage of an electroless nickel (Ni) immersion Au (ENIG) plating process [82] to first form a Ni layer and then a Au layer on the exposed Al electrode surfaces (see figure 5.3). The reason for forming the Ni layer first is that Au can not be directly plated on Al surfaces and an intermediate layer is necessary. This method does not require the use of masks since Ni and Au do not attach to the passivation layer. The thicknesses of the Ni and Au layers are approximately $2\mu m$ and $200nm$, respectively. The Au surface can be bio-functionalized using thiol-based protocols where the sulfur in the thiol group can form a covalent bond to the Au surface and act as the anchor for the linker molecule. This can be used for immobilization of various biomolecules such as DNA and proteins (Section 3.6.2).

5.2.2 Impedance Detection

The goal of the detection circuitry in EIS systems is to measure, in real-time, the admittance of the electrode-electrolyte interface, denoted by $Y(\omega)$. In an array format, we need to measure the admittances of all pixels in parallel and independently. To do this in our biosensor system, we place a large and shared reference electrode in the solution to establish the sinusoidal excitation voltage signal, $V_X(\omega)$, across all electrodes. Next, we measure individually the current flowing through each electrode, $I(\omega)$ and compute the electrode-

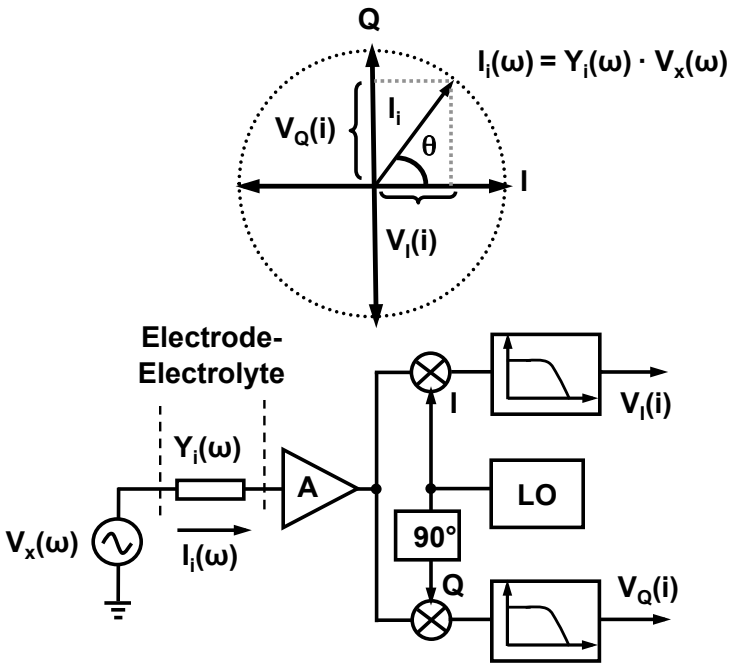

Figure 5.4: Coherent detection architecture for impedance measurement.

electrolyte admittance of the i^{th} pixel, $Y_i(\omega)$, using the formula

$$Y_i(\omega) = \frac{I_i(\omega)}{V_x(\omega)} \tag{5.1}$$

where $I_i(\omega)$ is the measured current at the i^{th} pixel. Since all signals in this system are sinusoidal, to find $Y_i(\omega)$, we only need to calculate the relative amplitude and phase shift of $I_i(\omega)$ compared to $V_x(\omega)$. In this chip, we take advantage of the coherent detection method (also known as the direct conversion method) to obtain the phase and amplitude information of $I_i(\omega)$ simultaneously. The approach is to first amplify the current $I_i(\omega)$ in each pixel by means of a low-noise transimpedance amplifier (TIA) with gain of A, as shown in figure 5.4. The output of TIA is then multiplied by orthogonal

sinusoidal signals (I and Q) at the frequency ω (the same frequency as the excitation source). Subsequently, the higher-order harmonics are removed using a low-pass filter. The DC value at output of the I and Q channels of the i^{th} pixel, denoted by $V_I(i)$ and $V_Q(i)$ respectively, are then used to estimate the amplitude and phase of $Y_i(\omega)$ using the formula

$$|Y_i(\omega)| = \frac{\sqrt{V_I^2(i) + V_Q^2(i)}}{A|V_x(\omega)|}, \tag{5.2}$$

and

$$\angle Y_i(\omega) = tan^{-1}\left(\frac{V_Q(i)}{V_I(i)}\right). \tag{5.3}$$

5.2.3 System Architecture

The overall chip architecture is shown in figure 5.5. The system consists of an array of 10×10 pixels where column and row decoders are used to scan the array and access the individual outputs of pixels sequentially. This approach is similar to the readout structure of CMOS image sensors [83]. Each pixel within the array consists of a sensing electrode and a coherent detector readout circuitry, which include the low-noise TIA for current amplification and two mixers I and Q for multiplication. The reference electrode, which establishes $V_x(\omega)$ within the electrolyte is an external component (i.e.., not integrated), and as discussed before, is immersed into the electrolyte solution. It is important to realize that the capturing probe of each pixel can be different and hence this particular system can be used to detect up to 100 different analytes.

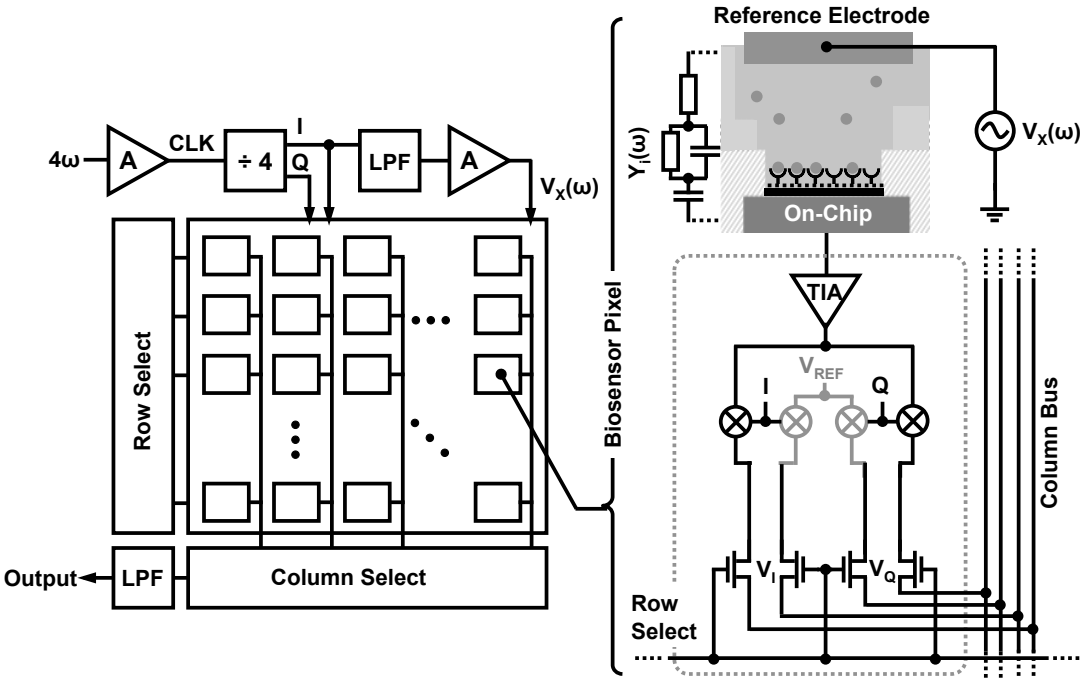

Figure 5.5: System architecture.

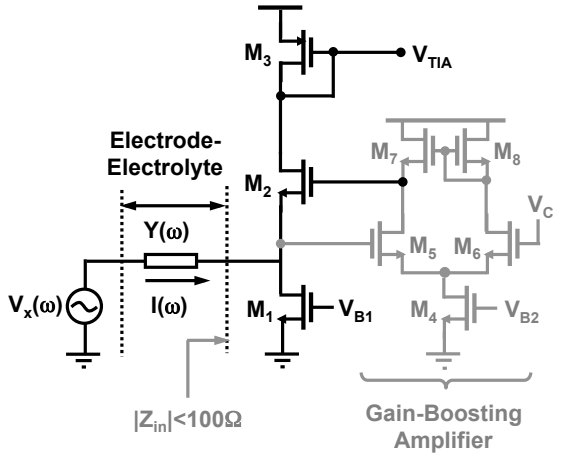

Figure 5.6: Circuit diagram of Transimpedance amplifier (TIA).

The quadrature (90° phase shifted) I and Q signals as well as $V_x(\omega)$ are generated within the system using an external reference clock operating at 4ω. The 4ω clock first goes through a divide-by-4 digital counter to generate the necessary quadrature I and Q square-wave signals at ω. The excitation signal $V_x(\omega)$ is derived from the I signal (using a low pass filter and an amplifier) and therefore is phase-locked to it. The main advantage of this approach is that by sweeping the clock, we can sweep ω and measure $Y(\omega)$ without modifying the readout circuit which operates independent of $V_x(\omega)$, at a much lower frequency. Yet, we still need to guarantee that the TIA and mixers function properly in the desired frequency range.

5.3 IC Implementation

5.3.1 Transimpedance Amplifier(TIA)

The main objective of the low-noise TIA, besides amplification, is to keep a low impedance node at the sensing electrode contact. This is to ensure that $Y(\omega)$ remains proportional to $I(\omega)$ only, and does not become a function of the TIA impedance. As illustrated in figure 5.6, we chose a common-gate topology for the TIA using transistors M_1-M_3. To decrease the input impedance of the TIA, we additionally gain-boost M_2 by using a differential amplifier made of transistors M_4-M_8. If we consider the gain of this differential amplifier to be $A_d = -g_{m5}\left(r_{o5}||r_{o7}\right)$, then, Z_{in}, the input impedance of the gain-boosted TIA becomes

$$Z_{in} = \frac{1}{g_{m2}A_d} = \frac{1}{g_{m2}g_{m5}\left(r_{o5}||r_{o7}\right)} \tag{5.4}$$

The TIA is designed such $|Z_{in}|$ always remains below 100Ω for frequencies up to 50MHz. This ensures that for a typical electrode-electrolyte interface impedance values (typically, $|Y(\omega)| > 10k\Omega$), the error remains below 1 %. The TIA gain, A_{TIA}, in this particular topology is equal to $g_{m3}^{-1} \approx 13k\Omega$, which is approximately equal to the input impedance of the diode connected M_3.

The role of the differential amplifier is to not only reduce $|Z_{in}|$, but also set the DC potential of the sensing electrode. This DC potential is set by applying an external voltage, V_c, to the positive input of the differential amplifier. The error voltage is a function of the loop gain and approximately

equal to 5mV for A_d=45dB, which is the nominal DC gain of the differential amplifier. This feature is particularly beneficial in controlling Faradaic processes (i.e., oxidation and reduction) that may occur due to the potential difference between the reference and sensing electrodes. The value of V_c in our system can vary between 0.9V to 2V without affecting the functionality of the TIA, making it possible to measure admittance while applying DC voltage stimulations on the sensing electrode.

One key consideration in the design of TIA is its noise performance. The leading noise contributors are the current source M_1 and the load transistor M_3. In the common-gate structure, M_2 acts as a cascode transistor and hence has little effect on the overall noise performance. The noise from the differential amplifier is also negligible since its output voltage noise has an contribution of $g_{m2}\left(1+g_{m2}r_{o1}\right)^{-1}$ to the TIA input current. Hence, the input-referred current noise power spectral density (PSD) of the TIA, denoted by $\overline{I_n^2(\omega)}$, can be formulated by

$$\overline{I_n^2(\omega)} = 4kT\left(\gamma_1 g_{do1} + \gamma_3 g_{do3}\right) \tag{5.5}$$

where g_{do} is the zero-bias drain source transconductance, and γ is a bias dependant noise coefficient of the associated transistors.

In equation 5.5, strictly speaking, one should also include the 1/f noise contributions of M_1 and M_3; yet we have neglected them and only included their thermal noise component. This is because the lock-in amplifier acts as an narrow-band coherent receiver architecture in the signal chain. In such

systems, similar to most RF receivers, as long as ω remains significantly above the 1/f noise corner frequency, the noise becomes out-of-band and thus not present at the output. The 1/f noise corner frequency in our system is designed to be 50 kHz which is achieved mainly by increasing the lengths of M_1 and M_3 to $5\mu m$ and $1\mu m$, respectively.

The current through the common gate stage in this design is $50\mu A$. Although this current can be lowered without significantly reducing the gain and worsening the noise performance of the TIA, we intentionally kept it high to be able to measure $|I(\omega)|$ in the order of 10-20μA with sufficient linearity. Since $|Y(\omega)|$ can be as low as $10k\Omega$, $|I(\omega)|$ can be as high as $20\mu A$, for an excitation voltage of 20mV. The differential amplifier bias current is also set to $50\mu A$. This is to achieve the sufficient gain-bandwidth product, i.e., minimum gain of 30 dB at 50 MHz, and ensure $|Z_{in}| < 100\Omega$.

5.3.2 Quadrature Mixers

To multiply $I(\omega)$ by the I and Q quadrature clocks, we connect the diode-connected output of the TIA, V_{TIA}, to the input of two double-balanced differential Gilbert cell mixers, as shown in figure 5.7. For the sake of clarity, only one of the two identical mixers is shown in the figure. Differential Gilbert cell mixers [84] are widely used as they greatly reduce the LO leakage to the outputs and relax the filtering requirements at the output. Also, having differential outputs is beneficial for sensor arrays as they are less prone to interference, IR drops, and other non-idealities present in the array. In the

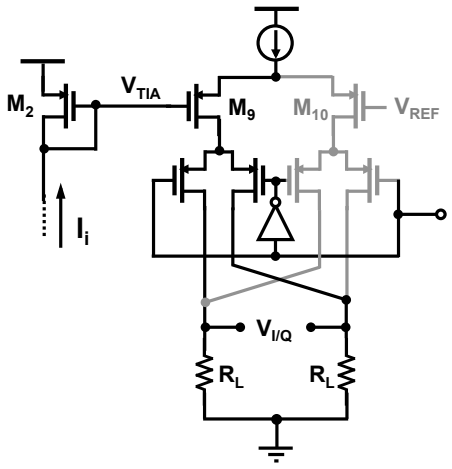

Figure 5.7: Circuit diagram of mixer.

mixers, the transconductance of M_9-M_{10}, g_{m9}, in the input differential pair is set to be equal to g_{m3}. To minimize the 1/f noise contributions of the mixers, we also use resistors ($\approx 50k\Omega$) instead of placing active transistor loads. Based on this configuration, the total transimpedance gain of system, A_{Total}, becomes

$$A_{Total} = \frac{2}{\pi} A_{TIA} \left(-g_{m9} R_L\right) = -\frac{2}{\pi} R_L \tag{5.6}$$

Since the output of the TIA (positive input of the differential mixer) is single ended, we have to generate a stable DC reference voltage V_{REF} for the other input (negative input of the differential mixer). As shown in figure 5.8, this is done by placing a replica circuit with an identical structure as the low-noise TIA. There is only one difference between the TIA structure and the replica circuit. In the replica circuit, the bias used for the differential amplifier is only $5\mu A$ instead of $50\mu A$ since it only needs to operate at DC and hence has a relaxed gain-bandwidth requirement. The overall current consumption of the

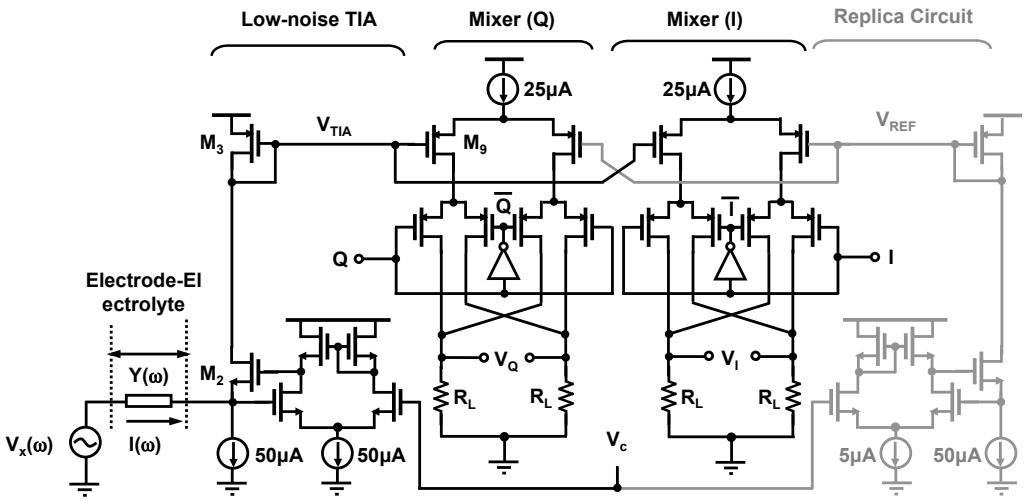

Figure 5.8: Circuit diagram of the entire pixel (excluding bias circuits).

pixel is $220\mu A$ (including the bias circuits in each pixel) with a 3.3.V supply with a total area of $100\mu m \times 100\mu m$.

It is important to realize that the large size of the biosensor array results in inevitable pixel-to-pixel gain and dc offset variations. This phenomenon is somewhat comparable to the fixed pattern noise (FPN) in CMOS image sensor arrays [83]. In our case, offset and gain variations are primarily caused by the mismatch between the load resistors of the mixers. Accordingly, we paid careful attention to the layout and physical dimensions of these devices to ensure acceptable non-idealities.

5.3.3 I and Q Generation

The chip has a built-in divide-by-4 generator which accepts a 4ω reference clock and generates the necessary I and Q clocks required for the oper-

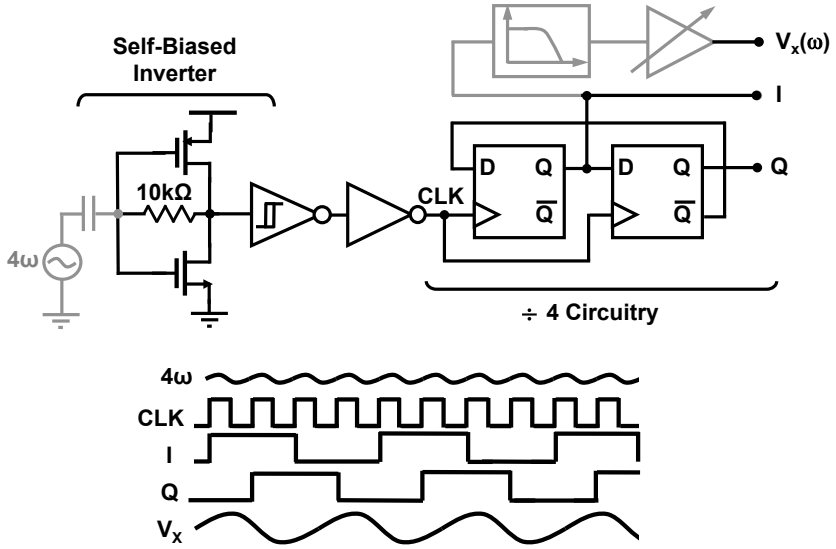

Figure 5.9: I/Q Generator (grey blocks are off-chip components).

ation of the mixers. As illustrated in figure 5.9, we use a self-biased inverter to recover the AC-coupled clock signal. The self-biased inverter reduces the sensitivity of the circuit to the amplitude and DC bias point of the input sinusoid. It also sets the DC bias point at the threshold voltage of the inverter (approximately to 1.65V in our design) with a small-signal gain of 3.5. The main disadvantage of self-biased inverters is their sensitivity to glitches in the power supply. In order to eliminate this impediment, a Schmitt trigger buffer [85] is used after the self-bias inverter. This buffer creates a voltage window of approximately 1V around the transition region, making the output insensitive to any input glitch within this window. The output of the Schmitt trigger is then buffered and applied as the clock input (CLK) of the two flip flops that serve as the divide-by-4 circuitry. The rationale behind using this topology is

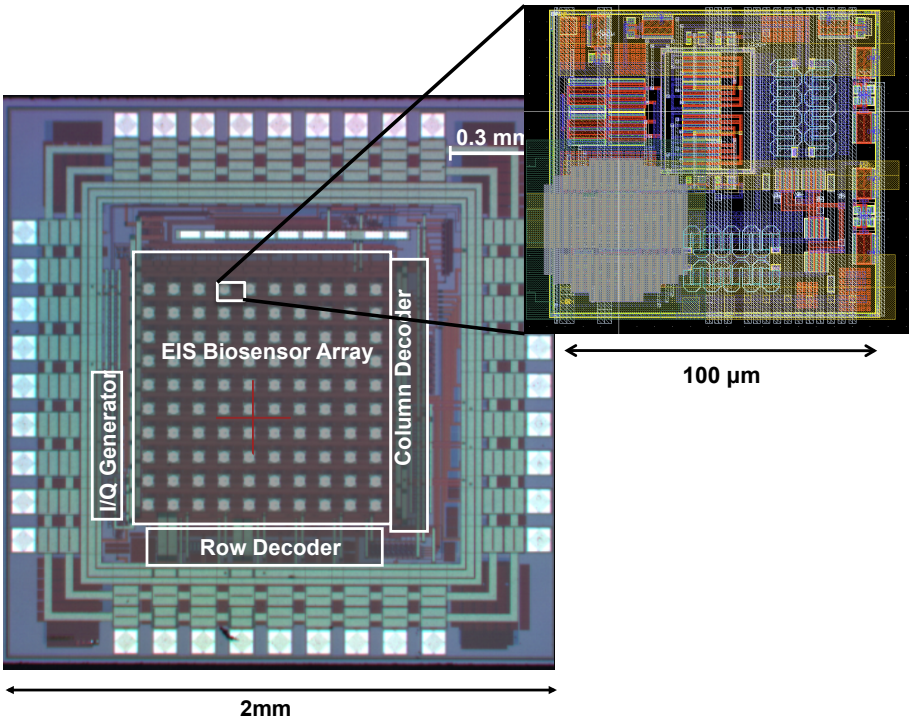

Figure 5.10: Die photograph.

that we can reliably generate accurate I and Q for a wide range of frequencies. Our measurements demonstrated that the achieved phase error is less than 0.2 degrees over the entire 10Hz to 50MHz frequency range. The I signal is subsequently taken off-chip, low-pass filtered, and passed through a variable gain amplifier to create $V_x(w)$. The typical amplitude for $V_x(w)$ in this system is between 10-20mV.

In figure 5.10, we show the chip micrograph of the biosensor IC which is designed and fabricated using a $0.35\mu m$ bulk CMOS process. The total chip size is $2mm \times 2mm$, with the 10×10 array occupying $1mm \times 1mm$ of this

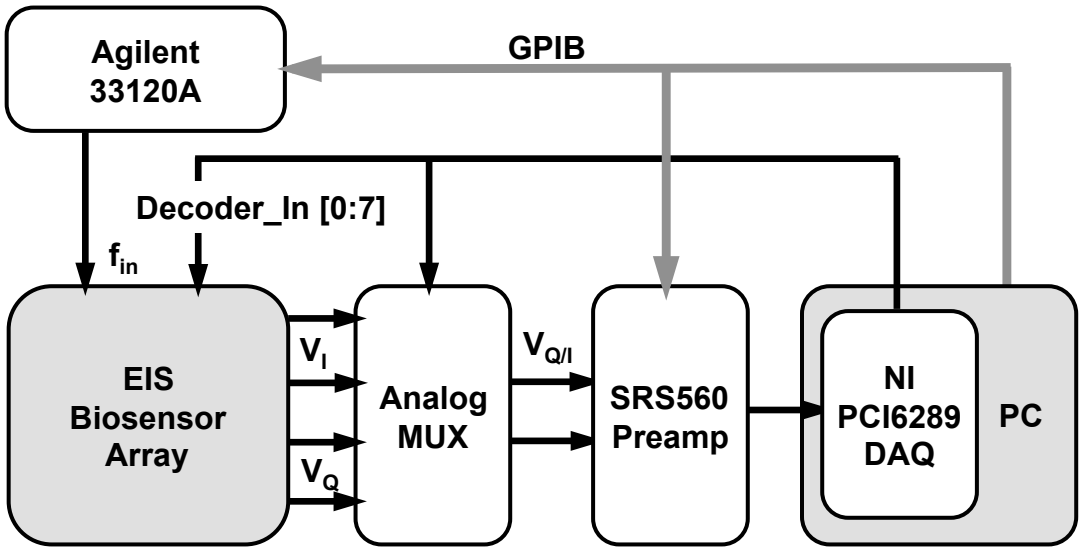

Figure 5.11: Measurement setup.

area. The layout of one of the identical pixels is also shown in the figure. The pixels are $100\mu m \times 100\mu m$ in size.

5.4 Results and Discussion

The IC measurement setup is shown in figure 5.11. The inputs to the EIS biosensor chip are the external reference clock operating at 4ω (from Agilent 33120A) and the digital inputs to the decoder (from NI PCI 6289). There are two differential outputs in this system, i.e., V_I and V_Q, which are first multiplexed, amplified, and filtered using a low noise preamplifier (SRS560) and later digitized using the NI PCI 6289 acquisition system. The whole setup is computer controlled by means of a GPIB bus, which also synchronizes the excitation and data collection components of the test system. Before

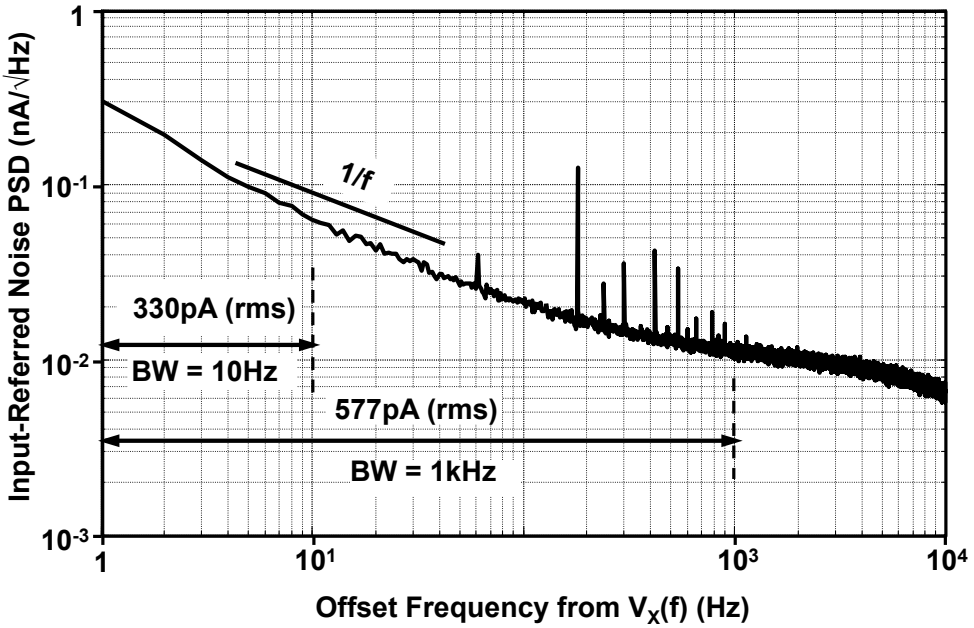

Figure 5.12: Pixel-level Input referred current noise PSD.

calculating the admittance using the equations 5.2 and 5.3, we subtract the DC offset of each pixel which is measured prior to experiments, under input open-circuit conditions. Using this setup and dc offset calibration procedure; we are able to perform automated admittance measurements accurately at a large number of frequency points over the entire array.

5.4.1 Admittance Detection Limits

In order to calculate the impedance sensitivity (i.e., minimum detection level) of the system, we need to measure the noise performance of the pixels. The noise at the output, prior to low pass filtering, is measured under input open circuit conditions with an excitation frequency of 2.5MHz. Shown in

figure 5.12, is the input-referred current noise PSD, which is essentially the output noise divided by A_{Total}.

Now, to evaluate the current sensitivity of this system, we need to integrate the current noise PSD over a specific bandwidth to find its noise rms value. As one can see in figure 5.12, this value is 330pA rms and 577 pA rms for 10Hz and 1kHz bandwidths, respectively. While lowering the cut-off frequency of the low pass filter, f_c, results in a better noise performance, it reduces the overall measurement speed and array scan rate. Considering that the required settling time for 16-bit accuracy is approximately $11f_c$, we need about 110s to perform one full scan of all the 100 pixels for f_c= 10Hz, while for f_c=1kHz, this value is 1.1s. Such level of sensitivity is sufficient for most EIS systems since any further improvement is limited by the thermal noise contribution of the electrolyte resistance [4].

The upper limit of impedance detection is set by the linearity of the signal-chain. The linearity is measured here by placing a $10k\Omega$ resistor at the input of the TIA and we vary the amplitude of $V_x(\omega)$. The output amplitude, $|V_0|$, is then calculated using the measured values of V_I and V_Q such that

$$|V_0| = \sqrt{V_I^2 + V_Q^2} \tag{5.7}$$

Figure 5.13 shows the measured $|V_0|$ as function of $|V_x(\omega)|$. For currents smaller than $20\mu A$, the response is linear with a constant slope equal to $|A_{Total}|$=86dBV/A. As the current increases, the circuit enters a non-linear region. The 1dB compression point is approximately $40\mu A$. One inherent dis-

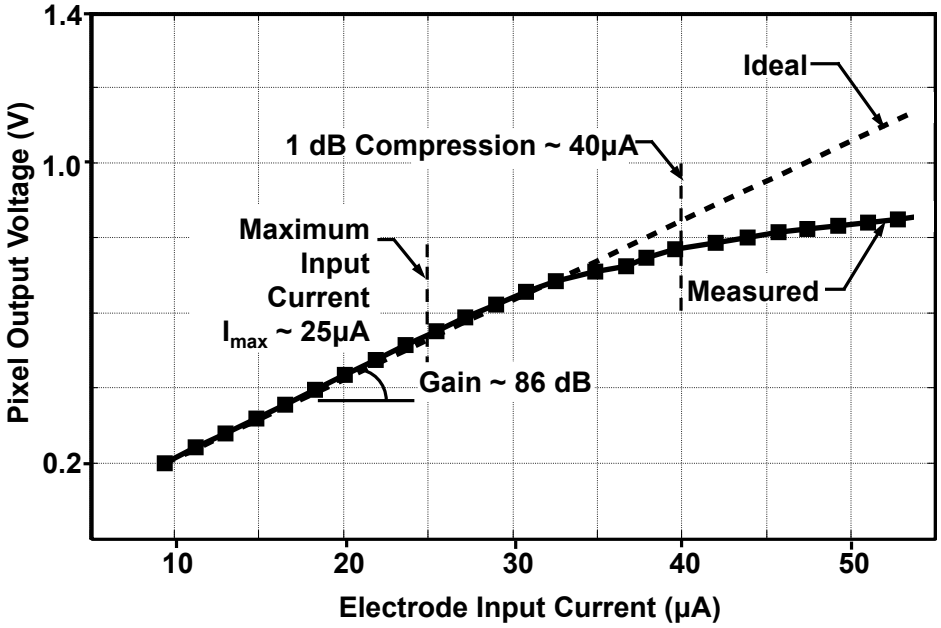

Figure 5.13: Linearity performance of the pixel.

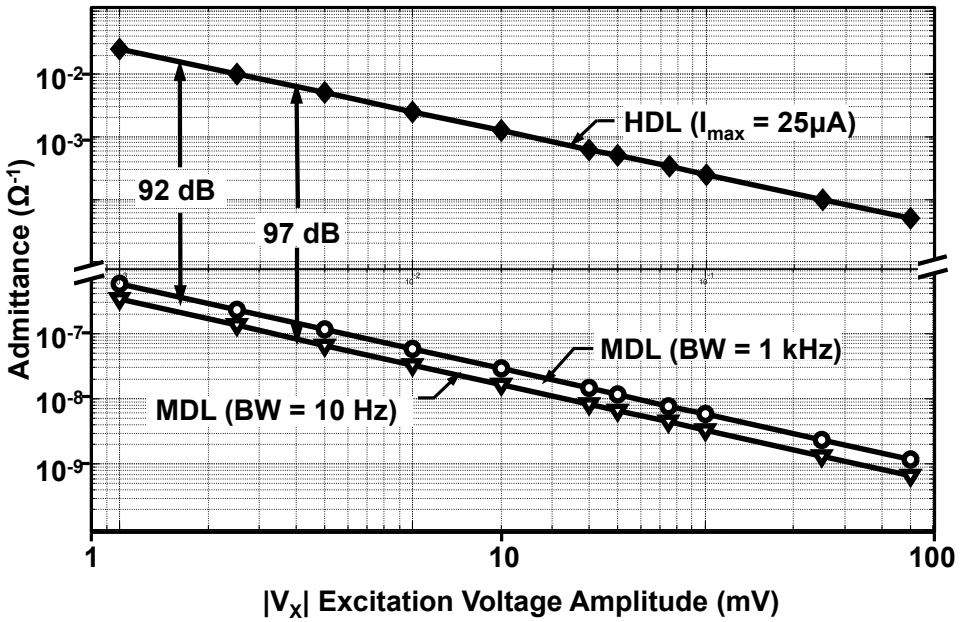

Figure 5.14: Admittance minimum detection level (MDL) and highest detection level (HDL).

advantage of using coherent receivers is that the DC output generated by the second order non-linearities directly affects the measured V_I and V_Q, which are also at DC. Accordingly, we chose a safe upper limit of detection, I_{max}, to be $25\mu A$, backing off sufficiently from the 1dB compression point.

Now we can calculate the admittance minimum detection level (MDL) and highest detection level (HDL). As plotted in figure 5.14, for $|V_x(\omega)|$=10 mV, this system is capable of measuring $\Delta|Y(\omega)|$ of 10nS for $|Y(\omega)|$ as high as 1mS. This is approximately 97dB detection dynamic range (DDR), which is maintained over a wide range of excitation frequencies from 10Hz to 50MHz. To the best of our knowledge, this is the highest reported DDR ever for an

Table 5.2: Chip's key metrics

Technology	$0.35\mu m$ CMOS, 4 metal layers, 3.3V supply
Die size	$2mm \times 2mm$
Array size	$10 \times 10, 100\mu m \times 100\mu m$
Electrode	$40\mu m \times 40\mu m$, Al/1 % Si
Frequency range	10Hz - 50MHz
Power consumption	84.8mW (100kHz)
Current sensitivity (BW=10Hz)	330pA
1 dB compression point	$40\mu A$
Dynamic Range(BW = 10Hz)	97dB
Scan rate (BW=10Hz)	$0.55min^{-1}$

admittance measurement system. The overall chip performance and its key metrics are listed in table 5.2.

5.4.2 Electrochemical Measurements

For performing EIS experiments, we need to bring the sensing electrode array in contact with the solution (electrolyte). To do this without interfering with the electronic data acquisition, we isolate the conductive solution from the bond-wires, I/O pads, and the IC package by using an electrically insulating epoxy (Epotek H70S), as shown in figure 5.15. Subsequently, the reference 1mm diameter Au wire electrode is immersed into the solution carefully on top of the sensing surface.

Shown in figure 5.16, are our real-time example impedance measurements performed with KCl buffer, in which the salt concentration is changed twice during the experiment. Initially $120\mu l$ of 1mM KCl is present into which

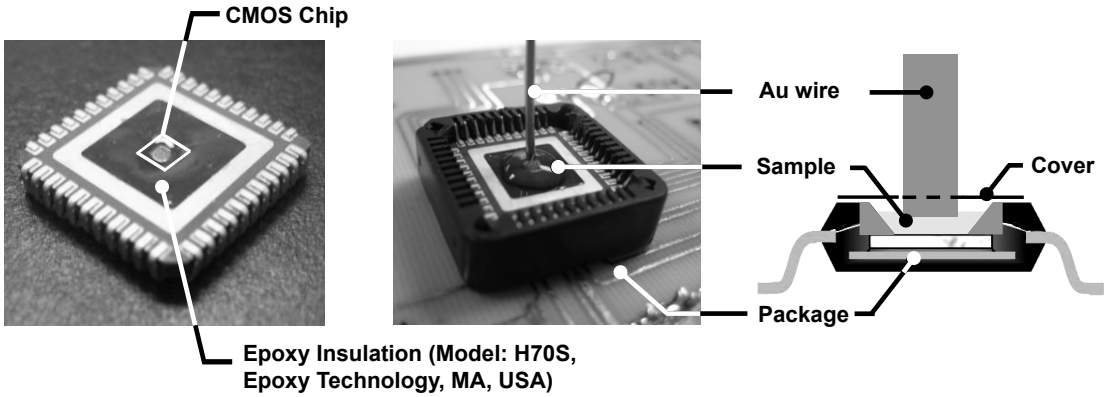

Figure 5.15: Packaging and electrochemical experimental setup.

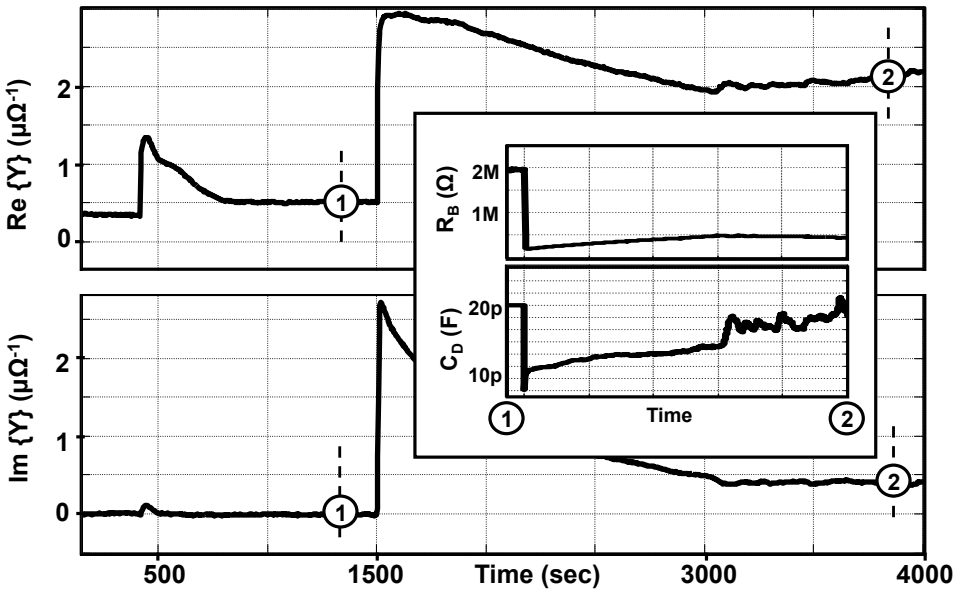

Figure 5.16: Real time control experiments.

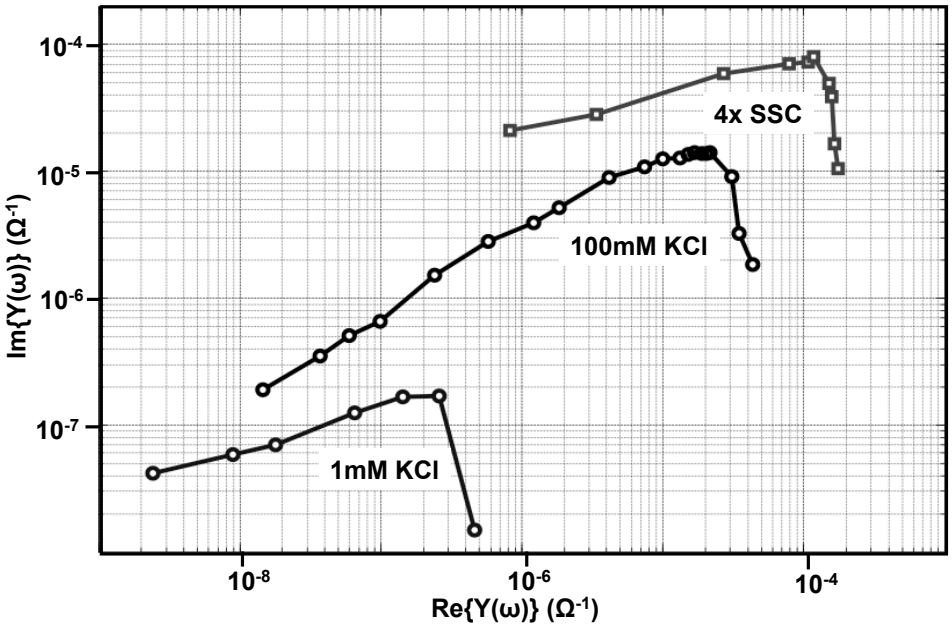

Figure 5.17: Admittance spectra of three different buffers.

$6\mu l$ of 10 mM and then $6\mu l$ of 100 mM KCl are added. The measurements results shown here are done at ω=100 kHz and data points are collected with a rate of $1ksamplesec^{-1}$. In this example, we can clearly see the exponential settling of the admittance values which shows the relaxation of the interface charge distribution. R_B decreases, as we increase the ionic strength of the solution. The surface capacitance increases due to the increase in ionic strength, as explained in an earlier chapter. The real-time detection capability provided by our CMOS EIS sensor is significant, since only a few commercially available platforms offer this feature.

Though real-time measurements enable kinetic analysis, conventional EIS methods still measure the admittance values at equilibrium. To demonstrate the versatility of the our system at measuring impedance at equilibrium, we first measured the admittance spectra of some of the common biological buffers used in DNA and protein detection assays. The admittance spectra are measured with zero DC potential difference between the reference electrode and the sensing electrode. In the Nyquist plots shown in figure 5.17, the imaginary part of $Y(\omega)$ is plotted as a function of the real part. As evident from the figure, the admittance values of different buffers can vary by five orders of magnitude, which is consistent with their ionic strength and conductivity. This admittance data is fitted into equivalent circuit model by utilizing a complex non-linear least square-fitting tool [86]. The equivalent circuit parameters are shown in Table 5.3. This specific set of measurements verifies the DDR our biosensor system can achieve and proves that it can operate both in low

Table 5.3: Equivalent circuit parameters for biological buffers

Buffer	C_{DL}	R_{CT}	R_B
1mM KCl	9.75pF	$10^{12}\Omega$	$3.3M\Omega$
100mM KCl	13.22pF	$270k\Omega$	$36.8k\Omega$
4x SSC	327.5pF	$72k\Omega$	$9.3k\Omega$

Table 5.4: Equivalent circuit parameters for DNA hybridization experiment

Buffer	C_{DL}	R_{CT}	R_B
ss-DNA	190.9pF	$1.2 \times 10^{10}\Omega$	$9.36k\Omega$
ds-DNA	175.1pF	$10^{10}\Omega$	$9.36k\Omega$

conductance as well as high-conductance regimes.

5.4.3 Biological Measurements

Detecting DNA hybridization is key to all nucleic acid-based biosensors such as gene expression DNA microarrays. One of the advantages of EIS based biosensor is that it permits label-free detection of DNA hybridization. To show this capability here, we immobilized thiolated ssDNA molecules directly onto the Au electrode surface as the capturing probe. The probe sequence in this

Table 5.5: Equivalent circuit parameters for protein detection experiment

Buffer	C_{DL}	R_{CT}	R_B
11-MUA	31.7pF	$149k\Omega$	$422k\Omega$
11-MUA + Protein-G	51.8pF	$177k\Omega$	$422k\Omega$

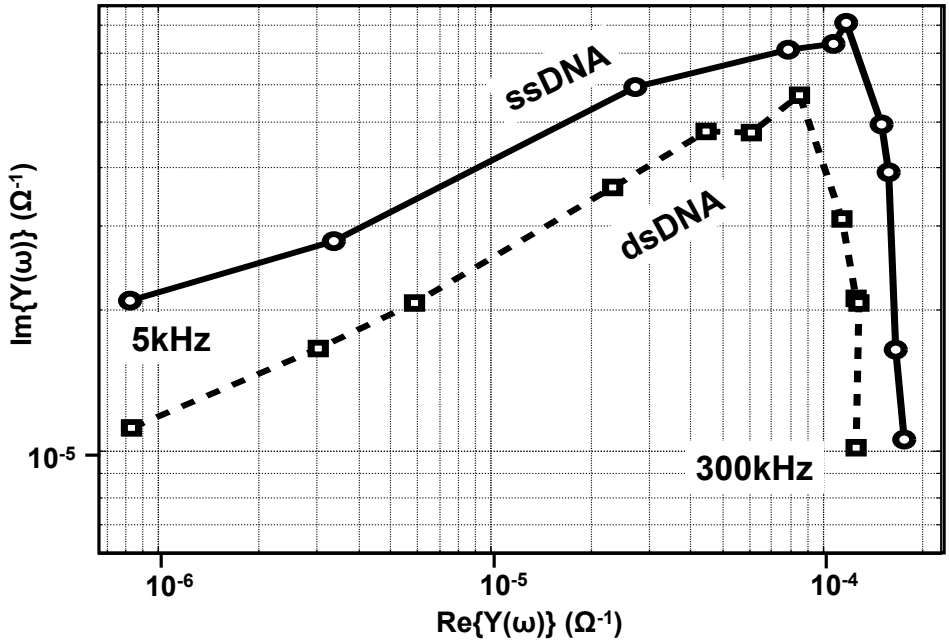

Figure 5.18: DNA hybridization admittance spectra.

particular experiment is 5'-TGATAGCCCTGTACAATGCTGCTAAAAAAA-Thiol-3'. The approximate probe concentration is 7×10^6 per electrode [87]. The admittance spectrum with immobilized probes is measured in 40 μl of $4 \times SSC$ buffer (solid line in figure 5.18). Onto the same buffer, we add $5\mu l$ of $1\frac{ng}{\mu l}$ of complementary ssDNA strand and the admittance spectra of the system is again measured at equilibrium (dashed curve in figure 5.18). This concentration is sufficient to saturate the entire electrode surface. On equivalent circuit fitting (shown in table 5.4), we observed that while R_{CT} and R_B almost remain the same, the value of C_{DL} drops from 190pF to 175pF. This 8% drop in capacitance is due to the lowering of dielectric permittivity near the surface [88]. By linear extrapolation of this result and by making use

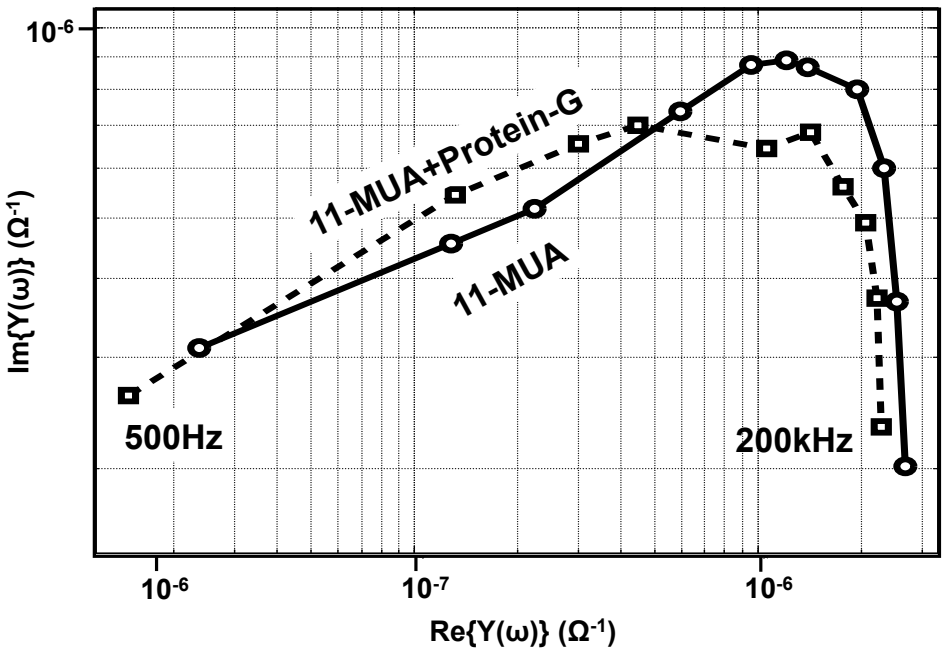

Figure 5.19: Protein G detection spectra.

of the admittance detection limits derived previously, the limit of detection for our system is around 10^5 molecules. This level of sensitivity makes our EIS system comparable to other label-free methods of detection that have been reported [23].

Label-free protein detection has always remained a challenge since it is difficult to label protein molecules without generally altering their properties [89]. EIS method is perhaps the ideal candidate as it can perform label-free detection and can probe into varying depths from the electrode surface, providing us with a vast amount of information. In this research, we performed the detection of protein-G molecules which is a immunoglobulin-binding protein that can attach to a wide variety of antibodies. The protocol for immobilization and detection is taken from [90]. A layer of 11-MUA molecules is immobilized on gold surface and the admittance spectrum is measured in 1x PBS buffer. Then, protein-G is immobilized onto the 11-MUA layer and once again the admittance spectrum is measured in 1x PBS buffer. As plotted in figure 5.19, the admittance spectrum exhibits more complex variation, when compared with DNA hybridization experiment. On equivalent circuit fitting (shown in table 5.5), we observed changes in R_{CT} as well as C_{DL}. As expected, no change was observed in the bulk resistance. The complicated change in admittance is attributed to the fact that proteins are large molecules with complex charge distribution. This is one of the first ever-reported admittance spectra for on-chip detection of protein attachment. Further studies need to be performed to better understand the changes in the admittance spectra. Nevertheless, EIS

provides us with tool for observing the changes that happen near the surface with the attachment of proteins and can be used to perform label-free protein detection.

5.5 Custom ADC design

The EIS chip, described above, still requires an external excitation signal source and external data acquisition systems. In order to build low-cost, portable EIS platforms, it is critical to develop fully integrated EIS system-on-chip (SoC), with no external components. The various components of the SoC, apart from the sensor, are a high resolution ADC, a DSP core capable of performing signal processing operations and a tunable signal generator. The ADC plays a key role by converting the sensor output into a digital signal, permitting one to perform complex on-chip digital signal processing operations and improving the accuracy and even speed of readout. The design and implementation of the ADC, specifically tailored towards digitizing the EIS sensor outputs is described in this section.

5.5.1 Target Specifications

In order to determine the important parameters in the ADC design, it is essential to have a list of target specifications. The output of the EIS sensor serves as the input for the ADC. The output of the pixel circuitry is at low frequencies, due to the lock-in operation, irrespective of the input excitation frequency. It is safe to assume that the bandwidth of the input signal is below

Table 5.6: ADC target specifications.

SNDR	$> 98dB$
Output frequency	$60Hz$
Sampling frequency	$61.44kHz$
Input signal	$DC(BW < 20Hz)$
Input voltage range	-1.6V to 1.6 V differential for common mode of 0.9V

20Hz, which is at a higher frequency than the capturing kinetics in biosensor systems.

The ADC output rate is set to 60 samples per second, which helps in eliminating 60Hz interference at the input. The maximum detection dynamic range of our sensor is close to 100dB, as explained in the previous section. This translates to a requirement of 16 effective number of bits (ENOB) for the ADC, with a signal-to-noise plus distortion ratio (SNDR) $> 98dB$ [91].

Another important specification for an ADC is its sampling frequency f_s. In oversampling data converters such as the Σ-Δ converter, oversampling ratio (OSR) refers to the ratio between the sampling frequency f_s and output data rate. In order to achieve a 100 dB dynamic range, it is essential to use a higher order Σ-Δ modulator ([91],[92]). The first-order modulator requires an OSR of 4096 to achieve a 100 dB dynamic range, whereas for a second-order Σ-Δ modulator, an OSR of 256 is sufficient. Also higher-order Σ-Δ modulators are less susceptible to issues such as idle tones and dead zones when compared to a first-order architecture ([91],[92]). In our case, we choose a

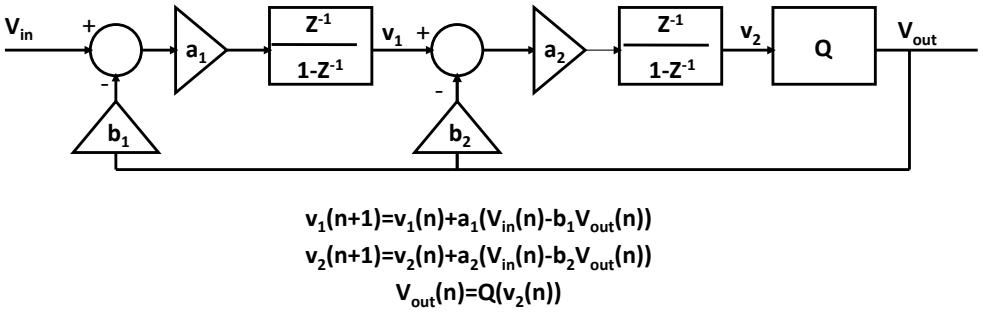

Figure 5.20: A general model of a second-order Σ-Δ converter.

second order Σ-Δ ADC with an OSR of 512, which sets the sampling frequency as $60 \times 512 = 61.44kHz$.

In order to accommodate the large range of DC output voltages generated by the sensor, the ADC must have the capability to work linearly over a wide range of input differential voltages. The differential input voltage range specification is chosen as -1.6V to +1.6V, for a common mode mode of 0.9V. Table 5.6 provides a summary of the key specifications.

5.5.2 System Level Design

A general model of a second-order Σ-Δ converter is shown in figure 5.20[92]. For achieving good linearity, a one-bit quantizer is used. The coefficients a_1, a_2, b_1, and b_2 play an important role in determining the intermediate voltage levels and the overall stability of the Σ-Δ loop.

In order to fix these coefficients, MATLAB simulations are run in which the input is swept over the entire differential voltage range (-1.6V to 1.6V) and

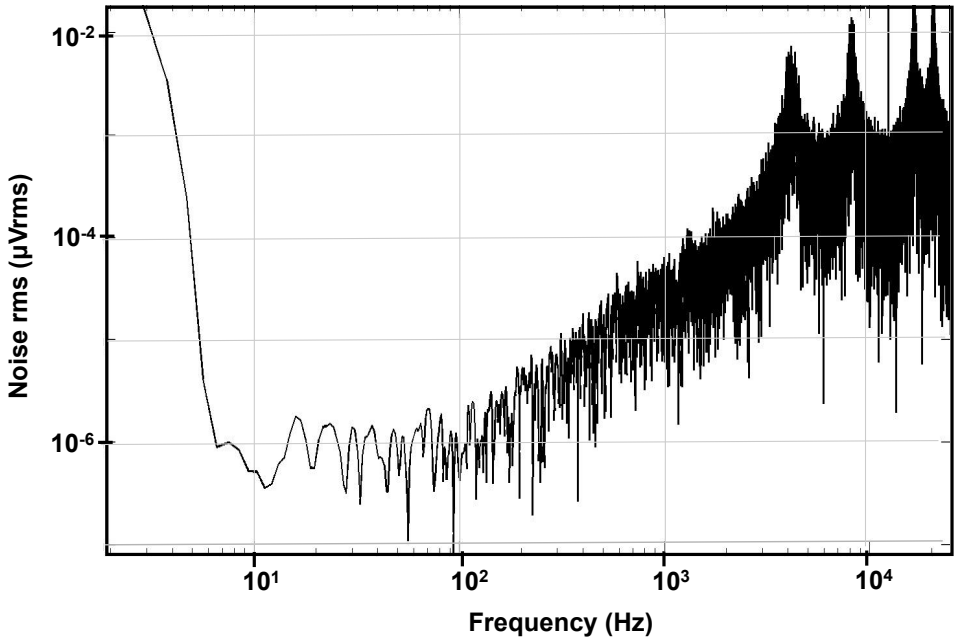

Figure 5.21: Simulated noise PSD of the Σ-Δ converter.

the corresponding intermediate voltage levels are observed. It was observed that for coefficients, $a_1 = 0.16$, $a_2 = 0.5$, $b_1 = 1$, and $b_2 = 0.5$, the intermediate voltage levels remain below 1.8V (which is the supply voltage for the chip) for the entire input differential voltage range.

One of the key advantages of the Σ-Δ converter is that it can perform noise shaping [93]. We performed a system level MATLAB simulation, considering an input referred thermal noise of $64\mu Vrms$. The noise response at the output of the converter is shown in figure 5.21. The integrated noise in 30Hz band is -105dB below full scale, which meets our SNDR requirement.

A decimation filter is used at the output of a Σ-Δ converter in order to reduce the sampling rate and filter out the noise outside the frequency band

of interest. In our system, we made use of a $sinc^3$ filter as a decimation filter, whose transfer function is given by $\left(\frac{1-z^{-OSR}}{1-z^{-1}}\right)^3$. This filter has three sinc filters in series and the filter roll-off is three times faster than a *sinc* filter [91].

5.5.3 Implementation

The Σ-Δ modulator can be implemented using a switched-capacitor circuit as shown in figure 5.22. It consists of two op-amp based integrators, a comparator, which acts as a one bit quantizer and a D flip-flop to hold the comparator output value for the entire clock cycle. V_{ref+} and V_{ref-} are switched between 0 and 1.8V, in order to maximize the input voltage range. V_{cmi} is set to the common mode voltage of the sensor outputs.

In the phase ϕ_1, the inputs are sampled onto the sampling capacitors C_1. In the phase ϕ_2, the stored value is subtracted with a fraction of either $+V_{ref(diff)} = 1.8$ or $-V_{ref(diff)} = -1.8$, depending whether it is a 0 or 1 at the output and the resultant charge is transferred to the integrating capacitors. The latch-based comparator compares the v_2+ and v_2- values during this phase, and determines the digital output state of the Σ-Δ converter for the next cycle.

The switches are sized $\frac{1\mu m}{0.18\mu m}$. This translates to a maximum on-resistance of $4k\Omega$. Since our f_s is only 64kHz, the switches settle to 17 bit accuracy well within one half period. In order to minimize errors due to charge injection, we have made use of differential bottom plate sampling at the input switches of the integrator [94]. C_1 value is chosen to be 500fF and

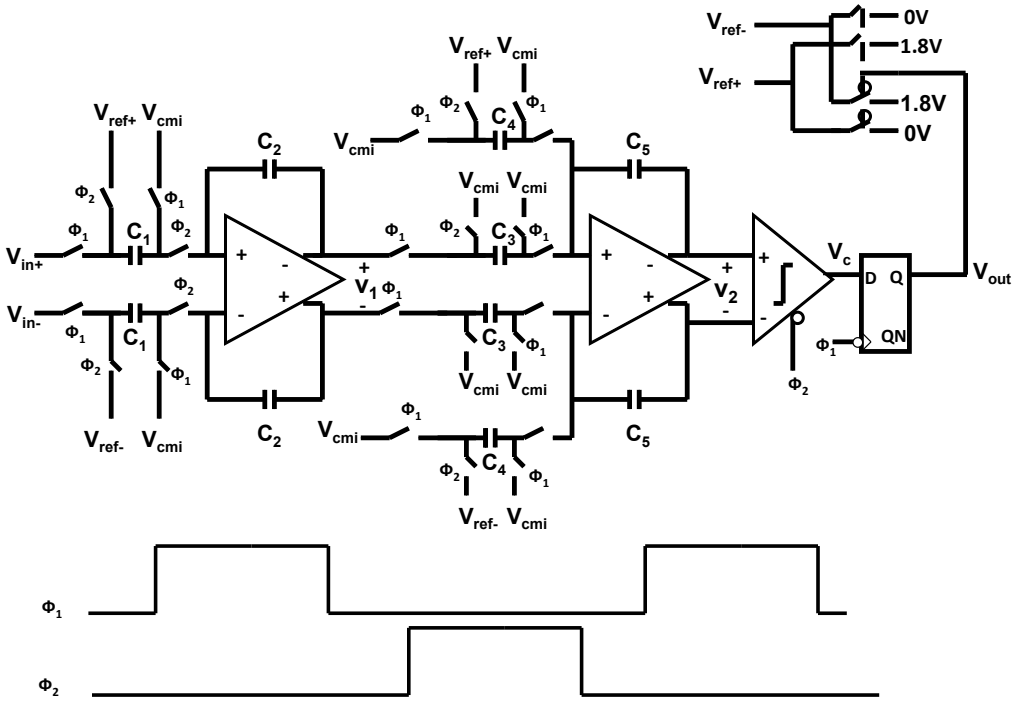

Figure 5.22: Switched capacitor implementation of the Σ-Δ converter.

C_2 is set to $\frac{500}{0.16} = 3.125pF$. These capacitor sizes ensure that the error due to charge injection is less than $25\mu V$(0.5LSB). Furthermore, the $\frac{KT}{C}$ noise at the input is low enough to meet our desired SNDR specification of 98dB. For the second integrator, C_4 is chosen to be 500fF, C_3 is set to $2 \times C_4 = 1pF$ and C_5 is set to $2 \times C_3 = 2pF$, in order to set the desired value for the coefficients a_2 and b_2. The total capacitance used in the circuit is 16.65pF.

5.5.3.1 Op-amp Design

Op-amp design is a critical step in the design of the Σ-Δ converter. Though the gain needs to be only around 54dB (as OSR=512) [91], it is important to make sure that the op-amp has a sufficient gain-bandwidth product, so that all the intermediate voltages settle to the correct value, within the on-duration of ϕ_1 or ϕ_2. The output swing needs to be large, almost rail-to-rail, since any non-linearity introduced by the op-amp due to clipping, can lead to a significant increase in the noise floor [91]. The slew rate should be high enough to support the change in $V_{ref(diff)}$, which can change from -1.8V to 1.8V every cycle. Furthermore, to ensure proper stability and to prevent any ringing, the op-amp should at-least have a phase margin of 60 degrees, and this phase margin condition needs to be met in both ϕ_1 and ϕ_2 conditions.

In order to meet these specifications, a two-stage folded cascode op-amp, with Miller compensation is designed [95]. The folded cascode architecture is chosen, since we need the flexibility to set the input and output common mode voltages independently. In order to obtain a large output swing, a com-

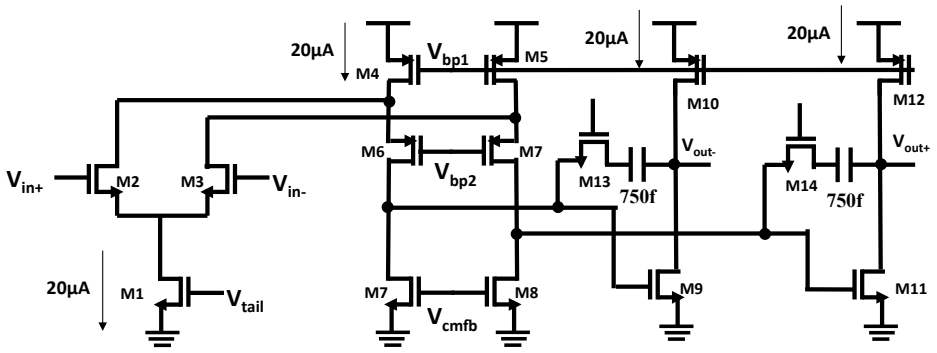

Figure 5.23: Circuit schematic of the op-amp.

mon source amplifier is used as the second-stage amplifier. To accurately define the common mode voltage level at the output, a switched-capacitor common mode feed back circuit (CMFB) is used (not shown) [95]. The total current consumption of the op-amp is $100\mu A$.

5.5.3.2 Comparator Design

A standard latch-based Yukawa comparator is used [96] as shown in the figure 5.24. The comparator outputs are precharged to high during one clock phase. During the other phase, the precharged transistors are disconnected and the outputs begin to discharge. Based on whether V_{INA} or V_{INB} is greater, one of the outputs will fall faster than the other. Due to the negative g_m resulting from the cross-coupled PMOS and NMOS pairs, the exponential rise in one of the outputs causes an exponential drop in the other, pushing the outputs to the opposite rails. The offset of the comparator is around 10 mV. In a Σ-Δ architecture, this offset does not cause any error, as it gets divided by the low

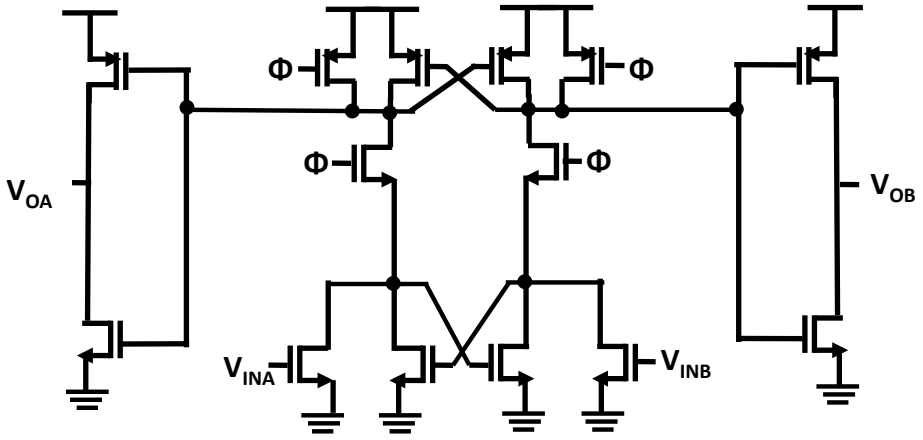

Figure 5.24: Circuit schematic of the comparator.

frequency gain of two integrators, when referred to the input. The settling time is very fast, in the order of a few ns.

5.5.4 Die-level Implementation

The Σ-Δ ADC, along with the decimator and the clock generation circuity are designed and fabricated in $0.18\mu m$ standard CMOS process. The area occupied is $0.5mm^2$. The total power consumption is 0.45mW with a 1.8V power supply. The die photograph of an integrated EIS chip with the EIS sensor and the 16-bit second order Σ-Δ ADC is shown in figure 5.25.

5.6 Conclusion

CMOS integrated biosensors are platforms that can leverage VLSI fabrication technologies to provide cost-efficiency, portability and manufacturability for biosensor platforms. In this chapter, we demonstrated that label-free

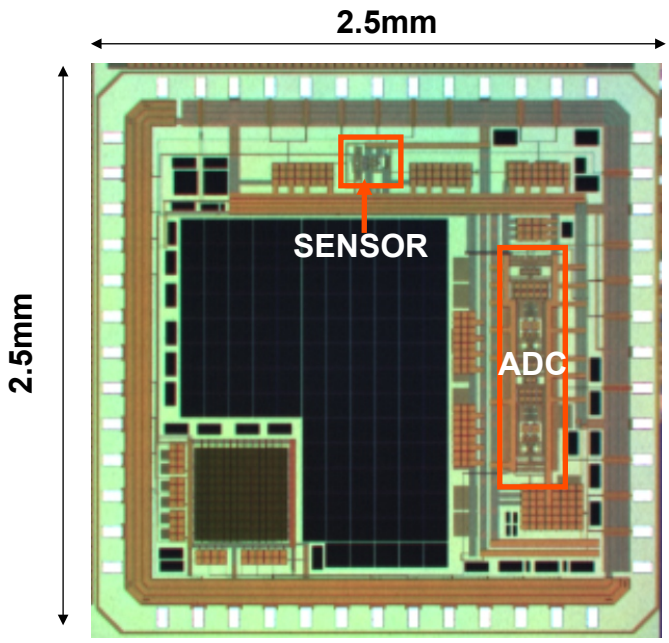

Figure 5.25: Die photograph showing the sensor and the 16-bit Σ-Δ ADC.

and real-time EIS biosensing can be carried out using CMOS ICs, with only one additional post processing step (i.e., gold plating). In this system, we have made use of a coherent detector scheme to measure impedance with superior DDR. Our preliminary measurement results indicate that we can perform label-free detection of DNA hybridization and protein attachment, which indicates the versatility of our chip and its potential use in a variety of assays and applications. Along with the sensor, in this chapter, we have also explained the design and implementation of a 16-bit Σ-Δ ADC specially tailored to digitize the output of our EIS sensor, which serves as an important component for a fully integrated EIS SoC.

Chapter 6

Summary and Future Work

6.1 Summary

The goal of this thesis is to demonstrate the applicability of EIS in biosensing and to build a miniaturized integrated EIS biosensor array, using the standard CMOS process. In chapters 2 and 3, we first introduced the basic concepts in biosensing and EIS. We discussed some of the important considerations in EIS-based biosensing, such as choice of the right electrode surface, the surface linkage option, the effect of monolayer length and the impact of buffer concentration. By making use of an example protein-antibody biosensor system, we demonstrated that EIS is a highly sensitive method for detecting biomolecular interactions happening close to the surface. EIS can act as a low-cost platform for studying the kinetics of molecular interactions.

This work marks one of the first efforts to build a compact modeling technique for distributed electrode-electrolyte systems (Chapter 4). The development of this model is critical for developing integrated biosensors, wherein typically large arrays of coplanar electrodes are used for sensing. Our technique not only enhances the accuracy of modeling, but also permits one to estimate the noise power spectral density of such distributed systems. We

have shown that our models are far more accurate than the analytical models and at the same time, require much lesser computational power and resources when compared to fully distributed simulations.

In this work, the first ever integrated CMOS EIS biosensor array was built (chapter 5), where the sensing electrodes and the detection circuitry are all integrated onto the same die. We made use of the electroless-nickel immersion gold (ENIG) plating method (a maskless gold plating method), in order to deposit gold onto the electrode surface, making it biocompatible. The CMOS EIS IC has a large dynamic range (close to 100dB) and a wide frequency range of operation, both of which are required for the development of open-platform EIS biosensors. Furthermore, the ICs are compact, packing a 10×10 array into a $4mm^2$ area. We have shown that it is possible to perform label-free and real-time studies of biomolecular interactions such as DNA and protein interactions. Furthermore, we have also designed and implemented a 16-bit sigma-delta analog-to-digital converter (ADC), which has been specially tailored to digitize our EIS sensor output. We have shown, that by taking advantage of IC fabrication processes, we can build a compact, high-performance biosensor array, which can push the detection of biomolecular agents, from laboratories, which make use of bulky instruments onto miniaturized platforms that are usable in PoC diagnostic or environmental monitoring applications.

6.2 Future Directions

6.2.1 Flow Setup

In an EIS experiment, any change in the interface impedance can be wrongly interpreted as the signal. Any movement in the bulk solution or the reference electrode, during the introduction of antibody or any other reagent can cause changes in the interface impedance, and it is difficult to separate out the real antigen-antibody binding signal from these motion artifacts. One of the ways to minimize this artifact is to make use of a tightly controlled flow setup, in which the antibody solution or the reagents are introduced at a slow rate, to ensure that the fluid flow does not disturb the equilibrium condition at the interface and significant changes in the interface impedance can only occur due to antigen-antibody binding. Such flow setups are popularly used in many different types of biosensing system such as in the SPR setup in [13] and in the EIS setup in [29].

6.2.2 Spotting

Using IC processes, it is possible to build highly dense arrays, in which multiple analytes can be detected in parallel. As the size of the electrodes and the individual pixels become smaller, it is increasingly difficult to immobilize different probes onto the different electrodes. On our EIS chip, the electrodes are $40\mu m \times 40\mu m$ in size. For these sizes, it is possible to make use of microplotter instruments ([97],[98]), which are capable of depositing different probe solutions with a resolution of 5-10μm. But for even smaller dimensions,

we require better resolution. Also, for really small electrodes (sizes in the order of $1\mu m \times 1\mu m$), the number of probe molecules per electrodes becomes small ($\approx 100 - 1000$). This can cause large percentage variations in probe density from one pixel to the other. It is necessary to analyze how scaling of electrode sizes affects the overall EIS accuracy, taking into account the increase in the probe density variation.

6.2.3 On-chip Sinusoidal Oscillator

For an integrated impedance measurement SoC, we require an on-chip tunable oscillator, which is capable of operating over a wide frequency range. The oscillator needs to have quadrature outputs. Moreover, for portable applications, it will be advantageous for the oscillator to have low power consumption. Furthermore, the oscillator needs to exhibit minimal harmonic distortion, to ensure high accuracy in the impedance measurements.

The simplest method to build an on-chip oscillator is the direct digital synthesis (DDS) method [99], where a large memory (typically 10Mbytes) is used to store samples of a sine wave and by making use of a high resolution DAC, it is possible to generate sine waves with very low distortion. But DDS based oscillators have high power and large area requirements, making it unsuitable for portable applications.

Another method is to make use of current-starved ring oscillators [95]. These oscillators consume much lesser power when compared to DDS based systems and occupy smaller areas. Also it is possible to adjust the frequency

by simply varying the bias current. However, the resultant sinusoid generated has large harmonic distortion components, making them unsuitable for EIS applications.

One of the methods to reduce harmonic distortion is to make use of the Wein-bridge oscillator structure. For ease of implementation, a current mode Wein-bridge can be used, where using a current mirror, one can easily provide sufficient gain for the positive feedback to work. The schematic of a Wein-bridge oscillator is shown in fig 6.1. The resistors required for the Wein-bridge network can be implemented by making use of diode-connected inverters, whose g_m varies as a function of the bias current. This network has a higher Q and by altering g_m of one of the elements, in response to the oscillation amplitude, harmonic distortion can be reduced significantly. The g_m of the inverters (and thereby the oscillation frequency) can be easily tuned by controlling the bias current. Furthermore, the Wein-bridge oscillator directly provides two voltage outputs, which are in quadrature with respect to each other, eliminating the need for frequency dividers or polyphase networks to generate the required phase shifts. As a part of our future work, we are planning to implement a tunable Wein-bridge oscillator circuit, with a feedback loop to reduce harmonic distortion.

6.2.4 Harmonic Rejection Mixing

One of the issues with the lock-in amplification method, is that any harmonic distortion in the excitation signal V_x leads to large errors in the DC

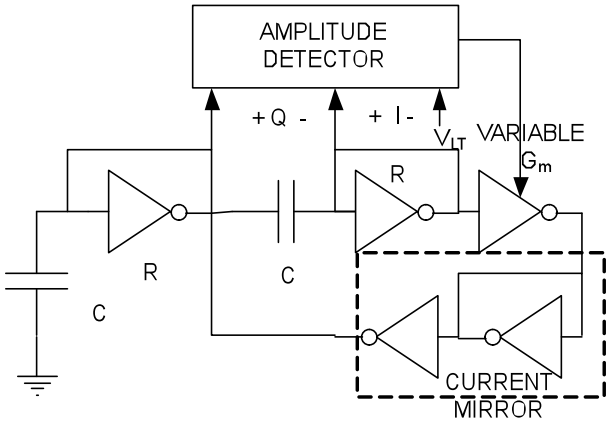

Figure 6.1: Block diagram of the Wein-bridge oscillator.

outputs of the two mixers V_I and V_Q. This places very difficult constraints on on-chip oscillators or on-chip filters, which are used to generate V_x.

In RF receivers, it has been previously shown that it is possible to improve harmonic rejection by adding extra mixers, which multiply the signal with clocks, with phase shifts other than 0° and 90° [100]. This technique is called harmonic rejection mixing. In our design, we can multiply the current flowing through the electrode-electrolyte system, not only with CLK_0 (I) and CLK_90(Q) clocks which are 90° apart, but also with a CLK_45 signal which is at a phase shift of 45° with respect to I. In the ideal case, if the output is calculated using the formula shown in figure 6.2, the effect of the third and fifth harmonics will be cancelled [100]. This can significantly reduce the error in the impedance measurement and permits us to use on-chip oscillators, which can have a higher total harmonic distortion (THD).

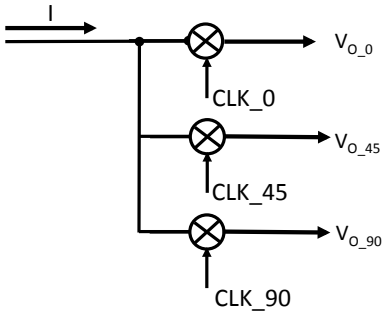

$$V_o = V_{o\_0} + \sqrt{2}V_{o\_45} + V_{o\_90}$$

Figure 6.2: Harmonic rejection method for EIS sensor.

6.2.5 Fully Integrated EIS Sensor

As introduced in Chapter 5, there is a demand for developing fully integrated EIS systems with no external components. The various blocks in a fully integrated EIS sensor is shown in figure 6.3. Apart from the sensor, the integrated EIS system-on-chip (SoC) consists of an analog-to-digital converter, a tunable sinusoidal oscillator, and a DSP processor. The design of ADC has been described in chapter 5. The design of a tunable oscillator has been explained in the previous section. The DSP processor can be used to calculate the magnitude and phase of the impedance from the digitized V_I and V_Q values. With fully integrated EIS sensor, it is possible to develop low-cost, portable EIS platforms.

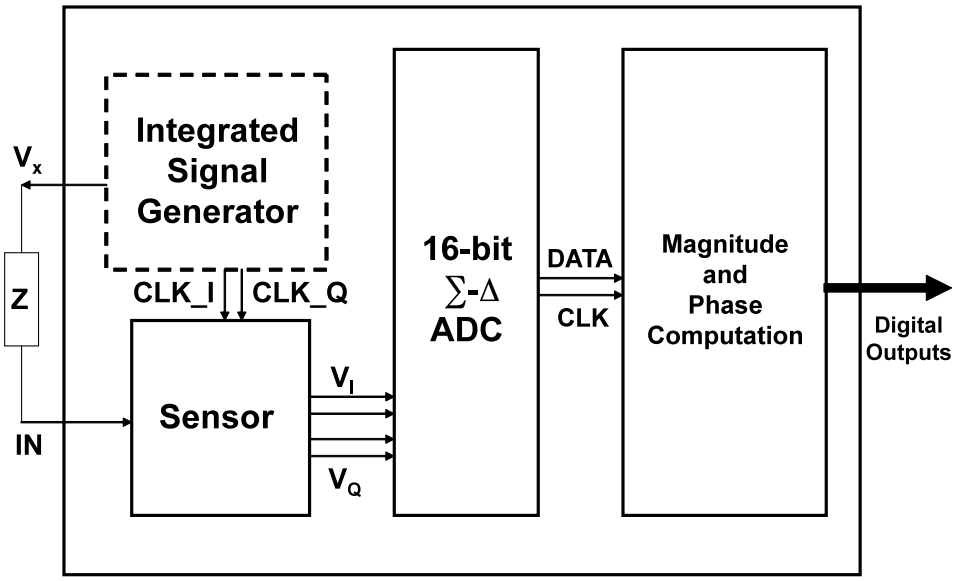

Figure 6.3: A fully integrated EIS SoC

Appendix

Appendix 1

Antigen-Antibody Experimental Protocols

The protocol for the antigen-antigen experiments is summarized in figure 1.1.

Surface Cleaning:

1. The fresh gold slides are washed in acetone for 1 minute.
2. The slides are then placed in ethanol for 1 minute.
3. After drying under nitrogen gas, the slides are placed in an air plasma chamber (700 atm) for 90 seconds.
4. For SC-1 clean, a large glass beaker is filled with 1000ml of water. Inside the beaker, a smaller Teflon beaker containing 100ml of DI water is placed.
5. The large glass beaker is placed on a hot plate and heated to $70°C$.
6. Once the temperature reaches $70°C$, 20 ml of ammonium hydroxide and 20 ml of hydrogen peroxide is added to contents of the Teflon beaker. The temperature is reduced to $65°C$.

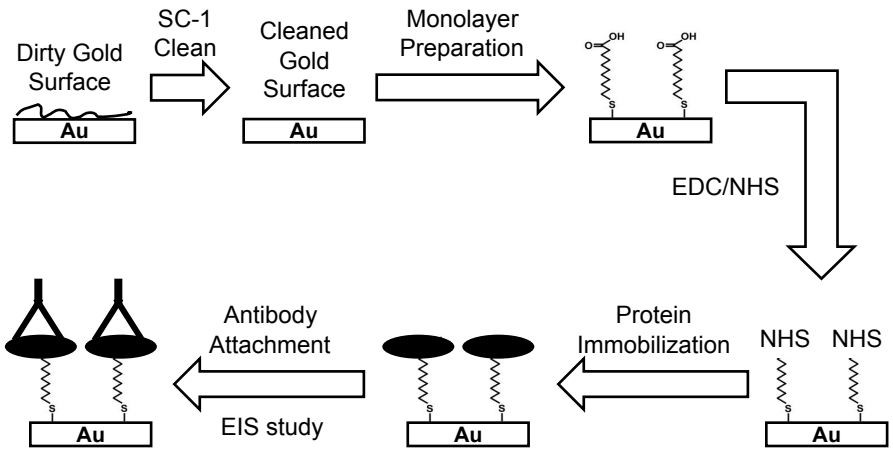

Figure 1.1: Protocol for protein/antibody experiment.

7. The gold slides are placed in the Teflon beaker with the SC-1 mixture. One can observe vigorous bubbling on the gold surface.

   Warning: SC-1 mixture can cause severe irritation and damage to the skin. Hence it is essential to wear proper protection before using the mixture.

8. Leave the slides in the mixture for 15 minutes.

9. After the SC-1 clean, place the slides in a well cleaned beaker containing DI water. Place it on the shaker for 10 min.

10. Transfer the slides to another beaker containing DI water. Place it on shaker for 10 minutes.

11. It is possible that a gold oxide layer might be formed on the gold surface. To reduce the oxide layer, place the slides in ultrapure ethanol and sonicate for one hour.

Monolayer preparation:

12. Prepare fresh solutions of 1mM of alkanethiol in ultrapure ethanol.

13. Place the cleaned slides in a beaker containing the 1mM solution. Back fill with nitrogen gas and tightly seal the beaker to make it airtight.

14. Place the beaker in a dark room for 24 hours.

EDC/NHS protocol:

15. Prepare a fresh solution of 75mM EDC in ethanol and 25mM NHS in 1x PBS.

16. Remove the slides from the monolayer preparation solution. Wash twice in ultrapure ethanol and dry it in nitrogen gas.

17. Place the slides in EDC/NHS solution for 4 hours. Backfill the beaker with nitrogen gas and place an airtight seal over the beaker.

Protein Immobilization :

18. Prepare protein/antibody solutions in 1x PBS buffer.

19. Take the slides from the EDC/NHS solution beaker. Wash it twice in 1x PBS.

20. Wash it once in DI water and dry it under nitrogen gas

21. Pipette 7-10 μl of the protein/antibody solution onto the EDC/NHS treated gold slide. Use cover slips for the liquid to cover the required portions of the slide.

22. Place the slide in a humid chamber for 30 minutes.

23. At the end of 30 minutes, remove the cover slips and wash the slides in 1x PBS twice.

24. Place the protein immobilized slides in 100mM sodium bicarbonate in 1x PBS (pH 8.0) buffer for 30 minutes. This step deactivates any reactive ester groups on the surface.

25. Place the slides in 1x PBS solution. The slides are now ready for EIS experiments.

Antibody Immobilization Experiments:

26. The gold slides with thioctic acid monolayer are first subject to EDC/NHS protocol (steps 15-17) and protein immobilization with a 200nM FoS in 1x PBS solution (steps 18-25).

27. Place the slide in 33nM anti-FoS in 1x PBS solution.

28. Study the attachment of anti-FoS onto a FoS immobilized surface in real-time using EIS.

    The EIS is performed using a bench-top Solartron impedance analyzer. A three-electrode setup is used, in which Ag/AgCl electrode serves as the

reference electrode and a platinum wire serves as the counter electrode. A three electrode setup is commonly used, as the potential of the bulk solution can be set accurately using the reference electrode, irrespective of the magnitude of the current flow through the counter electrode[6].

Make measurements every minute and measure the impedance at 1,5,10,50,100, and 500 Hz.

29. After an hour, place the slides in 1 $\frac{mg}{ml}$ of anti-IgG, which can attach to the immobilized anti-FoS IgG. Repeat real-time EIS measurements.

Bibliography

[1] K. R. Rogers, "Principles of affinity-based biosensors," *Molecular Biotechnology*, vol. 14, no. 2, p. 109, 2005.

[2] D. Leech, "Affinity biosensors," *Chem. Soc. Rev.*, vol. 23, pp. 205–213, 1994.

[3] B. Jang and A. Hassibi, "Biosensor systems in standard CMOS processes," *IEEE Transaction on Industrial Electronics*, vol. 56-4, pp. 979–985, 2009.

[4] A. Hassibi, "On noise processes and limits of performance in biosensors," *Jounral of Applied Physics*, vol. 102, no. 01490, pp. 1–12, 2007.

[5] A. Hassibi, H. Vikalo, J. L. Riechmann and B. Hassibi, "Real-time dna microarray analysis," *Nucleic Acids Research*, vol. 10, no. 1093, pp. 1–12, 2009.

[6] A. J. Bard and L. R. Faulkner, *Electrochemical Methods: Fundamentals and Applications*. Wiley and Sons, New York, 2001.

[7] J. S. Daniels and N. Pourmand, "Label-free impedance biosensors: Opportunities and challenges," *Electroanalysis*, vol. 19, no. 12, p. 12391257, 2007.

[8] O. S. Wolfbei, "Fluorescence methods and applications," *Blackwell*, 2008.

[9] L. J. Kricka and G. H. G. Thorpe, "Chemiluminescent and bioluminescent methods in analytical chemistry," *Science*, vol. 270, no. 5235, p. 467470, 1995.

[10] J.Wang, "Electrochemical nucleic acid biosensors," *Analytica Chimica Acta*, vol. 469, no. 1, pp. 63–71, 2002.

[11] M. Schena *et al.*, "Quantitative monitoring of gene expression patterns with a complementary DNA microarray," *Science*, vol. 270, no. 5235, p. 467 470, 1995.

[12] M. A. Cooper, "Label-free screening of bio-molecular interactions," *Anal. Bioanal. Chem.*, vol. 377, p. 834842, 2003.

[13] J. Homola *et al.*, "Surface plasmon resonance sensors: review," *Sensors and Actuators B: Chemical*, vol. 54, no. 1-2, pp. 3–15, 1999.

[14] B. Jang, P. Cao, A. Chevalier, A. Ellington and A. Hassibi, "A CMOS fluorescence-based Biosensor Microarray," *ISSCC Tech. Dig. Papers*, p. 436 437, 2009.

[15] E. Engvall and P. Perlmann, "Quantitation of specific antibodies by enzyme-labeled anti-immunoglobulin in antigen-coated tubes," *Journal of Immunology*, vol. 109, no. 1, pp. 129–135, 1972.

[16] B. Friguet *et al.*, "Measurements of the true affinity constant in solution of antigen-antibody complexes by enzyme-linked immunosorbent assay," *Journal of Immunological Methods*, vol. 77, no. 2, pp. 305–319, 1985.

[17] M. Ronaghi *et al.*, "DNA Sequencing: A Sequencing Method Based on Real-Time Pyrophosphate," *Science*, pp. 363–365, 1998.

[18] R. Georgiadis, K.P. Peterlinz, and A.W. Peterson, "Quantitative measurements and modeling of kinetics in nucleic acid monolayer lms using SPR spectroscopy," *J. Am. Chem. Soc.*, vol. 122, p. 31663173, 2000.

[19] N. Bassil *et. al*, "One hundred spots parallel monitoring of DNA interactions by SPR imaging of polymerfunctionalized surfaces applied to the detection of cystic brosis," *Sensors Actuat. B: Chem*, vol. 94, p. 313323, 2003.

[20] J. Wang, "Electrochemical glucose biosensors," *Chem. Rev.*, vol. 108, no. 2, pp. 814–825, 2008.

[21] E. Katz and I. Willner, "Probing biomolecular interactions at conductive and semiconductive surfaces by impedance spectroscopy: routes to impedimetric immunosensors, DNA-sensors, and enzyme biosensors," *Electroanalysis*, vol. 15, no. 11, pp. 913–947, 2003.

[22] P.M. Levine, P. Gong, R. Levicky and K. Shepard, "Active CMOS sensor array for electrochemical biomolecular detection," *IEEE J. Solid-State Circuits*, vol. 43, no. 8, pp. 1859–1871, 2008.

[23] M. Schienle *et al.*, "A fully electronic DNA sensor with 128 Positions and in-pixel A/D conversion," *IEEE J. Solid-State Circuits*, vol. 39, no. 2, pp. 2438–2445, 2004.

[24] C. Fan, K.W. Plaxco, and A.J. Heeger, "Electrochemical interrogation of conformational changes as a reagentless method for the sequence-specific detection of DNA," *PNAS*, vol. 100, no. 16, pp. 9134–9137, 2003.

[25] E. Boubour and R. B. Lennox, "Insulating properties of self-assembled monolayers monitored by impedance spectroscopy," *Langmuir*, vol. 16, pp. 4222–4228, 2000.

[26] M. Arnold and M. Meyerhoff, "Ion-selective electrodes," *Anal. Chem.*, vol. 56, no. 5, pp. 20–48, 1984.

[27] P. Bergveld, "Thirty years of ISFETOLOGY: What happened in the past 30 years and what may happen in the next 30 years," *Sensors and Actuators B: Chemical*, vol. 88, no. 1, pp. 1–20.

[28] P. Bergveld, "A 16×16 CMOS proton camera array for direct extracellular imaging of hydrogen-ion activity," *ISSCC Tech Digest*, pp. 590–592, 2008.

[29] C. Berggren, B. Bjarnason and G. Johansson, "Capacitive biosensors," *Electroanalysis*, vol. 13, no. 3, pp. 173–180, 2001.

[30] C. Berggren, P. Stalhandske, J. Brundell and G. Johansson, "A feasibility study of a capacitive biosensor for direct detection of DNA hybridization," *Electroanalysis*, vol. 11, no. 3, pp. 156–160, 1999.

[31] M. Prodromidis, "Impedimetric immunosensors - a review," *Electroachimica Acta*, vol. 55, pp. 4227–4233, 2010.

[32] V. Mirsky, "Impedimetric immunosensors - a review," *Electroachimica Acta*, vol. 55, pp. 4227–4233, 2010.

[33] J. Rickert *et al.*, "A mixed self-assembled monolayer for an impedimetric immunosensor," *Biosensors and Bioelectronics*, vol. 11, no. 8, pp. 757–768, 1996.

[34] R. Schweiss, C. Werner, and W. Knoll, "Impedance spectroscopy studies of interfacial acid-base reactions of self-assembled monolayers," *Journal of Electroanalytical Chemistry*, vol. 540, pp. 145–151, 2003.

[35] J.D. Plummer, M.D. Deal, and P.B. Griffin, "Silicon VLSI Technology," *PrenticeHal*, 2000.

[36] M. Pourbaix, "Electrochemical corrosion of metallic biomaterials," *Biomaterials*, vol. 5, no. 3, pp. 122–134, 1984.

[37] M.J. Schoning *et al.*, "A highly long-term stable silicon-based ph sensor fabricated by pulsed laser deposition technique," *Sensors and Actuators B: Chemical*, vol. 35, no. 1-3, pp. 228–233, 1996.

[38] R.Y. Lai *et al.*, "Comparison of the signaling and stability of electrochemical dna sensors fabricated from 6- or 11-carbon self-assembled monolayers," *Langmuir*, vol. 22, pp. 10796–10800, 2006.

[39] N. Patel *et al.*, "Immobilization of protein molecules onto homogeneous and mixed carboxylate-terminated self-assembled monolayers," *Langmuir*, vol. 13, pp. 6485–6490, 1997.

[40] A. Ulman, "Formation and structure of self-assembled monolayers," *Chem. Rev.*, vol. 96, pp. 1533–1554, 1996.

[41] A.B. Steel, R.L. Levicky, T.M. Herne, and M.J. Tarlov, "Immobilization of nucleic acids at solid surfaces: Effect of oligonucleotide length on layer assembly," *Biophysical Journal*, vol. 79, pp. 975–981, 2000.

[42] H. Maupas *et al.*, "Direct immunosensing using differential electrochemical measurements of impedimetric variations," *Journal of Electroanalytical Chemistry*, vol. 421, pp. 165–171, 1997.

[43] F. Patolsky *et al.*, "Enzyme-linked amplified electrochemical sensing of oligonucleotide DNA interactions by means of the precipitation of an insoluble product and using impedance spectroscopy," *Langmuir*, vol. 15, p. 37033706, 1999.

[44] M.D. Porter, T.B. Bright, D.L. Allara, and C.E.D. Chidseyi, "Spontaneously organized molecular assemblies. 4. structural characterization

of n-alkyl thiol monolayers on gold by optical ellipsometry, infrared spectroscopy, and electrochemistry," *J. Am. Chem. Soc.*, vol. 109, no. 12, pp. 3559–3569, 1987.

[45] S.M. Sagar, F.R. Sharp, and T. Curran, "Expression of c-fos protein in brain: metabolic mapping at the cellular level," *J. Am. Chem. Soc.*, vol. 240, no. 4857, pp. 1328–1331, 1988.

[46] C. Gupta, M.A. Shannon and P.J.A. Kenis, "Electronic properties of a monolayer-electrolyte interface ontained from mechanistic impedance analysis," *Journal of Physical Chemistry C Nanometer Interfaces*, vol. 113, no. 21, pp. 9375–9391, 2009.

[47] L.A. Liotta *et. al*, "Protein microarrays: Meeting analytical challenges for clinical applications," *Cancer Cell*, vol. 3, pp. 317–325, 2003.

[48] S. Kingmore, "Mutliplexed protein measurement: technologies and applications of protein and antibody arrays," *Nature Reviews Drug Discovery*, vol. 5, pp. 310–321, 2006.

[49] S. M. H. Ron and I. Rubinstein, "Self-assembled monolayers on oxidized metals. 2. gold surface oxidative pretreatent, monolayer properties and depression formation," *Langmuir*, vol. 14, no. 5, pp. 1116–1121, 1998.

[50] S. Cogan, "Neural stimulation and recording electrodes," *Annual Review of Biomedical Engineering*, vol. 10, pp. 275–309, 2008.

[51] E.T .McAdams *et al.*, "Factors affecting electrode-gel-skin interface impedance in electrical impedance tomography," *Jounral of Medical and Biological engineering and computing*, vol. 34, no. 6, pp. 397–408, 1996.

[52] T.C. Ferree, P. Luu, G.S. Ruseell and D.M. Tucker, "Scalp electrode impedance, infection risk and EEG data quality," *Clinical Neurophysiology*, vol. 112, no. 3, pp. 536–544, 2001.

[53] R. Gomez *et al.*, "Microfluidic biochip for impedance spectroscopy of biological species," *Biomedical Microdevices*, vol. 3, no. 3, pp. 201–209, 2001.

[54] M. Durr, J. Kentsch, T. Muller, T. Schnelle and M. Stelzle, "Microdevices for manipulation and accumulation of micro- and nanoparticles by dielelectrophoresis," *Electrophoresis*, vol. 24, no. 4, pp. 722–731, 2003.

[55] C. Krantz-Rlcker, M. Stenberg, F. Winquist and I. Lundstrm, "Electronic tongues for environmental monitoring based on sensor arrays and pattern recognition: a review," *Analytica chimica acta*, vol. 426, no. 2, pp. 217–226, 2001.

[56] G. Hanrahan, D.G. Patil and J. Wang, "Electrochemical sensors for environmental monitoring: design, development and applications," *Journal of environmental monitoring*, vol. 6, p. 657 664, 2004.

[57] M. A. Ryan, M. L. Homer, M. G. Buehler, K. S. Manatt, F. Zee and J. Graf, "Monitoring the air quality in a closed chamber using an electronic

nose," *Proceedings of the 27th International Conference on Environmental Systems*, 1997.

[58] D. Tang *et al.*, "A novel immunosensor based on immobilization of hepatitis B surface antibody on platinum electrode modified colloidal gold and polyvinyl butyral as matrices via electrochemical impedance spectroscopy," *Bioelectrochemistry*, vol. 65, no. 1, pp. 15–22, 1997.

[59] R. P. Janek, W. R. Fawcett and A. Ulman, "Impedance spectroscopy of self-assembled monolayers on Au(111): sodium ferrocyanide charge transfer at modified electrodes," *Langmuir*, vol. 14, pp. 3011–3018, 1998.

[60] G. Lillie, P. Payne and P. Vadgama, "Electrochemical impedance spectroscopy as a platform for reagentless bioaffinity sensing," *Sensors and Actuators B: Chemical*, vol. 78, pp. 249–256, 2001.

[61] Y. T. Long, C.Z. Li, H. B. Kraatz and J. S. Lee, "AC impedance spectroscopy of native DNA and M-DNA," *Biophysical Journal*, vol. 84.

[62] A. Manickam, A. Chevaliar, M. McDermott, A. D. Ellington and A. Hassibi, "A CMOS electrochemical impedance spectroscopy biosensor array for label-free biomolecular detection," *Tech. Dig. of International Solid-State Circuits Conference(ISSCC)*, 2010.

[63] W. Franks, I. Schenker, P. Schmutz and A. Hierlemann, "Impedance characterization and modeling of electrodes for biomedical applications," *IEEE Transactions on Biomedical Engineering*, vol. 52, 2005.

[64] P. Jacobs, A. Varlan and W. Sansen, "Design optimization of planar electrolytic conductivity sensors," *Journal of Medical and Biological Engineering and Computing*, vol. 33, no. 6, pp. 802–810, 2005.

[65] S. R. Igreja and C. J. Dias, "Analytical evaluation of the interdigital electrodes capacitance for a multi-layered structure," *Sensors and Actuators A: Physical*, vol. 112, no. 6, pp. 802–810, 2005.

[66] A. Hassibi, R. Navid, R. W. Dutton and T. H. Lee, "Comprehensive study of noise processes in electrode electrolyte interfaces," *Jounral of Applied Physics*, vol. 96, 2004.

[67] C. Gabrielli, F. Huet, and M. Keddam, "Fluctuations in electrochemical systems. i. general theory on diffusion limited electrochemical reactions," *Journal of Chemical Physics*, vol. 99, 1993.

[68] A. V. der Ziel, "Noise in measurements," *Wiley*, 1976.

[69] H. Nyquist, "Thermal agitation of electric charge in conductors," *Physics Reviews*, vol. 32, no. 1, pp. 110–113, 1928.

[70] J.R. Macdonald, J. Schoonman, and A.P. Lehnen, "Applicability and power of complex nonlinear least squares for the analysis of impedance and admittance data," *Journal of Electroanalytical Chemistry and Interfacial Electrochemistry*, vol. 131, pp. 77–95, 1982.

[71] A. Hassibi and T. Lee, "A Programmable $0.18 - \mu m$ CMOS Electrochemical Sensor Microarray for Biomolecular Detection," *IEEE Sensors Journal*, vol. 6, no. 6, pp. 1380–1388, 2006.

[72] A. Manickam, R. Singh, S. Ayazian, and A. Hassibi, "Front-end integrated circuits for high-performance biological and chemical sensing," *Midwest Symposium on Circuits and Systems (MWSCAS)*, pp. 1–4, 2011.

[73] H. Eltoukhy *et al.*, "A $0.18 \mu m CMOS 10^{-6}$ lux bioluminescence detection system-on-chip," *ISSCC Digest of Tech. papers*, pp. 222–224, 2004.

[74] H. Wang *et al.*, "A frequency-shift $CMOS$ magnetic biosensor array with single-bead sensitivity and no external magnet," *ISSCC Digest of Tech. papers*, pp. 438–439, 2009.

[75] N. Sun *et al.*, "CMOS RF Biosensor Utilizing Nuclear Magnetic Resonance," *Journal of Solid-State Circuits*, vol. 44, no. 5, pp. 1629–1643, 2009.

[76] M. Schienle*et al.*, "A fully electronic DNA sensor with 128 Positions and in-pixel A/D conversion," *IEEE J. Solid-State Circuits*, vol. 39, no. 2, pp. 2428–2445, 2004.

[77] F. Heer*et al.*, "CMOS Electro-Chemical DNA-Detection Array with On-Chip ADC," *ISSCC Digest of Tech. papers*, pp. 168–169, 2008.

[78] C. Stagni*et al.*, "Fully Electronic CMOS DNA Detection Array Based on Capacitance Measurement with On-Chip Analog-to-Digital Conversion," *ISSCC Digest of Tech. papers*, pp. 69–70, 2006.

[79] R. Singh *et al.*, "A CMOS $\Sigma-\Delta$ photodetector array for bioluminescence-based DNA sequencing," *Symposium on VLSI circuits*, pp. 96–97, 2011.

[80] P. Roberts-Thomson and K. Shepherd, "Molecular size heterogeneity of immunoglobulins in health and disease," *Clin Exp Immunol.*, vol. 79, pp. 328–334, 1990.

[81] F. Lucarelli *et al.*, "Carbon and gold electrodes as electrochemical transducers for DNA hybridisation sensors," *Biosensors and Bioelectronics*, vol. 19, no. 6, pp. 515–530, 2004.

[82] "Specification for electroless nickel/immersion gold (ENIG) plating for printed circuit board," *IPC Standard 4522*.

[83] A. E. Gamal and H. Eltoukhy, "CMOS image sensors," *Langmuir*, vol. 21, no. 3, 2005.

[84] T. H. Lee, "The design of CMOS radio-frequency integrated circuits," *Cambridge Univ. Press*, 1998.

[85] I.M.Filanovsky and H.Baltes, "CMOS schmitt trigger design," *IEEE Trans. on Circuits and System: Part-I*, vol. 41, no. 1, pp. 46–49, 1994.

[86] J. Macdonald and J. Garber, "Analysis of impedance and admittance data for solids and liquids," *Journal of The Electrochemical Society*, vol. 124, no. 7, 1977.

[87] Y. Jung *et al.*, "Self-directed and self-oriented immobilization of antibody by protein G-DNA conjugate," *Anal. Chem.*, vol. 79, pp. 6534–6541, 2007.

[88] K.S. Ma *et al.*, "DNA hybridization detection by label free versus impedance amplifying label with impedance spectroscopy," *Sensors and Actuators B: Chemical*, vol. 114, no. 1, pp. 58–64, 2006.

[89] B. B. Haab, "Methods and applications of antibody microarrays in cancer research," *Proteomics*, vol. 3, no. 11, p. 2116, 2003.

[90] Y.M. Bae *et al.*, "Detection of insulinantibody binding on a solid surface using imaging ellipsometry," *Biosensors and Bioelectronics*, vol. 20, no. 4, pp. 895–902, 2004.

[91] R. Schreier and G. Temes, "Understanding delta-sigma data converters," *Wiley*, 2005.

[92] B. E. Boser and B. A. Wooley, "The design of sigma-delta analog-to-digital converters," *IEEE J. Solid-State Circuits*, vol. 23, p. 12981308, 1988.

[93] J. Candy and O. Benjamin, "The structure of quantization noise from sigma-delta modulation," *IEEE Transactions on Communications*, vol. 29, no. 9, pp. 1316–1323, 1981.

[94] C. Enz and G. Temes, "Circuit techniques for reducing the effects of op-amp imperfections: Autozeroing, correlated double sampling, and chopper stabilization," *Proceedings of the IEEE*, vol. 84, no. 11, pp. 1584 – 1614, 1996.

[95] B. Razavi, "Design of analog CMOS integrated circuits," *McGraw-Hill*, 2002.

[96] A. Yukawa, "A highly sensitive strobed comparator," *Journal of Solid-State Circuits*, vol. 16, no. 2, pp. 109–113, 1981.

[97] Larson *et al.*, "Device for detecting interaction with an object," *US Patent*, no. US 7849738 B2, 2010.

[98] R. Piner, J. Zhu, F. Xu, S. Hong, and C.A. Mirkin, "Dip-pen Nanolithography," *Science*, vol. 283, no. 12, p. 66, 1999.

[99] L. Cordesses, "Direct digital synthesis: a tool for periodic wave generation," *IEEE Signal Processing Magazine*, vol. 21, no. 4, pp. 50–54, 2004.

[100] J.A. Weldon *et al.*, "A 1.75-GHz highly integrated narrow-band CMOS transmitter with harmonic-rejection mixers," *Journal of Solid-State Circuits*, vol. 36, no. 12, pp. 2003–2015, 2001.

Vita

Arun Manickam is a Ph.D. student in the Electrical and Computer Engineering Department of the University of Texas at Austin. His research interests are IC design for biomedical applications and interface modeling. His current research is on the design of an impedance spectroscopy SoC. He completed his undergraduate in Electronics and Communication Engineering in 2006 from Anna University, India.

Email id: mmarun@utexas.edu

This dissertation was typeset with LaTeX[†] by the author.

[†]LaTeX is a document preparation system developed by Leslie Lamport as a special version of Donald Knuth's TeX Program.